UNIVERSITY of CALIFORNIA
Santa Barbara

Physical aspects of cell and tissue elongation

A dissertation submitted in partial satisfaction of the
requirements for the degree of

Doctor of Philosophy

in

Physics

by

Samhita P. Banavar

Committee in charge:

Professor Otger Campàs, Co-Chair

Professor Phillip A. Pincus, Co-Chair

Dr. Tau-Mu Yi, Associate Researcher

Professor Jean M. Carlson

December 2019

The dissertation of Samhita P. Banavar is approved.

Dr. Tau-Mu Yi, Associate Researcher

Professor Jean M. Carlson

Professor Phillip A. Pincus, Co-Chair

Professor Otger Campàs, Co-Chair

December 2019

To Amma and Appa

Acknowledgements

I am indebted to my advisor, Otger Campàs. I have been inspired by your enthusiasm and your talent for tackling exciting and relevant problems. Thank you for your unparalleled support and guidance. I am extremely fortunate to have learned so much from you and am very grateful to have you as my mentor.

I would like to thank my co-advisor, Fyl Pincus, and my thesis committee members, Jean Carlson and Tau-Mu Yi. Thank you very much, Jean, for your encouragement, mentorship, and guidance throughout my PhD career.

This work was supported by The National Institute of General Medical Sciences of the National Institutes of Health (R01GM113241), The National Science Foundation Graduate Research Fellowship under Grant (DGE 1144085) and The Mellichamp Fellowship for Graduate Students in Systems Biology and Bioengineering at UCSB.

I would like to thank my collaborators on the yeast project. Thank you, Tau-Mu Yi for being my guide to the yeast world and to experiments. I would also like to express my deep gratitude to Linda Petzold, who has not only been a wonderful collaborator but also has supported me throughout my PhD career. This work would not have been possible without Michael Trogdon. Thank you for teaching me Python, for the insightful discussions, and for your encouragement. Also, Carlos Gomez was invaluable to this work. He performed the yeast experiments, spending hours at the microscope and counting thousands of yeast cells. Thank you for interesting discussions about science and beyond.

I would like to thank my collaborators on the zebrafish project. Thank you, Payam Rowghanian and Emmet Carn for teaching me about COMSOL and providing the springboard for this project. I am grateful to Georgina Stooke-Vaughan for gathering amazing photos of the zebrafish tailbud and teaching me about its development. Thank you, Sangwoo Kim, for your valuable insights on analyzing the data.

I have enjoyed working with and learning from all the Campàs Lab members, Ale, Friedhelm, Jamie, Adam, Mishel, Elijah, James, David, Hannah, Dennis, Yucen, Renwei, Marie, and Antoine. Thank you to Dennis for being the COMSOL wizard. And special thanks to Marie and Antoine – without their morning banter and advice, this final year would have been much less enjoyable.

I would like to thank the staff of the physics department, the Center for Nanosystems Institute, the Bio-engineering department, the Institute for Collaborative Biotechnologies, and the mechanical engineering department. I would like to specially mention Jennifer Farrar for friendly office chats when handing in forms or sorting out physics matters, Bob Hanson for being an amazing building manager of CNSI, Ruby Holder and Elizabeth Jensen for being the experts on reimbursements and helping with occasional purchases, and Francisco for your very early morning greetings in the hallways of CNSI.

I am very grateful to my Santa Barbara friends, Anusha, Stephanie, Annie, and Diana, who made life outside the office fun and Chen and Rishi, whose phone calls provided great support and entertainment.

Last but not least, I thank my dear family who have stood by me and encouraged me all these years.

Curriculum Vitæ

Samhita P. Banavar

Education

2019	Ph.D., Physics, University of California, Santa Barbara
2013	B.S, Physics, The Pennsylvania State University, University Park, PA
2013	B.S, Mathematics, The Pennsylvania State University, University Park, PA
2009	State College Area High School, State College, PA

Publications

"Mechanical feedback coordinates cell wall expansion and assembly in yeast mating morphogenesis", **Samhita P. Banavar**, Carlos Gomez, Michael Trogdon,Linda R. Petzold, Tau-Mu Yi, Otger Campàs. *PLoS Comput Biol* 14, (2018)

"The effect of cell geometry on polarization in budding yeast", Michael Trogdon, Brian Drawert, Carlos Gomez, **Samhita P. Banavar**, Tau-Mu Yi, Otger Campàs, Linda R. Petzold. *PLoS Comput Biol* 14, (2018)

"Mechanical feedback maintains polarization during mating projection growth in budding yeast", **Samhita P. Banavar**, Michael Trogdon, Brian Drawert, Tau-Mu Yi, Linda R. Petzold, Otger Campàs. *In submission*

"Theoretical studies of Zebrafish body axis elongation", **Samhita P. Banavar**, Emmet Carn, Payam Rowghanian, Georgian Stooke-Vaughan, Sangwoo Kim, Otger Campàs. *In submission*

Honors and Awards

2017	Mellichamp Fellowship in Systems Biology and Bioengineering, UCSB
2014	Department of Physics Outstanding TA Award, UCSB
2013	Herbert P. Broida Fellowship, UCSB

2013	National Science Foundation Graduate Research Fellowship, NSF
2013	Phi Beta Kappa
2013	Department of Physics David Bohm Award, PSU
2009	Schreyer Honors Scholar, PSU
2009	Robert C. Byrd Honors Scholarship

Abstract

Physical aspects of cell and tissue elongation

by

Samhita P. Banavar

The morphogenesis of cells and tissues involves an intricate coordination of physical and biological processes. In this thesis, we focus on the unidirectional elongation of cells and tissues. We use budding yeast mating projection growth and the axis elongation of zebrafish as our motivating examples of cell elongation and tissue elongation respectively. Both require a fluid to solid transition in the growing structure for elongation to occur.

The mating projection growth of yeast cells display polarized, unidirectional growth. It is unclear how information about the mechanical state of the wall is relayed to the molecular processes building it, thereby enabling the coordination of cell wall expansion and assembly during morphogenesis. Combining theoretical and experimental approaches, we show that a mechanical feedback coordinating cell wall assembly and expansion is essential to sustain mating projection growth in budding yeast (Saccharomyces cerevisiae). Our theoretical results indicate that the mechanical feedback provided by the Cell Wall Integrity pathway, with cell wall stress sensors Wsc1 and Mid2 increasingly activating membrane-localized cell wall synthases Fks1/2 upon faster cell wall expansion, stabilizes mating projection growth without affecting cell shape. Experimental

perturbation of the osmotic pressure and cell wall mechanics, as well as compromising the mechanical feedback through genetic deletion of the stress sensors, leads to cellular phenotypes that support the theoretical predictions.

The mechanisms that maintain continued polarization to the growth region during mating projection formation, and the subsequent change in geometry from a spherical cell, remain unknown. We theoretically show that a genetically-encoded mechanical feedback relaying information about the cells geometry is sufficient to ensure that key polarity molecules (e.g., Cdc42) remain localized to the site of growth. Interestingly, we find that a common feedback mechanism, connecting the physics/geometry of the cell wall to the cellular molecular machinery, can both stabilize cell growth and maintain polarity.

Tissue morphogenesis requires the successful translation of molecular information to the physical fields that shape tissues into their functional morphologies. While regional control of cellular forces or cell proliferation has been assumed to be the main contributor to shaping tissues, it has been recently shown that the elongation of the body axis entails a fluid-to-solid transition in the state of the tissue. Here we theoretically study how the regional control of the fluid and solid states controls morphogenesis of the extending body axis and how morphogenetic flows emerge from the underlying inhomogeneities in physical fields. We theoretically describe from first principles the process of tissue morphogenesis accounting for contact inhibition of proliferation, a mechanical feedback preventing cell proliferation when tissue pressure is high, and show that both the existence of a fluid-to-solid transition and the tissue surface tension determine the shape of the

tissue and its ability to elongate unidirectionally. Our results indicate the existence of counter-rotating vortices in the tissue that arise from the interplay between tissue rigidification and growth. Posterior tissues are found to globally push on anterior tissues to support elongation, but stresses in the tissue can display regions of both pulling and pushing forces. These results help explain how the regional fluidization of the posterior tissues drives posterior body elongation in vertebrates and the formation of complex morphogenetic flows.

Contents

Chapter 1

Introduction

Morphogenesis derives from the Greek words meaning the emergence ($\gamma\epsilon\nu\nu\tau\sigma\eta$- gennisi) of shape ($\mu o\rho\phi\eta$- morphi). Cells and tissues come in a variety of different shapes and sizes with their shape being a key determinant of function. What determines the shapes of cells and tissues? An unanswered question is how a cell acquires its physical form from the blueprint of life, its DNA. However dependent a cell's shape may be on the genetic instructions, as D'Arcy Thompson aptly pointed out a century ago, living cells must grow in accord with the laws of physics [1]. Here will use the machinery of mathematics and physics to understand the morphology of cells and tissues.

The emergence of patterns in inert out-of-equilibrium systems has long been studied in physics. In these systems, the patterns emerge through an instability of the homogeneous state caused by noise, generally yielding defects in the patterns. The emergence of shape, but not necessarily patterns, in living (out-of-equilibrium) systems, such as in cells or

tissues, is far less understood. In this case, any errors (or defects) could be fatal for the organism, suggesting that qualitatively different physical principles may be at play in shaping living structures compared to inert systems. It is unclear to what extent physical laws constrain the space of possible shapes and how the genetic/molecular information controls the physical processes that shape biological structures. In this thesis, we explore distinct cases of morphogenesis in search for answers to these questions.

1.1 Morphogenesis of cells and tissues

What do a human, a zebrafish, a yeast cell, and a bacterium have in common? DNA, the molecular instructions for life! The genetic information encoded in DNA is extremely important as it leads to the protein synthesis and biochemical signaling which organizes the cells and tissues. Many studies have focused on the genetic and molecular aspects of morphogenesis. Genetic screens are carried out to understand a genes influence on shape. Biomolecular patterns are thought to influence cells in an embryo leading to morphogenesis [2]. A famous modeling study of the biochemical phenomenon leading to morphogenesis is Alan Turings The Chemical Basis of Morphogenesis. Turing showed that non-trivial spatial patterns can arise from having two chemical agents, morphogens, which diffuse and interact. Even though genes and the subsequent biochemical signaling are extremely important for organizing the events underlying morphogenesis, the physical processes sculpting cells and tissues are equally vital.

1.2 Physical aspects of morphogenesis

Our aim is to study the physical aspects of growth. Morphogenesis in biological systems share some features with the molding of clay into a beautiful sculpture in a reproducible and robust manner. The artists hands sculpt the clay into the desired form by applying forces, water is added judiciously to soften the clay, and the soft material is added at the appropriate place and time to build the form. Similarly cells and tissues are shaped by physical forces, the material properties need to be tuned just right to allow for the correct growth dynamics, and the material needed for growth has to be supplied to the right location at the right time. Morphogenesis necessarily involves the exquisite spatiotemporal orchestration of these three processes, which, in turn, are directly linked to biochemical processes within the cell.

1.2.1 Cellular morphogenesis

The shapes of eukaryotic (animal, plants, fungi) cells are largely determined by a structure of meshed polymers that bears the load. These structures are highly dynamic to allow for growth to occur. In animal cells, the shape is determined by the cytoskeleton (Fig. 1.1A). The cytoskeleton is made up of microfilaments, intermediate filaments, and microtubules. The cytoskeleton supports the cell membrane, provides a scaffold for organizing the interior of the cell and provides tracks for intracellular transport. In plant and fungi cells, the shape is determined by the cell wall (Fig. 1.1B). The cell wall is a rigid layer providing structural support for the cell and is primarily made up of carbohydrates.

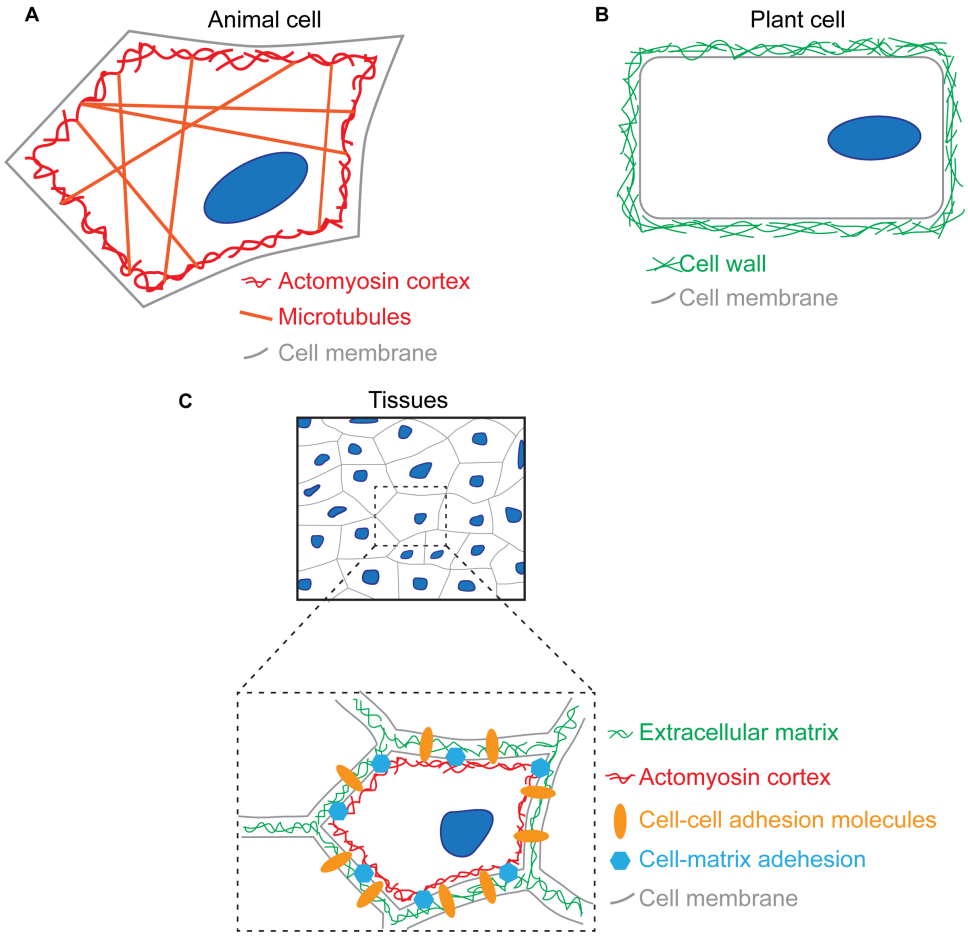

Figure 1.1: **Sketch of structure providing features of.** A. Animal cells, B. Plant and fungal cells, and C. Tissues adapted from [3].

Walled cells are under a high osmotic pressure. In our efforts to understand cellular morphogenesis, we focus on tip growing walled cells because the shape is much easier to define than in animal cells. The osmotic pressure is the driving force of growth and one requires tuning of the local material properties of the cell wall and coordination of new cell wall material addition.

1.2.2 Tissue morphogenesis

Tissues are more complex and are a group of cells that share a common embryonic origin. Although the control of the physical properties leading to morphogenesis occurs at the cellular and subcellular levels, an emergent behavior at the supracellular scale leads to morphogenetic events. The tissues shape is determined by various supracellular factors such as cell-cell adhesion, the properties of the extracellular matrix (ECM), cell rearrangements and cell divisions. Active cellular forces like actomyosin contractility and changes in cell volume can drive tissue morphogenesis. The material properties of the tissue can be controlled by cortical actomyosin contractility, by cell-cell or cell-matrix adhesion, or by the ECM (Fig. 1.1C). Material can be added or removed by cell proliferation, programmed cell death, cell volume changes, or ECM deposition. These are the crucial processes that sculpt the tissue. In addition, mechanical forces can promote the addition of new ECM and there can also be a rich interplay between the mechanical forces and tissue material properties [3]. Understanding tissue morphogenesis is an intricate problem combining many primary aspects of physical growth.

1.3 Unidirectional growth

We focus on understanding directed growth. Elongated objects have a high surface to volume ratio which can be advantageous to absorb nutrients and transmit signals. The mathematical description can often be simplified due to a symmetry about the direction of elongation. Cells and tissues exhibit unidirectional growth which we use as a motivating

example to better understand morphogenesis.

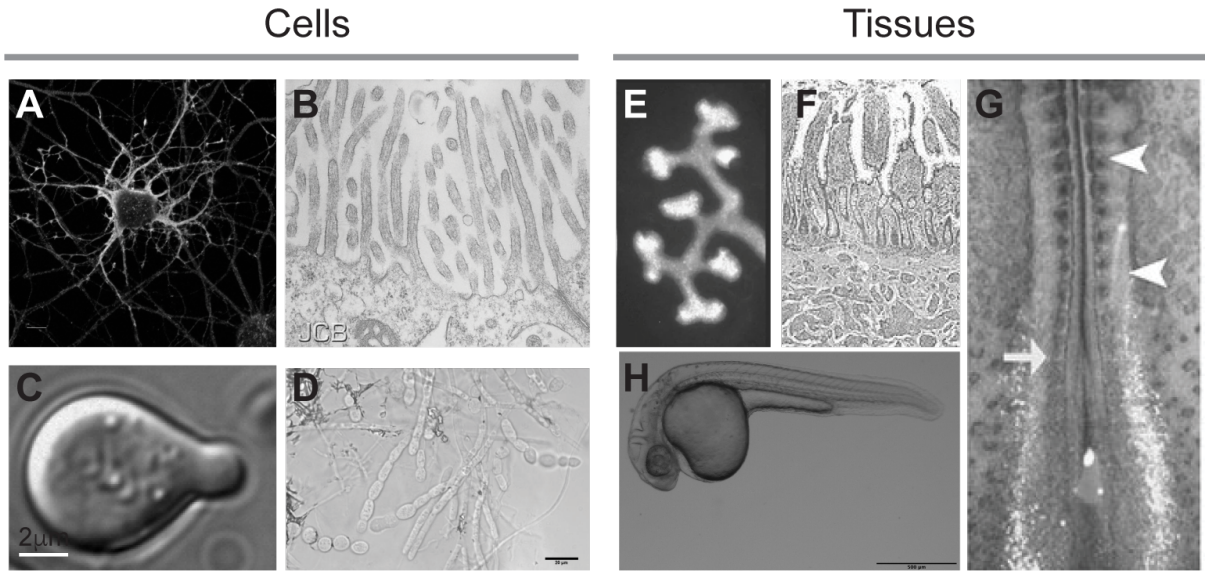

Figure 1.2: **Elongating cells and tissues.** A. Neuron [4] B. Microvilli [5] C. Budding yeast with mating projection courtesy of Carlos Gomez of the Campàs lab D. Fungal hypha [6] E. Kidney branches [7] F. Intestinal villi [8] G. Primitive streak of mouse embryo [9] H. Zebrafish body axis elongation courtesy of Logan Roberts of the Campàs lab.

1.3.1 Cellular morphogenesis

A cells shape is a key determinant of its function. Nerve cells have long thin branches, called dendrites, extending from the neuronal cell body in order to transmit signals over large distances (Fig. 1.2A) [10]. Cells lining the small intestine have long thin protrusions called microvilli (Fig. 1.2B) which are important for absorbing nutrients. Tip growth is a common mode of cellular expansion seen across walled celled species in fungal hyphae (Fig. 1.2D), pollen tubes, and the mating projection of yeast cells (Fig. 1.2C) [11]. It occurs due to a local expansion at the tip/apex thus greatly simplifying the mathematical

and physical analysis of cell growth and it relies on the biochemical process of polarization which localizes the necessary molecules to the site of growth. We seek to understand polarization and tip growth using the yeast mating projection as our motivating example.

Previous studies of the mechanics of tip-growing walled cells of plant and fungal species [12, 13, 14] have underscored the importance of two distinct features: the polarized assembly of new cell wall material at the tip and inhomogeneous mechanical properties enabling its apical expansion. Earlier theoretical analyses of tip-growth focused on cell wall assembly [15, 16, 17] or cell wall mechanics [14, 18, 19] separately. Since then both cell wall assembly and mechanics [20, 21, 22, 23] have been treated simultaneously but as independent processes. We find that that this assumption leads to an instability in cell wall expansion and causes cell lysis, at odds with experimental observations. Our work is directly relevant to cell viability during cell wall remodeling and morphogenesis and is the first to consider the coordination (coupling or feedback) between cell wall mechanics and assembly in the morphogenesis of walled cells.

The triggering and maintenance (at the correct spatial location) of the molecular polarization of a cell is of fundamental importance for tip growth. While many existing models of cell polarization are able to reproduce the spontaneous symmetry breaking and establishment of a polarization cap in a static, 1D or 2D spherical cell geometry [24, 25], they do not explain the maintenance of cell polarization at the tip of mating projections [26], required for polarized growth. Unlike earlier theories, which either considered the dynamics of polarization in fixed geometries or the mechanics of cell morphogenesis

without accounting for polarization, we couple the dynamics of cell polarization and cell wall mechanics during mating projection growth. Remarkably, the mechanical feedback encoded in the CWI pathway coordinates both the dynamics of the polarization cap and cell morphogenesis, maintaining the polarization cap at the tip of the mating projection and sustaining mating projection growth.

1.3.2 Tissue morphogenesis

Similar to cells, tissues also develop into elongated structures. We see this in the branching of the lungs wherein the slender branches help increase the surface area to allow for gas exchange with the uptake of oxygen and the release of carbon dioxide. Branching is also seen in the kidney as seen in Fig. 1.2E. The tissue in the small intestine grow into protrusions which are called the intestinal villi (Fig. 1.2F), which help with absorption in the gut. The digits on our hands are also formed by tissue elongation. Tissue elongation can also define the body axes of an organism (Fig. 1.2G) [27]. Here we use zebrafish tailbud elongation as a motivating example to understand elongation at the tissue scale as seen in Fig. 1.2H.

Recent quantitative measurements of the spatial variations in both mechanical stresses and tissue material properties showed that a fluid-to-solid transition in the state of the tissue played a role in guiding the posterior extension of the body axis in zebrafish embryos [28]. Cell-based models are well suited to understanding tissue morphogenesis when cellular resolution is necessary, but typically lead to a large number of parameters because

the mechanical state for each cell needs to be accounted for [29, 30, 31, 32, 33, 34]. Tissue morphogenesis can also be described by coarse-grained continuum approaches that only require information of physical fields at supra-cellular scales [35]. Previous continuum descriptions [35, 36, 37] of tissue morphogenesis generally assumed spatially uniform mechanical properties (i.e., constant tissue viscosity or constant stiffness depending on the tissue) and considered only spatial variations in either cell proliferation or forces because experimental studies have primarily considered spatial variations of these quantities. In the specific case of body axis elongation, self-propelled particle descriptions [38, 39, 40, 41] assumed set tissue shape (fixed tissue boundaries), allowing the prediction of cell movement but not tissue morphogenesis since the boundaries are, by construction, fixed. Importantly, most cases of tissue morphogenesis are examples of so-called free boundary problems, in which tissue flows change the shape of the tissue and these boundary changes affect the movements inside the tissue. Therefore, in tissues that change shape during morphogenesis, it is important to consider the coupled dynamics of the tissue shape and morphogenetic flows. Our studies explicitly incorporates the role of spatial variations in tissue mechanical properties and, especially, the role of localized transitions between the fluid and solid tissue states.

1.4 Outline

We carry out theoretical studies of the dynamics of growth of cells and tissues using a coarse grained approach and basic physics first principles. Interestingly, we find that for

both cell and tissue elongation, a fluid to solid transition of the growing material plays a pivotal role. Our theoretical descriptions are based on experimental evidences and one of our principal goals is to understand the interplay between the biochemical and physical processes leading to morphogenesis.

In chapter 2, we discuss how the shaping of tip growing walled cells requires a tight coordination of cell mechanics and growth. The cell wall undergoes a fluid to solid transition in order for elongation to occur. Using the mating projection growth of budding yeast (Saccharomyces cerevisiae) cells as a model system, we show that a genetically-encoded mechanical feedback relays information about the mechanical state of the cell wall to the intracellular processes assembling it, thereby coordinating cell wall expansion and growth during cell morphogenesis. The mechanism of mechanical feedback predicted in our work was later observed in fission yeast and there have been hints of a similar feedback mechanism in a very different system of pollen tube growth in plants. This underscores the likelihood of a system-independent universal mechanism that coordinates the physical and molecular aspects of cell morphogenesis.

In chapter 3, we discuss the process by which budding yeast cells establish and maintain cell polarization, which is key to unidirectional cellular morphogenesis and mating projection growth. We theoretically show that the same genetically-encoded mechanical feedback is also sufficient to ensure that key polarity molecules (e.g., Cdc42) remain localized to the site of growth. It is noteworthy that this same mechanical feedback mechanism is responsible for cell viability during growth, indicating that a common feedback

mechanism, connecting the physics/geometry of the cell wall to the cellular molecular machinery, can both stabilize cell growth and maintain polarity.

In chapter 4, we study theoretically how the regional control of the fluid and solid states controls morphogenesis of the extending body axis in the zebrafish tailbud and how morphogenetic flows emerge from the underlying inhomogeneities in physical fields. We theoretically describe, from first principles, the process of tissue morphogenesis accounting for contact inhibition of proliferation and a mechanical feedback preventing cell proliferation when the tissue pressure is high. We show that both the existence of a fluid-to-solid transition and the tissue surface tension determine the shape of the tissue and its ability to elongate unidirectionally.

We conclude in Chapter 5 by summarizing our results and discussing future directions.

Chapter 2

Budding yeast mating projection growth

From cell division to polarization and growth, cells constantly change their shapes to perform specific tasks [42, 43, 44]. These morphological changes are achieved through remodeling of the structures that mechanically sustain the cell, such as the cytoskeleton in animal cells and the cell wall in walled cells. Unlike animal cells, which can undergo fast and complex cell shape changes, walled cells must take extra care during shape changes, as the cell wall needs to mechanically sustain their high internal turgor pressure throughout the cell wall remodeling process [45, 46, 47]. A lack of coordination between cell wall expansion and assembly during cell growth can be fatal for the cell, as the thinning of the cell wall in expanding regions may lead to cell lysis unless it is carefully balanced by newly assembled wall material. While it is believed that the coordination of

cell wall expansion and assembly is necessary to cell wall remodeling and morphogenesis, the mechanisms behind this coordination remain largely unknown. This work was done in close collaboration with Carlos Gomez, Michael Trogdon, Dr. Tau-Mu Yi and Professor Linda Petzold. This chapter was published in PLOS Computational Biology [48].

2.1 Introduction

Cell shape changes are ultimately governed by the mechanical state of the cell wall [46, 49, 47]. Studies of the mechanics of walled cell morphogenesis have predominantly focused on tip-growing cells of plant and fungal species because of their large size, simpler geometry and fast growth rates [12, 13, 14]. In this highly polarized growth mode, cells adopt a tubular shape that extends only at the apical region (Fig. 2.1). During this process, cells polarize their cytoskeleton and localize exocytosis to the growing region, exactly where the cell wall needs to be assembled and remodeled. While the molecular underpinnings of tip-growth differ across species, two basic features have been shown to be necessary [49]: polarized assembly of new cell wall material at the tip, and inhomogeneous mechanical properties enabling its apical expansion (Fig. 2.1F). Previous theoretical descriptions of tip-growth focused on cell wall assembly [15, 16, 17] or cell wall mechanics [14, 18, 19] separately. More recent descriptions accounted for both cell wall assembly and mechanics [20, 21, 22, 23], but assumed these processes to be independent of each other. As we show below by directly solving the dynamics of cell wall assembly and expansion, assuming cell wall mechanics and assembly to be independent

of each other always leads to unstable cell wall expansion and cell lysis, in stark contrast with experimental observations. Despite its relevance to cell viability during cell wall remodeling and morphogenesis, no previous theoretical descriptions have addressed the role of coordination (coupling or feedback) between cell wall mechanics and assembly in the morphogenesis of walled cells.

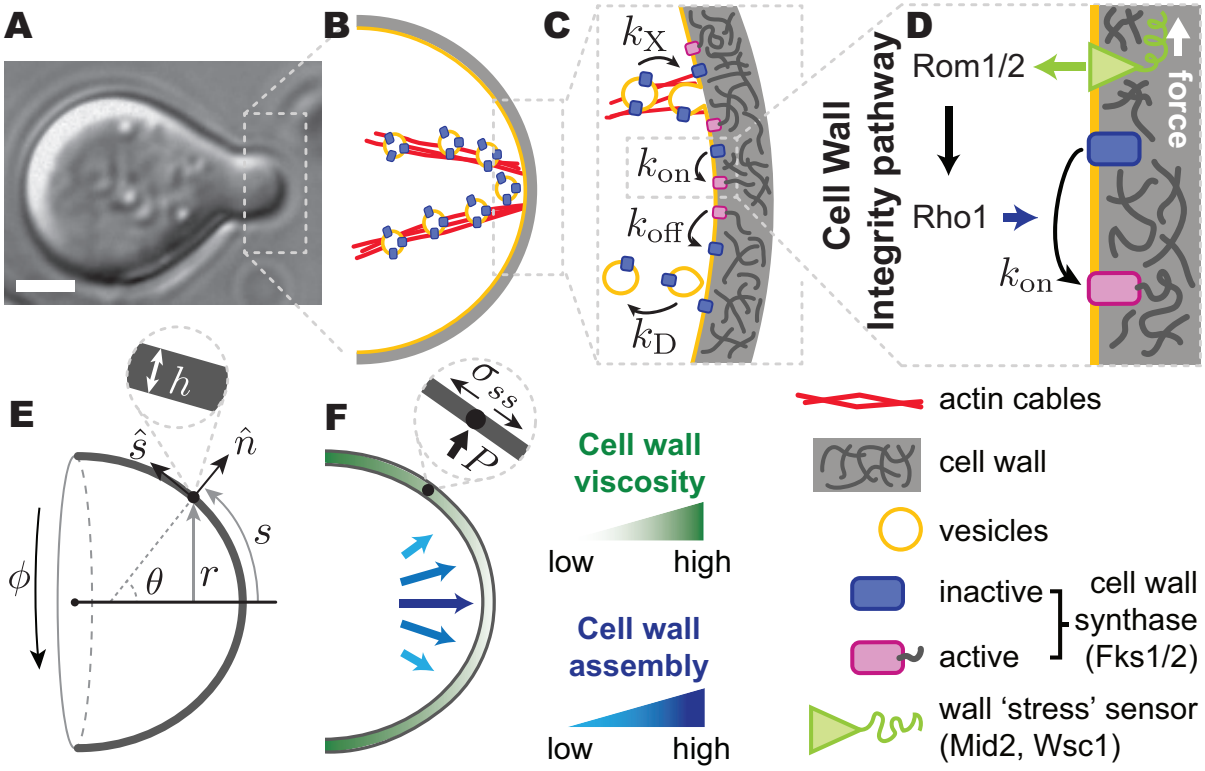

Figure 2.1: **Schematic diagrams of relevant events and quantities in mating projection growth.** (A) Transmitted light image of a *S. cerevisiae* cell growing a mating projection in the presence of α-factor. Scale bar, 2μm. (B-D) Sketch of molecular events leading to the delivery and activation of cell wall synthases Fks1/2 at the apex. See table 2.2.2 for definitions of parameters. (E) Geometry of the system and definition of the relevant variables. (F) Sketch depicting the increasing cell wall viscosity and decreasing cell wall assembly away from the apex. The inset depicts local normal force balance at the cell wall. All variables are defined in the main text.

In addition to well-known model systems for tip-growth, such as pollen tubes in plants

and hyphal growth in higher fungi [12, 13, 49], budding yeast displays tip-growth during mating. Haploid cells secrete pheromone (α- and **a**-factors for mating types **a** and α, respectively) that elicits the growth a tubular mating projection from the partner of the opposite type [50, 51] (Fig. 2.1A). Since the molecular basis of cell polarization and cell wall assembly and remodeling have been extensively studied in budding yeast, tip-growth of mating projections provide a unique system to study the mechanism of coordination between cell wall mechanics and assembly.

In **a**-cells, binding of α-factor to its cognate receptor activates the heterotrimeric G-protein, leading to the activation and polarization of the small G-protein Cdc42, a master regulator of cell polarization [52]. Cdc42-mediated polarization recruits various molecular factors to an apical region of the plasma membrane known as the polarisome, where the formin Bni1 drives the nucleation of actin cables, focusing exocytosis at the apex [50, 44] (Fig. 2.1B). Secretory vesicles transporting Fks1/2 cell wall synthases and cell wall remodeling enzymes (e.g., glucanases) move along actin cables to the exocyst, eventually leading to the incorporation of Fks1/2 synthases to the plasma membrane and the release of glucanases into the preexisting cell wall (Fig. 2.1B,C) [53, 54, 55, 56]. Together, these events molecularly and mechanically polarize the cell, causing a localized expansion of the cell wall at the apex (Fig. 2.1B,F).

In general, the expansion of the cell wall is a dangerous situation that the cell needs to carefully control. Since the cell wall sustains the high cell's internal turgor pressure, uncontrolled cell wall expansion can lead to cell wall piercing and cell lysis. In bud-

ding yeast, the Cell Wall Integrity (CWI) pathway is known to help the cell prevent loss of cell wall mechanical integrity in a variety of situations [57, 58, 59, 60], from mating pheromone-induced growth to vegetative growth [59, 58, 61]. Five transmembrane proteins, namely Wsc1, Wsc2, Wsc3, Mid2, and Mtl1, are thought to act as stress sensors and relay information about the mechanical state of the cell wall to multiple intracellular processes via the activation of Rho1 GTPases [59, 62, 63, 58, 64, 65, 66, 67]. Previous works have shown that Wsc1 and, especially, Mid2 play an important role during mating pheromone induced growth, while the remaining stress sensors do not seem to strongly affect projection growth [68, 69, 70, 67, 71]. While the specific mechanical quantity that these stress sensors monitor in the cell wall remains unclear, activation of the CWI pathway leads to the downstream Rho1-mediated activation of several key molecular components, including cell wall synthases (Fks1/2), actin nucleators (Bni1) and mediators of exocytosis (Sec3), and also induces a transcriptional response via a MAPK cascade [59]. The activation of cell wall Fks1/2 synthases [59, 63, 51] provides the most direct coupling between cell wall mechanics and assembly and could potentially stabilize mating projection growth (Fig. 2.1D). However, it is unknown if such a simple, direct mechanical feedback can stabilize morphogenesis of walled cells by itself.

Using mating projection growth in budding yeast as a model system, and combining experiments and theory, we show that coordination between cell wall mechanics and assembly through direct Fks1/2 activation in the CWI pathway (mechanical feedback) stabilizes mating projection growth without affecting its geometry. In what follows, the

term 'mechanical feedback' refers to the nature of the input signal that is sensed and relayed by stress sensors in the CWI pathway. We first derive a theoretical description that connects the cell wall mechanics to the intracellular processes building the wall (Fks1/2 activation dynamics) via the CWI pathway, and show that stable projection growth can only persist in the presence of mechanical feedback. In the absence of coordination between cell wall assembly and mechanics, cell wall expansion is always unstable, leading to either progressive thickening or thinning of the cell wall depending on conditions. Our experimental results indicate the compromising the mechanical feedback through genetic deletions of the wall stress sensors Mid2 and Wsc1, and also through perturbations of cell wall mechanics and increased turgor pressure, all lead to defects in mating projection growth and cell viability. Our experimental observations are in agreement with the theoretical predictions, suggesting that the mechanical feedback provided by the CWI pathway via direct activation of Fks1/2 synthases can stabilize projection growth without altering cell geometry. In addition, by directly measuring the size of the exocytosis region in wild-type (WT) and mutants with compromised mechanical feedback, we show that the size of the mating projection is controlled by the size of the exocytosis region, but is independent of the strength of the mechanical feedback, as predicted theoretically. Altogether, our results show that a mechanical feedback between cell wall mechanics and assembly is essential for stability of cell wall expansion and projection growth, but that its geometry and size are insensitive to the mechanical feedback.

2.2 Theoretical description

The expansion of the cell wall during morphogenesis is powered by the cell's internal turgor pressure, P. Such high pressure is mechanically sustained by the cell wall, which provides mechanical integrity to the cell at all stages, including during mating projection growth. Similarly to other organisms [13, 46, 49], the cell wall in budding yeast can be considered a thin shell surrounding the cell, as the wall thickness ($\sim$ 100 nm [72]) is much smaller than the radius of the projection ($\sim 1\,\mu$m [73]). Since the cell's shape is determined by the location of its cell wall, we describe the growth of the mating projection as the expansion of an asymmetric thin shell, parameterized by the arclength s from the projection apex and azimuthal angle ϕ (Fig. 2.1E). The shape of the projection is characterized by its local radius, $r(s,t)$, and the principal curvatures $\kappa_s = \partial\theta/\partial s$ and $\kappa_\phi = \sin\theta/r$, respectively, where $\theta(s,t)$ is the angle between the local outward normal and the axis of growth (Fig. 2.1E). The coordinates (r,ϕ,z) (Fig. 2.1E) are standard cylindrical coordinates, and the angle θ and arclength s parameterize changes in normal and tangential directions of the surface, $\hat{n}$ and $\hat{s}$ respectively [23, 74] (Fig. 2.1E). The time evolution of the mating projection shape is governed by the mechanics and assembly of the cell wall, as described below.

2.2.1 Cell wall mechanics and extension

Building on previous work combining cell wall mechanics and growth in tip-growing cells [23], as well as on the expansion of thin viscous shells [74], we write the equations

governing the dynamics of the growing cell wall. Local normal force balance at the cell wall reads

$$\sigma_{\rm ss}\kappa_{\rm s} + \sigma_{\phi\phi}\kappa_{\phi} = P \quad \text{and} \quad \sigma_{\rm ss}\kappa_{\phi} = \frac{P}{2}\,, \tag{2.1}$$

where $\sigma_{\rm ss}(s,t)$ and $\sigma_{\phi\phi}(s,t)$ are the tensions along s and ϕ in the wall (Fig. 2.1F). The expansion of the cell wall during growth is caused by the tensions and depends on the mechanical properties (rheology) of the cell wall, which govern the response of the cell wall to applied stresses. Although the yeast cell wall behaves elastically at short time scales (seconds [72]), it expands irreversibly on the characteristic timescales of mating projection growth (minutes [20]), revealing a fluid-like behavior of the cell wall in growing regions. The transition between fluid-like behavior at the growing apical region to an elastic behavior far away from the apex has been studied in other systems and it is believed to be controlled by an increasing concentration of cross-links between wall polymers away from the tip [75, 76]. This is consistent with the higher concentration of cell wall degrading enzymes (glucanases) in the apical region of the mating projection [77]. We therefore assume the cell wall of the growing mating projection to behave as an inhomogeneous viscous fluid, with spatially varying viscosity $\mu(s)$, minimal at the apex and increasing away from it (Fig. 2.1F). The local tangential velocity $u(s,t)$ of a cell wall with constant density $\rho_{\rm w}$, or its strain (expansion) rates $\dot{\epsilon}_{\rm s} = \partial u/\partial s$ and $\dot{\epsilon}_{\phi} = (1/r)(dr/dt)$ equivalently, can be minimally related to the tensions in the wall by [23, 74]

$$\sigma_{\rm ss} = 4\mu h\,[\dot{\epsilon}_{\rm s} + \dot{\epsilon}_{\phi}/2] \quad \text{and} \quad \sigma_{\phi\phi} = 4\mu h\,[\dot{\epsilon}_{\rm s}/2 + \dot{\epsilon}_{\phi}]\ . \tag{2.2}$$

2.2.2 Dynamics of cell wall assembly

Sustained expansion of the cell wall during mating projection growth requires constant assembly of new cell wall material in the expanding apical region (Fig. 2.1B-C,F). Cell wall assembly occurs through synthesis of the primary component of the wall, 1,3-β glucan [72], by transmembrane 1,3-β glucan synthases Fks1/2, which localize at the apical, growing region of the mating projection [78, 79]. While only inactive Fks1/2 molecules, unable to synthesize glucans, are incorporated to the plasma membrane through exocytosis, Fks1/2 can be activated by Rho1 once at the plasma membrane [80] (Fig. 2.1C,D). The activated form of Fks1/2 synthases extrudes 1,3-β glucan chains into the extracellular space, thereby assembling new cell wall onto the preexisting wall [45]. Accounting for these events, mass conservation of cell wall material yields

$$\partial_t(rh) + \partial_s(rhu) = \frac{r m_{\mathrm{m}} k_{\mathrm{p}}}{\rho_{\mathrm{w}}}\, \rho_{\mathrm{A}}(s,t)\,, \tag{2.3}$$

where $h(s,t)$ is the cell wall thickness (Fig. 2.1E), and m_m and k_p are the mass of a 1,3-β glucan monomer and the 1,3-β glucan assembly rate by Fks1/2 synthases, respectively. For simplicity, we assume that the assembly rate of new cell wall material is proportional to the local surface density ρ_{A} of active Fks1/2. Given that Fks1/2 synthases are constantly added and removed from the plasma membrane by exo- and endo-cytosis, it is important to consider their dynamics.

Inactive Fks1/2 are transported to the apical region of the mating projection by the cells exocytic machinery and incorporated to the plasma membrane via exocytosis [81] (Fig. 2.1C). Once on the membrane, inactive Fks1/2 molecules, characterized by a local

density ρ_I, can be activated at a rate k_{on}. Due to the relatively fast exo- and endocytosis Fks1/2 recycling ($\sim$ 1s [82]) and very low diffusion constant D of proteins on yeast membranes ($D \sim 0.01\,\mu\text{m}^2/\text{s}$ [83]), the diffusive movement of inactive Fks1/2 on the plasma membrane can be neglected. In the active state, Fks1/2 extrudes new 1,3-β glucan chains into the wall, which get assembled into the preexisting 1,3-β glucan network, effectively attaching active Fks1/2 to the wall and leading to a wall-driven convective movement of active Fks1/2 with velocity u. Finally, active Fks1/2 synthases become inactive at a rate k_{off} (Fig. 2.1C). The dynamics for both inactive and active Fks1/2 states can be written in the curved geometry of the cell as

$$\begin{aligned} &\partial_t(\rho_{\text{I}} r) = r[k_{\text{off}}\rho_{\text{A}} - k_{\text{on}}\rho_{\text{I}}] + r[k_{\text{X}}\rho_0 - k_{\text{D}}\rho_{\text{I}}]\,, \\ &\partial_t(\rho_{\text{A}} r) + \partial_s(\rho_{\text{A}} r u) = r[k_{\text{on}}\rho_{\text{I}} - k_{\text{off}}\rho_{\text{A}}]\,, \end{aligned} \tag{2.4}$$

where k_{X} and k_{D} are the exocytosis and endocytosis rates, respectively. Experimental observations of the spatial distribution of both exocytic and endocytic events during mating projection growth indicate that these are maximal at the apex and decay away from it [82]. These localized exo- and endo-cytosis profiles are characterized by a decay length scale and can be written as $k_{\text{X}}(s,t) = k_{\text{X}}^0 \exp(-s^2/\lambda_{\text{X}}^2)$ and $k_{\text{D}}(s,t) = k_{\text{D}}^0 \exp(-s^2/\lambda_{\text{D}}^2)$, where k_X^0 and k_D^0 are the apical rates of exocytosis and endocytosis, respectively, and λ_X and λ_D are the length scales over which exocytosis and endocytosis decay, respectively. Given that the enzymes that locally degrade the cell wall and control its mechanical properties are secreted through exocytosis [84], we assume the length scale of viscosity variation to be set by the exocytosis length scale and write the viscosity profile as $\mu(s) = \mu_0 \exp(s^2/\lambda_{\text{X}}^2)$.

In order to simultaneously solve for the mechanics of cell wall expansion and the dynamics of cell wall assembly described above, it is necessary to specify the activation and inactivation rates of membrane-localized Fks1/2 cell wall synthases, k_{on} and k_{off}, respectively. Inactivation of active, membrane-localized Fks1/2 synthases has been largely unexplored and assumed here to occur at a constant rate. The activation of inactive Fks1/2 is mediated by the GTPase Rho1 through the CWI pathway [59, 63, 51] (Fig. 2.1D), providing a direct coupling between the local mechanical state of the wall and the local cell wall synthesis machinery via the Fks1/2 activation rate k_{on} (Fig. 2.1D). To account for this coupling, we write the Fks1/2 activation rate k_{on} as dependent on the cell wall mechanical state, namely

$$k_{\text{on}} = \Gamma \left[\dot{\epsilon}_{\text{s}} + \dot{\epsilon}_{\phi}\right], \tag{2.5}$$

where we assumed the stress sensors to perceive the expansion (strain) rate in the wall, rather than strain or stress. Indeed, activation of cell wall synthases should not occur in the absence of cell wall expansion, as it could otherwise lead to uncontrolled cell wall thickening. Eqn. 2.5 constitutes a direct *mechanical feedback of cell wall mechanics on cell wall assembly*, with the dimensionless parameter Γ establishing the strength of the mechanical feedback: large values of Γ indicate that low levels of cell wall expansion trigger large activation of Fks1/2 synthases, and vice versa.

Combining equations. 2.1-2.5 and the profiles of exocytosis, endocytosis and wall viscosity described above, we solve the coupled dynamics of cell wall mechanical expansion and assembly. Normalizing all variables, we find 5 dimensionless parameters that control

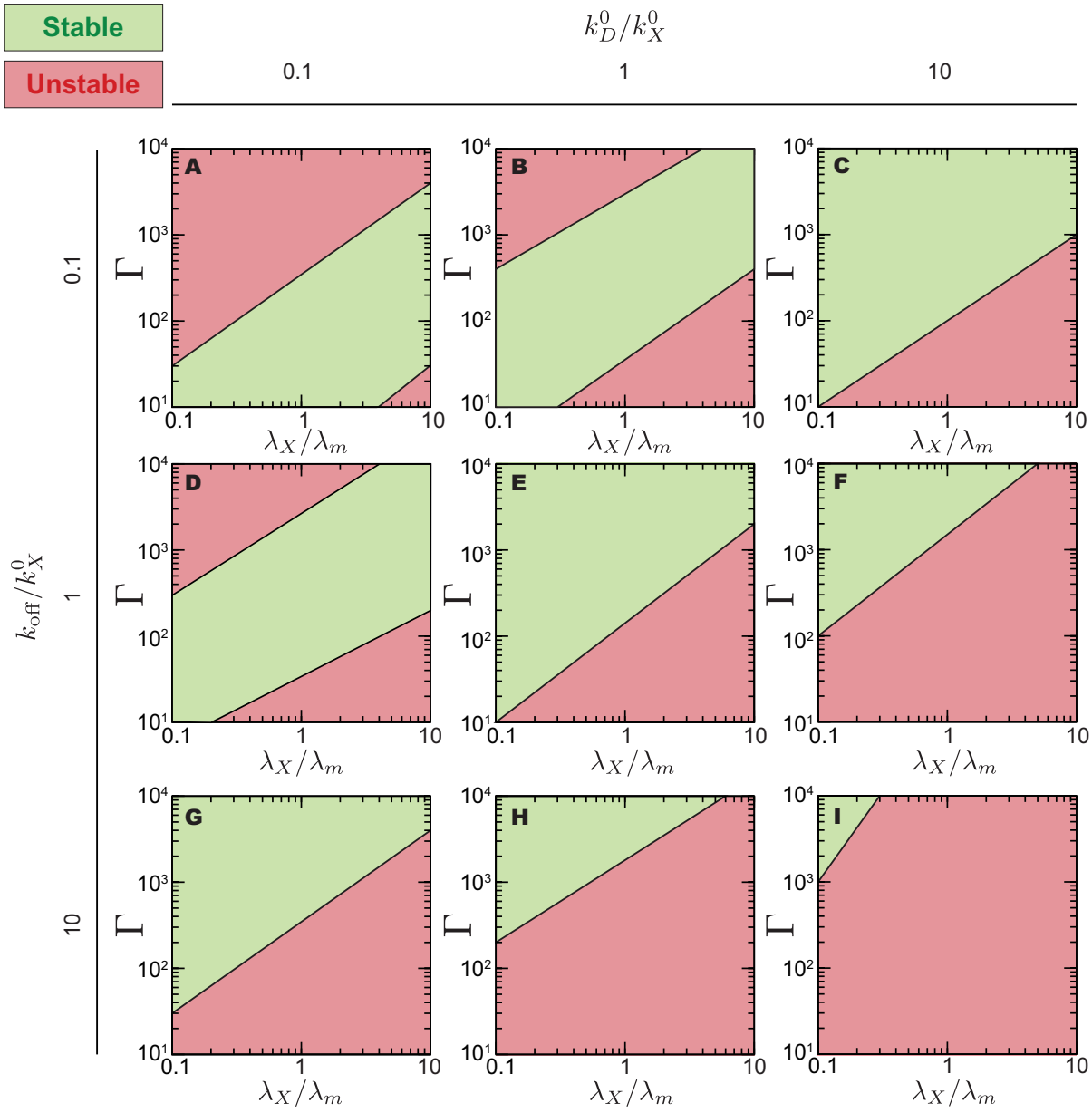

Figure 2.2: **Dynamical regimes** Parameter space spanned by Γ and $\lambda_{\rm X}/\lambda_{\rm m}$ (A-I) for different values of the parameters k_D^0/k_X^0 and $k_{\rm off}/k_X^0$. The transition from unstable growth (red) to stable growth (green) exists in all cases.

the dynamical regimes of the system (Table 2.2.2), namely $k_{\rm off}/k_{\rm X}^0$, $k_{\rm D}^0/k_{\rm X}^0$, $\lambda_{\rm D}/\lambda_{\rm X}$, Γ, and the ratio $(P\rho_{\rm w}\lambda_{\rm X})/(12\,\mu_0 m_{\rm w}\rho_0 k_{\rm p})$, which corresponds to the ratio $\lambda_{\rm X}/\lambda_{\rm m}$ of the exocytosis length scale $\lambda_{\rm X}$ and a length scale $\lambda_{\rm m} \equiv 12\,\mu_0 m_{\rm w}\rho_0 k_{\rm p}/P\rho_{\rm w}$ set by the expansion

mechanics of the cell wall.

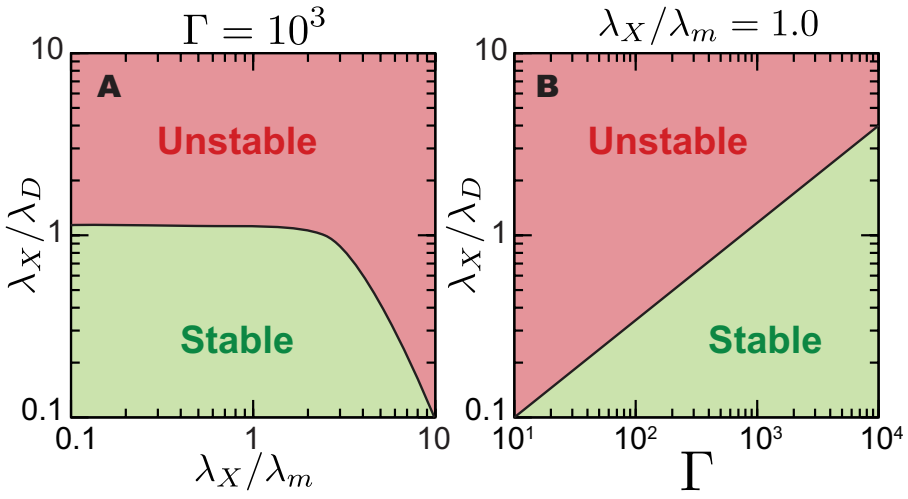

Figure 2.3: **Dynamical regimes as the ratio of lengthscales of exocytosis and endocytosis is varied** Transition from unstable (red) growth to stable (green) growth exists in all cases.

The parameters $k_{\rm off}/k_{\rm X}^0$, $k_{\rm D}^0/k_{\rm X}^0$, $\lambda_{\rm D}/\lambda_{\rm X}$ have either been measured or estimated and we use below their known values [85, 82] (Table B in Appendix A); variations in these parameters do not qualitatively affect our results. We vary the parameters held constant in the main text within a reasonable range and determine the dynamical regimes. Since our theoretical predictions and experimental results indicate that the instability occurs as the pressure is increased or the mechanical feedback decreased, we explore if this behavior is robust as we vary all other parameters. Varying the parameters k_D^0/k_X^0 and $k_{\rm off}/k_X^0$ by two orders of magnitude (from 0.10 to 10) does not change our qualitative results (Fig. 2.2): there is transition between stable and unstable states, and the critical value of the mechanical feedback strength increases with $\lambda_{\rm X}/\lambda_{\rm m}$. Varying λ_X/λ_D leads also to the same qualitative results (Fig. 2.3).

In contrast, the feedback strength Γ and the ratio $(P\rho_{\rm w}\lambda_{\rm X})/(12\,\mu_0 m_{\rm w}\rho_0 k_{\rm p})$ are un-

known and we explore below the dynamical regimes of the system when these parameters are varied.

Dimensionless parameters				
$\frac{P\rho_{\mathrm{w}}\lambda_{\mathrm{X}}}{12\,\mu_0 m_{\mathrm{w}}\rho_0 k_{\mathrm{p}}}$	Γ	$\frac{k_{\mathrm{off}}}{k_{\mathrm{X}}^0}$	$\frac{k_{\mathrm{D}}^0}{k_{\mathrm{X}}^0}$	$\frac{\lambda_{\mathrm{D}}}{\lambda_{\mathrm{X}}}$
Physical/Chemical parameters				
Parameter	Description	Parameter	Description	
P	Turgor pressure of budding yeast	λ_X	Exocytosis length-scale	
ρ_w	Density of 1,3-β glucans in cell wall	λ_D	Endocytosis length-scale	
μ_0	Apical viscosity of cell wall	k_X^0	Apical rate of exocytosis	
m_w	Mass of 1,3-β glucan monomer	k_D^0	Apical rate of endocytosis	
ρ_0	Density of Fks1/2 enzymes in vesicle	k_{off}	Inactivation rate of Fks1/2	
k_p	Extrusion rate of 1,3-β glucan monomers			

Table 2.1: System physical parameters and relevant dimensionless parameters

Numerical integration of governing equations

The system of equations 2.1-2.5 was scaled and written in a manner such that r, h, ρ_A, and ρ_I were described by equations evolving in time, and u, θ, κ_{s} by differential equations in s. The latter equations were solved by the method of lines; s was discretized and the s-derivatives were written as a differential matrix using fourth order central difference and one sided finite differences at the boundary. The resulting system becomes a differential algebraic system (DAE), which was solved using Sundials, a suite of nonlinear and DAE solvers. Steady state solutions were obtained by ensuring that all time derivatives of scaled variables were below 10^{-3}.

2.3 Stability of mating projection growth

In the absence of mechanical feedback ($\Gamma = 0$),the equation 2.4 cannot lead to projection growth because Fks1/2 synthases cannot be activated and, consequently, there is no cell wall assembly at all. To study the system in the absence of mechanical feedback ($\Gamma = 0$), but in the presence of cell wall assembly, we only consider an active Fks1/2 state, with Fks1/2 molecules incorporated to the plasma membrane via exocytosis and removed from it via endocytosis. As Fks1/2 molecules are always active in this limiting case, they directly contribute to the assembly of the cell wall and their dynamics is fully decoupled from the cell wall mechanics, namely

$$\partial_t(\rho_A r) + \partial_s(\rho_A r u) = r[k_X \rho_0 - k_D \rho_A]\,. \tag{2.6}$$

Eqns. 2.1-2.3 and Eq. 2.6, together with the profiles of exocytosis, endocytosis and wall viscosity described in the main text, describe the coupled dynamics of cell wall mechanical expansion and assembly in the absence of mechanical feedback. Normalizing all variables, we obtain the relevant dimensionless parameters, namely $k_{\mathrm{D}}^0/k_{\mathrm{X}}^0$, $\lambda_{\mathrm{X}}/\lambda_{\mathrm{D}}$, and the ratio $(P\rho_{\mathrm{w}}\lambda_{\mathrm{X}})/(12\,\mu_0 m_{\mathrm{w}}\rho_0 k_{\mathrm{p}})$, which corresponds to the ratio $\lambda_{\mathrm{X}}/\lambda_{\mathrm{m}}$ of the exocytosis length scale λ_{X} and a length scale $\lambda_{\mathrm{m}} \equiv 12\,\mu_0 m_{\mathrm{w}}\rho_0 k_{\mathrm{p}}/P\rho_{\mathrm{w}}$ set by the expansion mechanics of the cell wall.

We numerically integrate the dynamics of the system in the absence of feedback and find that no stable states exist for varying values of k_D^0/k_X^0 and λ_X/λ_m and fixed $\lambda_X/\lambda_D = 0.5$ or for λ_X/λ_D and λ_X/λ_m fixed $k_D^0/k_X^0 = 1.0$ (Fig. 2.4A,B). No stable states were found over a two order of magnitude variation of the parameters around their

unit values. The instability is caused by either the progressive thinning or thickening of the cell wall, depending on the region of the parameters space (Fig. 2.4A,B). Cell wall thinning eventually leads to the piercing of the cell wall at the apex ($h(s = 0, t_p) = 0$) at a finite time t_p (Fig. 2.4C). In other regions of the parameters space, the apical cell wall progressively thickens without bound (Fig. 2.4D). The presence of a mechanical feedback is therefore crucial for the stable growth of the mating projection. In the absence of a mechanical feedback there is a lack of coordination between cell wall expansion and wall assembly, making it impossible for the cell wall synthesis machinery (Fks1/2) to appropriately balance cell wall expansion because it does not have information about its mechanical state.

In the presence of mechanical feedback ($\Gamma > 0$), numerical integration of Eqns. 2.1-2.5 (Methods) shows that stable states of mating projection growth can be sustained for a large range of parameters (Fig. 2.5B and 2.5). In this context, stable states refer to

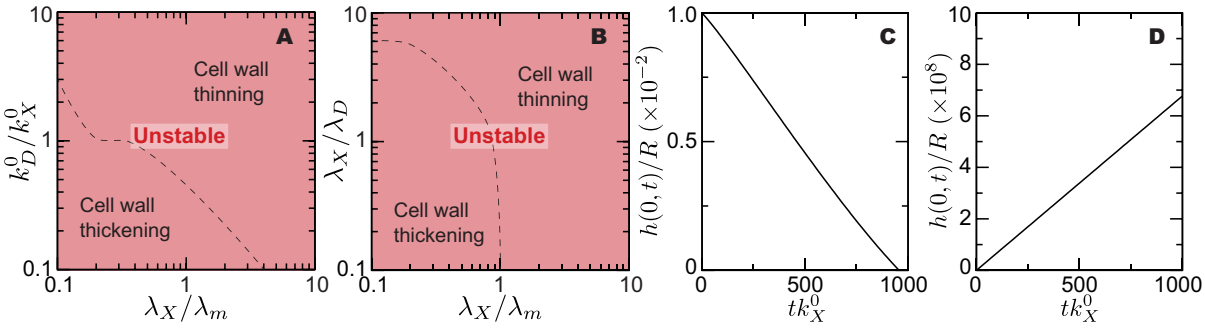

Figure 2.4: **Mating projection growth is always unstable in the absence of mechanical feedback.** (A) No stable solutions exist as k_D^0/k_X^0 and λ_X/λ_m are varied and $\lambda_X/\lambda_D = 0.5$. (B) No stable solutions exist as λ_X/λ_D and λ_X/λ_m are varied and $k_D^0/k_X^0 = 1.0$. (C) Progressive thinning of the apical cell wall ($h(s = 0, t)$), eventually leading to the piercing of the cell wall at the apex. (D) Progressive, unbounded thickening of the apical cell wall.

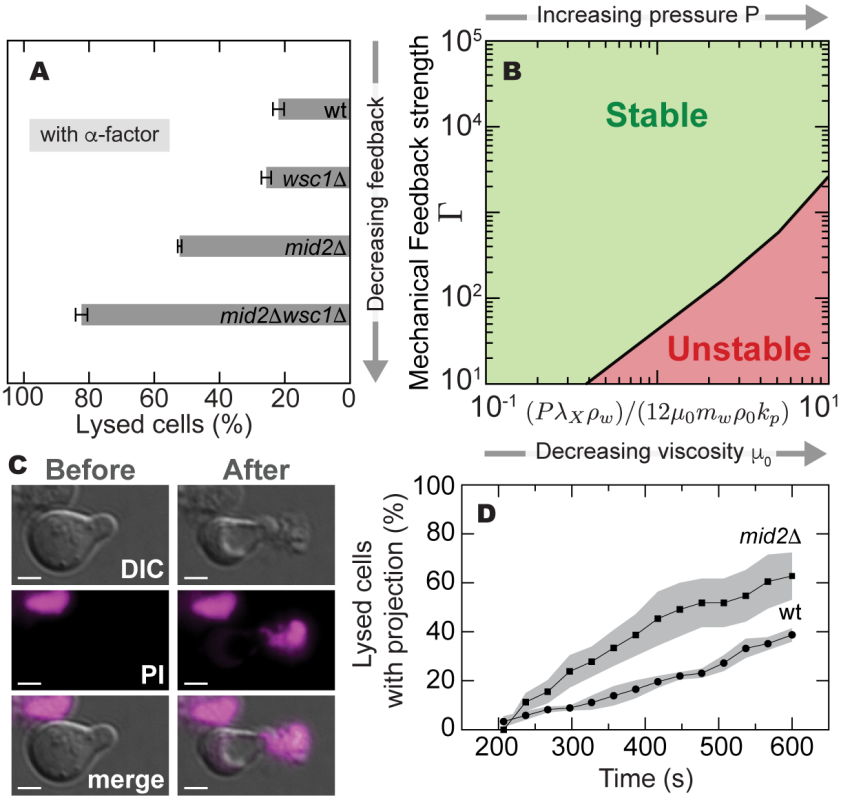

Figure 2.5: **Effect of mechanical feedback strength and turgor pressure on cell viability.** The strength of mechanical feedback, Γ, is experimentally varied by deleting *MID2* and *WSC1*. The dimensionless parameter $(P\rho_{\mathrm{w}}\lambda_{\mathrm{X}})/(12\,\mu_0 m_{\mathrm{w}}\rho_0 k_{\mathrm{p}})$ is varied by changing the osmolarity of the external medium through dilution of the yeast growth media, YPD, in deionized H_2O, effectively increasing turgor pressure P in cells. Cell lysis was measured using the PI staining viability assay (Methods). (A) Percent of lysed cells in *mid2Δ* and *wsc1Δ* mutants, as well as the *mid2Δwsc1Δ* double mutant, when grown in the presence of α-factor in YPD. (B) Theoretically predicted dynamical regimes for varying values of the mechanical feedback strength Γ and the ratio $(P\rho_{\mathrm{w}}\lambda_{\mathrm{X}})/(12\,\mu_0 m_{\mathrm{w}}\rho_0 k_{\mathrm{p}})$. Decreasing osmolarity experimentally, corresponds to increasing P and, therefore, moving along horizontal lines in the positive direction. Addition of zymolyase, a cell wall degrading enzyme, corresponds to decreasing the cell wall viscosity, moving also along horizontal lines in the positive direction. (C) Images (DIC, PI staining and merge) showing the moments before and after the piercing of the cell wall at the tip of a mating projection and subsequent cell lysis of a *mid2Δ* cell after the addition of zymolyase. Scale bar, 2μm. (D) Temporal increase in the fraction of pierced mating projections for both *mid2Δ* (squares) and WT (circles) cells after addition of zymolyase.

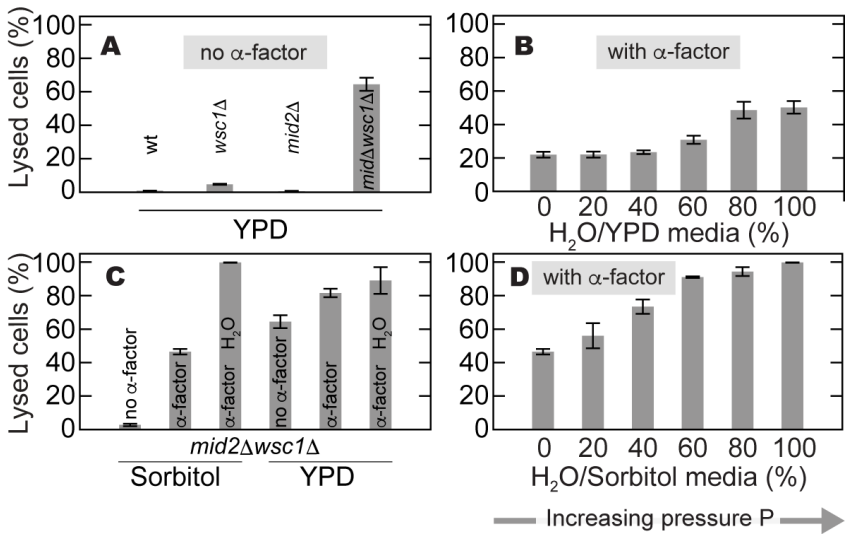

Figure 2.6: **Effect of mechanical feedback strength and turgor pressure on cell viability.** The strength of mechanical feedback, Γ, is experimentally varied by deleting *MID2* and *WSC1*. The dimensionless parameter $(P\rho_{\mathrm{w}}\lambda_{\mathrm{X}})/(12\,\mu_0 m_{\mathrm{w}}\rho_0 k_{\mathrm{p}})$ is varied by changing the osmolarity of the external medium through dilution of the yeast growth media, YPD, in deionized H_2O, effectively increasing turgor pressure P in cells. Cell lysis was measured using the PI staining viability assay (Methods). (A) Percent of lysed cells in the absence of α-factor for WT, *mid2Δ* and *wsc1Δ* mutants, as well as the *mid2Δwsc1Δ* double mutant. (B) Percent of WT lysed cells when grown in the presence of α-factor in YPD medium with decreasing osmolarity. (C) Percent of *mid2Δwsc1Δ* lysed cells when grown both in the presence and absence of α-factor in YPD, in osmotically supported conditions (YPD + 1M sorbitol), as well as in hypo-osmotic conditions (100% H_2O). (D) Percent of *mid2Δwsc1Δ* lysed cells when grown in the presence of α-factor and osmotically supported media (YPD + sorbitol), diluted for decreasing osmolarities.

sustained steady state growth of the mating projection at constant velocity. For any given value of the ratio $(P\rho_{\mathrm{w}}\lambda_{\mathrm{X}})/(12\,\mu_0 m_{\mathrm{w}}\rho_0 k_{\mathrm{p}})$ there exists a critical value of the feedback strength Γ below which mating projection growth is unstable. Similarly, for every value of the feedback strength Γ, there is a maximal value of $(P\rho_{\mathrm{w}}\lambda_{\mathrm{X}})/(12\,\mu_0 m_{\mathrm{w}}\rho_0 k_{\mathrm{p}})$ above which mating projection growth becomes unstable. This instability is caused by the progressive thinning of the apical cell wall, eventually causing the piercing of the cell and leading to cell lysis. The bifurcation between stable and unstable states characterizes the

transition between stably growing mating projections and a situation in which this stable growth cannot be sustained because of the progressive thinning of the cell wall and its eventual piercing. This instability threshold (bifurcation) is equivalent to the existence of a maximal turgor pressure (or a minimal viscosity), above (below) which the cell wall progressively thins and eventually pierces at the tip of the projection, leading to cell lysis. The predicted increase of the maximal turgor pressure or decrease in the minimal wall viscosity for increasing feedback strength Γ indicates that cells with compromised mechanical feedback should be more sensitive to both an increase in turgor pressure or a decrease in wall viscosity than WT cells.

In order to experimentally explore the predicted dynamical regimes (Fig. 2.5B, Fig, 2.2, Fig, 2.3), we systematically varied the mechanical feedback strength, as well as the turgor pressure P and cell wall viscosity μ_0. In contrast to previous works, here we examine all three perturbations in the context of the stability of pheromone-induced projection growth. We first varied the feedback strength Γ by compromising the ability of the cell to sense the mechanical state of the wall. To this end, we genetically deleted the two primary cell wall stress sensors present during mating projection growth, namely Wsc1 and Mid2 [63] (Fig. 2.1D), and measured the resulting cell lysis (Methods). Only in the presence of α-factor and mating projection growth, did the deletion of either of the two sensors (Mid2, Wsc1) lead to increased levels of cell lysis compared to WT (Fig. 2.5A,2.6A), as predicted theoretically (Fig. 2.5B), indicating that the ability to sense the mechanical state of the wall is essential during growth. Moreover, the double

mutant *mid2Δwsc1Δ* exhibited the highest level of cell lysis in α-factor and, even when osmotically supported by 1M sorbitol, showed a substantial increase in lysis after the addition of α-factor (Fig. 2.5E,2.6A,C). These observations show that the double mutant has an enhanced sensitivity to the addition of mating pheromone, in agreement with previous results obtained during vegetative growth [70]. To explore how changes in the parameter $(P\rho_{\mathrm{w}}\lambda_{\mathrm{X}})/(12\,\mu_0 m_{\mathrm{w}}\rho_0 k_{\mathrm{p}})$ affected cell viability (Fig. 2.5B), we independently changed the turgor pressure P and the cell wall viscosity μ_0. To increase the cell's turgor pressure P, we progressively decreased the osmolarity of the external medium (Methods). We observed a monotonic increase in lysed cells for both WT and *mid2Δwsc1Δ* cells as media osmolarity was decreased in the presence of α-factor (Fig. 2.6B,D), consistent with the theoretically predicted effect of increased turgor pressure P (Fig. 2.5B). Finally, in order to decrease the cell wall viscosity μ_0, thereby increasing the value of the parameter $(P\rho_{\mathrm{w}}\lambda_{\mathrm{X}})/(12\,\mu_0 m_{\mathrm{w}}\rho_0 k_{\mathrm{p}})$ (Fig. 2.5B), we added zymolyase to the culture media (Methods). Zymolyase enzymatic activity degrades 1,3-β glucans in the cell wall, effectively lowering the cell wall viscosity. Addition of zymolyase led to the piercing of the cell wall typically at the tip of the mating projection (Fig. 2.5C and Supplementary Video), as expected theoretically (Fig. 2.5B). Since zymolyase will continuously degrade the cell wall, leading to the eventual piercing and lysis of all cells, we studied the temporal increase in pierced cells. Our results indicate that *mid2Δ* cells with reduced mechanical feedback pierced faster than WT cells when grown at the same zymolyase concentration (Fig. 2.5D), as theoretically expected (Fig. 2.5B). Overall, our experimental results are in

agreement with our theoretical predictions (Fig. 2.5B) and are consistent with the CWI pathway providing the necessary mechanical feedback to coordinate cell wall expansion and assembly.

2.4 Characteristics of stably growing mating projections

Stable, steady-state solutions for mating projection growth show that the shape of the mating projection is largely insensitive to variations in the feedback strength Γ and the ratio $(P\rho_{\mathrm{w}}\lambda_{\mathrm{X}})/(12\,\mu_0 m_{\mathrm{w}}\rho_0 k_{\mathrm{p}})$ (Fig. 2.7A-B,E-F). The size (radius) R of the mating projection increases linearly with the size of the exocytosis region λ_{X}, but it is independent from the feedback strength Γ (Fig. 2.7B). Beyond projection shape and size, the cell wall expansion rate, $\dot{\epsilon}_{\mathrm{s}} + \dot{\epsilon}_{\phi}$, is always maximal at the projection apex ($s = 0$) and decreases away from it (Fig. 2.7C), eventually vanishing as no wall expansion occurs far away from the growing apical region. The cell wall expansion rate at the projection apex, $(\dot{\epsilon}_{\mathrm{s}}+\dot{\epsilon}_{\phi})|_{s=0}$, increases with increasing turgor pressure (or $(P\rho_{\mathrm{w}}\lambda_{\mathrm{X}})/(12\,\mu_0 m_{\mathrm{w}}\rho_0 k_{\mathrm{p}})$ equivalently) and with decreasing mechanical feedback strength (Fig. 2.7C-D). In contrast, the apical cell wall thickness displays the opposite behavior (Fig. 2.7G-H), decreasing for increasing P or decreasing Γ. These results indicate that cells closer to the instability threshold display stronger apical cell wall expansion rates and thinner cell wall (Fig. 2.5A and Fig. 2.7D,H), suggesting the strong cell wall expansion and thinning at the apex as

the cause of the loss in cell wall mechanical stability.

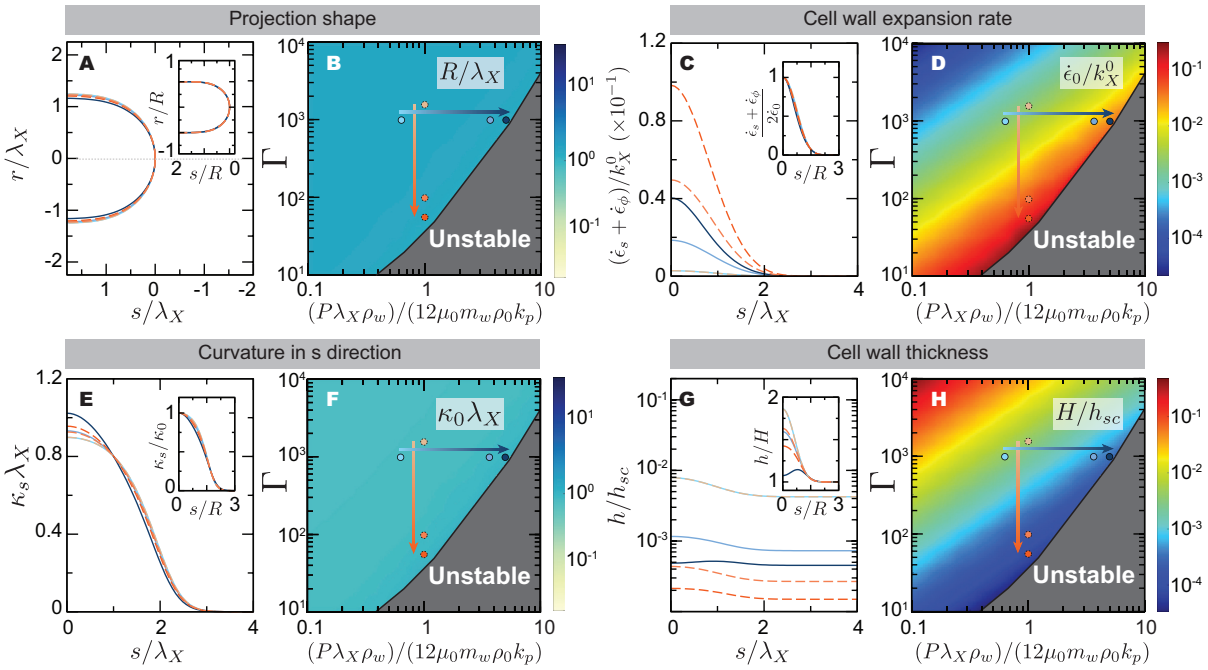

Figure 2.7: **Steady-state stable solutions for mating projection growth: Projection shape and cell wall expansion.** (A,C,E,G) Mating projection shape (A), as well as the spatial profiles of the cell wall expansion rate $\dot{\epsilon}_\mathrm{s} + \dot{\epsilon}_\phi$ (C), curvature κ_s (E) and cell wall thickness h (G), for different values of the mechanical feedback strength Γ and the ratio $\lambda_\mathrm{X}/\lambda_\mathrm{m} = (P\rho_\mathrm{w}\lambda_\mathrm{X})/(12\,\mu_0 m_\mathrm{w}\rho_0 k_\mathrm{p})$. All insets show a different scaling of each magnitude, with the arclength normalized by the projection radius R and each quantity normalized by its value at the projection tip ($s = 0$), with the exception of the wall thickness $h(s)$ and the shape $r(s)$, which are normalized by the limiting values far away from the apical region, H and R respectively. The color code indicates the different parameter values, shown as dots of the same color in the parameter space right to each panel. Increasing orange and blue tones of the dots corresponds to decreasing Γ and increasing $(P\rho_\mathrm{w}\lambda_\mathrm{X})/(12\,\mu_0 m_\mathrm{w}\rho_0 k_\mathrm{p})$, respectively (arrows in Fig. 2.5A). (B,D,F,H) The variation of the apical value of each magnitude, namely $\dot{\epsilon}_0 \equiv \dot{\epsilon}_\mathrm{s}(s = 0) = \dot{\epsilon}_\phi(s = 0)$ (D) and $\kappa_0 \equiv \kappa_s(s = 0)$ (F), is shown for the different values of the parameters for which stable states exist. The variation of the projection radius and wall thickness away from the apical region, R (B) and H (H) respectively, are shown as a function of the parameters as well.

Regarding cell wall assembly during stable, steady-state projection growth, our theoretical results indicate maximal cell wall assembly at the expanding apical region. Both

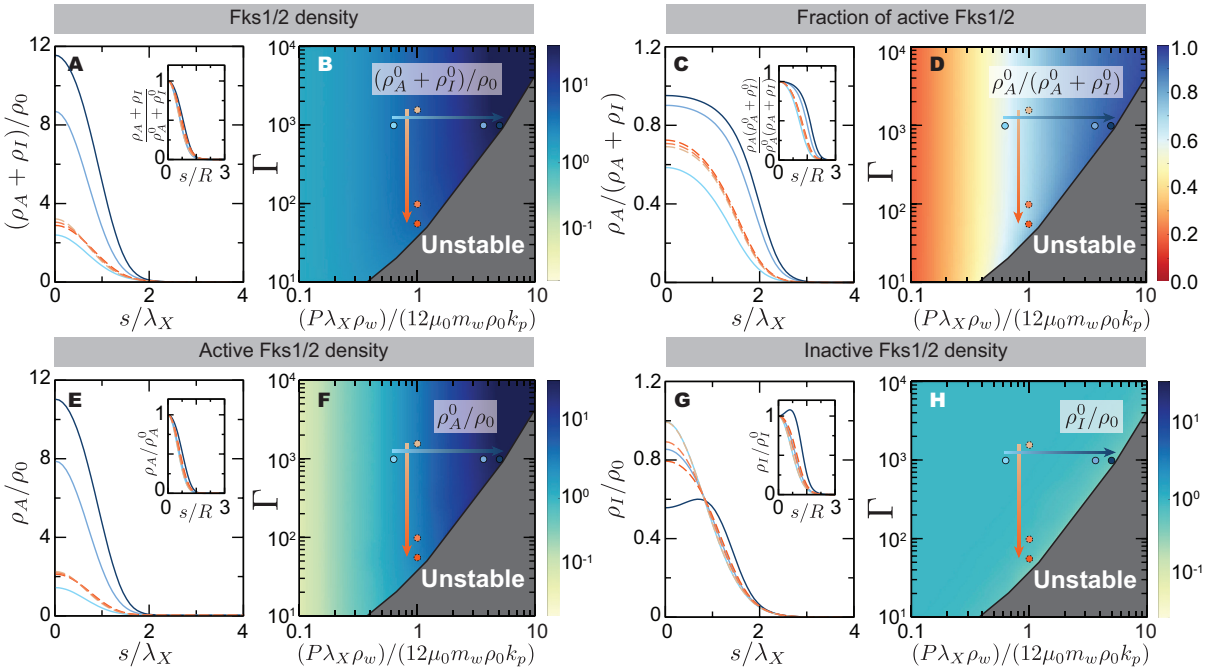

Figure 2.8: **Steady-state stable solutions for mating projection growth: Cell wall assembly via Fks1/2.** Cell wall assembly via Fks1/2. (A,C,E,G) Total Fks1/2 density $\rho_A + \rho_I$ (A), fraction of active Fks1/2, $\rho_A/(\rho_A + \rho_I)$ (C), active Fks1/2 density (E) and inactive Fks1/2 density (E), for different values of the mechanical feedback strength Γ and the ratio $\lambda_\mathrm{X}/\lambda_\mathrm{m} = (P\rho_\mathrm{w}\lambda_\mathrm{X})/(12\,\mu_0 m_\mathrm{w}\rho_0 k_\mathrm{p})$. All insets show a different scaling of each magnitude, with the arclength normalized by the projection radius R and each quantity normalized by its value at the projection tip ($s = 0$). The color code indicates the different parameter values, shown as dots of the same color in the parameter space right to each panel. Increasing orange and blue tones of the dots corresponds to decreasing Γ and increasing $(P\rho_\mathrm{w}\lambda_\mathrm{X})/(12\,\mu_0 m_\mathrm{w}\rho_0 k_\mathrm{p})$, respectively (arrows in Fig. 2.5A). (B,D,F,H) The variation of the apical value of each magnitude, namely $(\rho_A^0 + \rho_I^0)/\rho_0$ (B), $\rho_A^0/(\rho_A^0 + \rho_I^0)$ (D), ρ_A^0/ρ_0 (F) and ρ_I^0/ρ_0 (H), is shown for the different values of the parameters for which stable states exist.

the total surface density of Fks1/2 synthases, $\rho_A + \rho_I$, and the surface density of only active Fks1/2 synthases, ρ_A, are maximal at the apex and decrease away from it until they vanish (Fig. 2.8A-B,E-F), as expected from the apically-localized exo- and endocytosis profiles. The apical value of the total (or only active) Fks1/2 surface density, namely $\rho_A^0 + \rho_I^0$ (or ρ_A^0), can be either smaller or larger than the surface density ρ_0 of

Fks1/2 synthases secreted by exocytic vesicles (Fig. 2.8A-B,E-F). The reason why the total Fks1/2 surface density $\rho_A^0 + \rho_I^0$ can be larger than ρ_0 at the apex is that active Fks1/2 is secreting 1,3-β glucans into the cell wall, a process that effectively anchors them to the wall, holding secreted Fks1/2 synthases to the tip region and increasing its concentration there. Beyond Fks1/2, anchoring transmembrane proteins to the cell wall can potentially be used as a mechanism to locally increase the protein concentration on the membrane to levels well-beyond secretion levels. The fraction of active Fks1/2, $\rho_A/(\rho_A + \rho_I)$, is also maximal at the apex and decreases away from it (Fig. 2.8C-D). This is because of mechanical feedback, which induces more Fks1/2 activation at the apex following the larger cell wall expansion rate in this region (Fig. 2.7C). Finally, the surface concentration of inactive Fks1/2 also decreases away from the expanding tip because of tip-localized exo- and endo-cytosis (Fig. 2.8G-H). Non-monotonic profiles of inactive Fks1/2 occur because high cell wall expansion rates at the tip lead to more Fks1/2 activation, leaving less inactive Fks1/2 molecules in this region. Altogether, these results indicate that at the instability threshold, the apical cell wall expansion rate becomes too large to be balanced by cell wall assembly, leading to the progressive thinning of the cell wall and cell lysis.

Analytical expressions can be obtained for the values of all variables at the apex (apical scales), but one. This is because the two principal directions defining the cell's surface become physically equivalent at the apex (as the apex is locally spherical) and, as a consequence, there are not enough boundary conditions at the apex to determine all apical scales. This can be seen from the analytical relations of the apical scales

in Table 2.4, which are defined as: $\kappa_0 \equiv \kappa_s(s=0) = \kappa_\phi(s=0)$, $h_0 \equiv h(s=0)$, $\dot{\epsilon}_0 \equiv \dot{\epsilon}_s(s=0) = \dot{\epsilon}_\phi(s=0)$, $\rho_A^0 \equiv \rho_A(s=0)$ and $\rho_I^0 \equiv \rho_I(s=0)$.

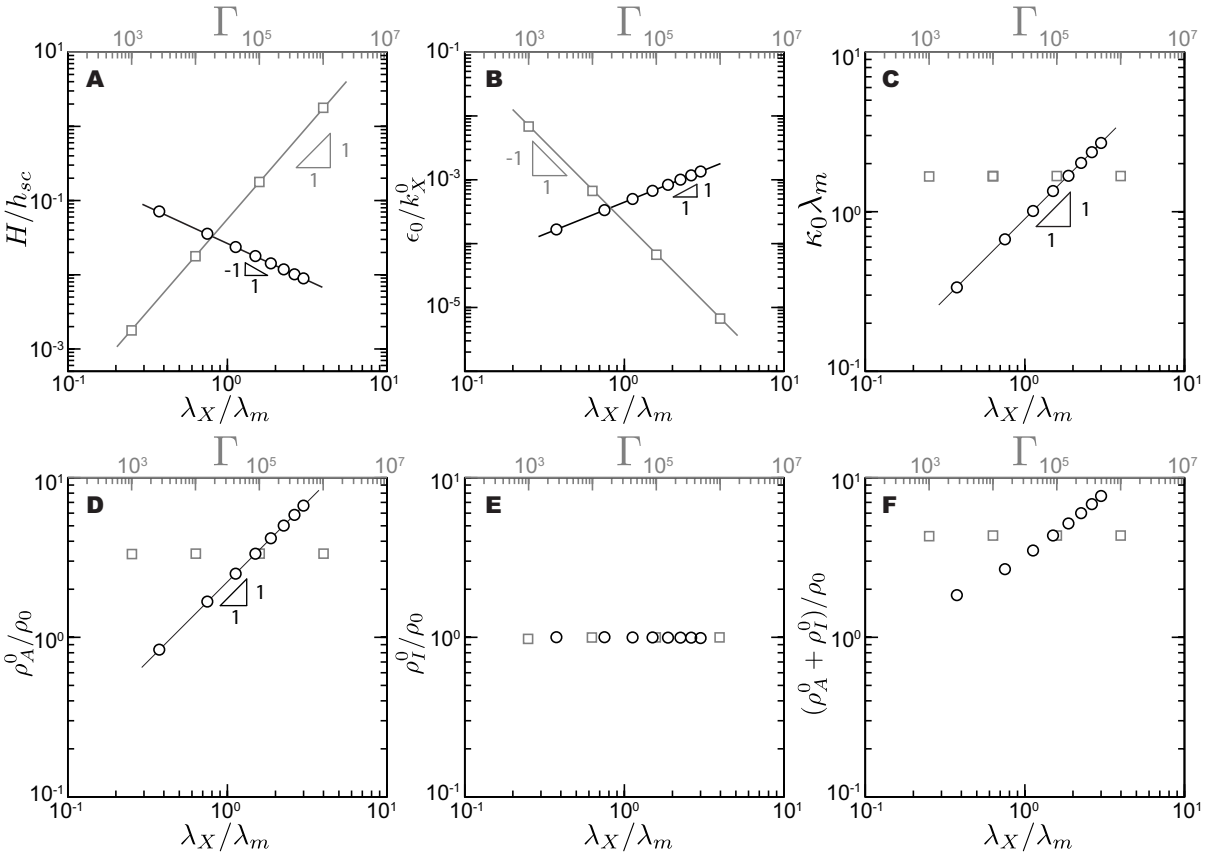

Figure 2.9: **Dependence of the apical and distal scales on Γ and λ_X/λ_m** (A) Distal thickness, H, scaled with $h_{sc} = P\lambda_X/12\mu_0 k_X^0$, (B) apical strain rate, ϵ_0 scaled with k_X^0, (C) apical curvature, κ_0 scaled with λ_m, (D) apical density of active Fks1, ρ_A^0, scaled with ρ_0, (E) apical density of inactive Fks1, ρ_A^0, scaled with ρ_0, and (F) apical density of Fks1, $\rho_A^0 + \rho_I^0$, scaled with ρ_0. Exponents of power-law behaviors are indicated.

To fully determine all the scales, it is necessary to numerically integrate the equations describing the dynamics of the system and impose boundary conditions away from the apex. In this region, the projection radius reaches a constant distal value $R \equiv r(s \to \infty)$ and the cell wall thickness reaches a constant distal value $H = h(s \to \infty)$.

Integrating numerically the equations describing the dynamics of the system in the

$h_0 = A\frac{k_p}{k_{off}}\frac{k_X^0}{k_D^0}\frac{m_w\rho_0}{\rho_w}$
$\kappa_0\dot{\epsilon}_0 = \frac{1}{A}\frac{k_D^0}{k_X^0}\frac{k_{off}}{k_p}\frac{\rho_w}{m_w\rho_0}\frac{P}{12\mu_0}$
$\rho_I^0 = \frac{k_X^0}{k_D^0}\rho_0$
$\kappa_0\rho_A^0 = \frac{P}{6\mu_0 k_p}\frac{\rho_w}{m_w\rho_0}\rho_0$

Table 2.2: System physical parameters and relevant dimensionless parameters

steady-state (see main text), we find the solutions for all the variables (see main text). We also obtain the values of all scales as the parameters Γ and the ratio $\lambda_{\rm X}/\lambda_{\rm m} = (P\rho_{\rm w}\lambda_{\rm X})/(12\,\mu_0 m_{\rm w}\rho_0 k_{\rm p})$ are varied. The scaling relations defining the dependence of the scales on the parameters Γ and $\lambda_{\rm X}/\lambda_{\rm m}$ are shown in Fig. 2.9.

The theoretical results above predict that both the geometry and size of the growing mating projection are independent from the mechanical feedback strength Γ, and that the projection radius increases with the size of the exocytosis region (Fig. 2.10A,B and Fig. 2.7A,B). To experimentally explore how exocytosis and the mechanical feedback strength affect the mating projection size R (Fig. 2.10A), we employed a deletion mutant for Spa2, a scaffold protein that localizes Bni1 and is recruited by Cdc42 [53], which displays a very wide mating projection compared to WT (Fig. 2.10C,D). We visualized the exocytosis region in both WT and *spa2Δ* cells by expressing GFP-tagged Sec3, a component of the exocyst that marks exocytic sites [86]. The exocytosis length scale $\lambda_{\rm X}$ (Fig. 2.10A), which we measured directly from confocal images (Fig. 2.10C,D and Methods), is considerably larger in *spa2Δ* mutant cells than in WT cells (Fig. 2.10E), indicating that a larger mating projection radius R is associated with a larger size of the exocytosis region. In contrast, the size R of the mating projection was not observed to

vary with changes in the strength of the mechanical feedback Γ (Fig. 2.10E), as shown by deleting Mid2 or Wsc1 in both WT and *spa2Δ* backgrounds, while simultaneously measuring the size of the mating projection R and the length of the exocytosis region using Sec3-GFP. While deletion of Wsc1 and Mid2 strongly affects mating projection stability (Fig. 2.5A), our measurements show that it does not affect the size of the mating projection (Fig. 2.10E). These results indicate that the mechanical feedback is essential to sustain stable mating projection growth, but it does not affect mating projection size, which is controlled by the exocytosis profile, as predicted theoretically (Fig. 2.10B).

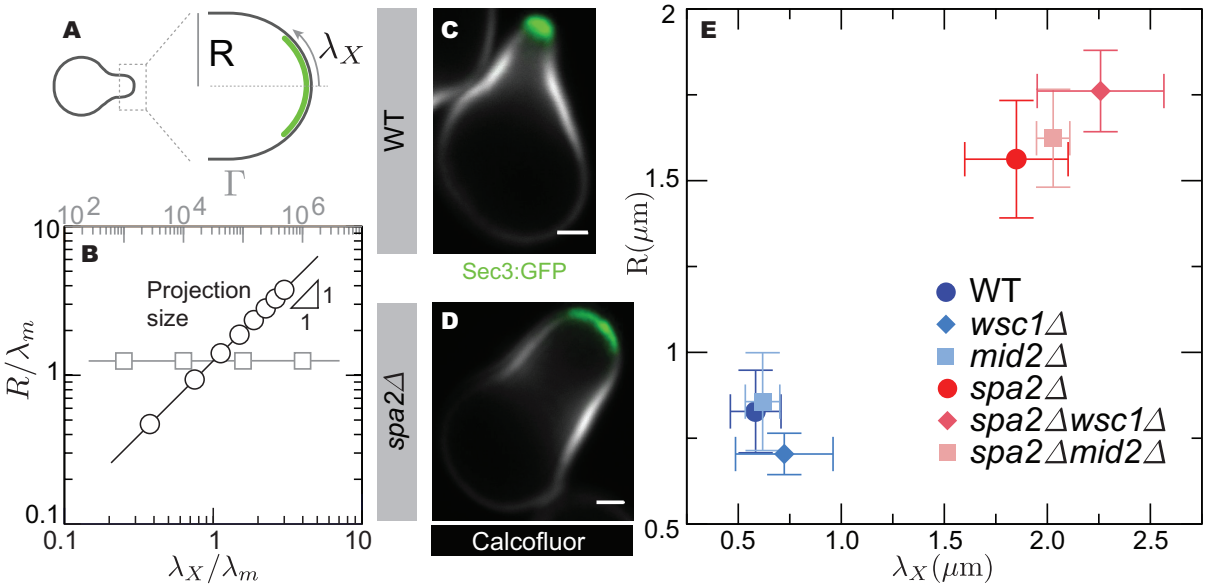

Figure 2.10: **Control of mating projection size.** (A) Diagram of a growing mating projection showing the mating projection radius R and length scale of the secretion region (green), λ_X. (B) Theoretically predicted dependence of the projection radius R with the length scale of the secretion region, λ_X, and the strength of mechanical feedback, Γ. (C-D) Confocal images of WT (C) and *spa2Δ* (D) mutant cells growing mating projections. The cell wall is labeled with calcofluor (white) and the exocytosis profile is defined by Sec3-GFP (green). Scale bar, 1 μm. (E) Measured average cell radius, R, and exocytosis length scale, λ_X, for *mid2Δ* and *wsc1Δ* mutants in both WT and *spa2Δ* backgrounds (*mid2Δ*, N=6; *wsc1Δ*, N=9; *spa2Δmid2Δ*, N=7; *spa2Δwsc1Δ*, N=6), as well as for WT (N=7) and *spa2Δ* (N=6) cells. Mean and standard deviation are shown.

2.5 Discussion

In this work, we studied both theoretically and experimentally how the mechanics of cell wall expansion and the molecular processes assembling the cell wall are coordinated during cell morphogenesis, using budding yeast mating projection growth as a model system. We first derived a theoretical description of mating projection growth that couples, through a mechanical feedback encoded in the CWI pathway, the cell wall expansion and geometry to the molecular processes building the cell wall. The theoretical predictions were tested experimentally through genetic deletions affecting the feedback strength and also through mechanical perturbations (hyposmotic shocks and cell wall degradation). Our theoretical predictions are in good agreement with the experimental results and indicate that the existence of mechanical feedback is essential to guarantee stability during cell wall remodeling and cell morphogenesis.

This theoretical description of mating projection growth connects the mechanics of the cell wall to the molecular events in charge of sensing its mechanical state and controlling its assembly via well-established signaling pathways (CWI pathway), thus providing specific predictions on how mutations can affect cell morphogenesis. Various previous models accounted for both the mechanics and assembly (remodeling) of the cell wall [20, 21, 22, 23], as we have done above, but did not account for a connection to known molecular feedback control (CWI pathway) coupling wall mechanics and assembly. These models consider the cell wall to be either a elastic material undergoing remodeling [21, 22] or an elastoplastic material [20], as opposed to our description of the cell wall as a viscous

fluid, which has also been considered before [23]. Importantly, at long timescales over which cell growth and cell wall remodeling occur, assuming the cell wall to be a viscous fluid, a remodeled elastic material or an elastoplastic material is largely equivalent because all of them properly account for the observed irreversible expansion (flow) of the cell wall at long timescales [20]. While previous descriptions assumed that irreversible cell wall expansion only occurs when new cell wall material is inserted into the pre-existing wall [21, 22], we allowed the possibility of cell wall expansion even in the absence of cell wall assembly because the cell wall can be fluidized by the action of wall degrading enzymes secreted via exocytosis. Indeed, addition of zymolyase leads to cell wall piercing for cells with intact cell wall assembly (Fig. 2.5C). Such cell wall degrading enzymes are known to play an important role in cell wall remodeling [87, 59] and the establishment of inhomogeneous cell wall material properties in several organisms [75, 88], including budding yeast [20]. Since these enzymes are secreted via exocytosis, we assumed the length scale of viscosity variation away from the apex to be the same as the exocytosis region. Finally, the combination of the observed inhomogeneous stiffness of the cell wall during mating projection growth [20] (measured at short timescales; seconds) and cell wall remodeling can be theoretically described as an effective inhomogeneous viscosity at timescales longer than cell wall remodeling, as we assumed in our description above and also done previously for other systems [23].

We theoretically find that in the absence of any mechanical feedback relaying information about the mechanical state of the cell wall to the intracellular processes building it,

cell wall expansion is unstable, leading to cell lysis. Previous works have shown that the cell wall is prone to piercing in cell if the CWI is compromised [59], and our experimental data indicates that degradation of the cell wall by zymolyase (effectively lowering the cell wall viscosity in our description) also leads to cell wall piercing (Fig. 2.5C). Since cell wall piercing involves changes in cell wall thickness, our theoretical description accounts for the dynamics of cell wall thickness from first principles (mass conservation). This is in contrast to previous models that also consider cell wall mechanics and assembly, which assume the cell wall thickness to be constant, fixed by an unknown mechanism [20, 21, 22]. Considering a variable cell wall thickness was done before [23], but the cell wall mechanics and assembly were considered independently (no mechanical feedback) and the dynamics of cell growth was not studied. We theoretically show that accounting for the simplest mechanical feedback encoded in the CWI pathway, which directly couples cell wall expansion and assembly via direct activation of Fks1/2 synthases, stabilizes cell wall expansion for a wide range of parameters. The agreement between our theoretical predictions and experimental results suggests that the specific mechanical feedback studied herein, with cell wall stress sensors Wsc1 and Mid2 locally sensing cell wall expansion and directly activating Fks1/2 cell wall synthases, can stabilize cell wall remodeling during mating projection growth by itself. Such mechanical feedback ensures that in regions where the cell wall expands the fastest (at the projection apex) and could potentially rupture via thinning, local activation of cell wall synthases increases assembly of cell wall material, preventing cell wall rupture and stabilizing mating projection growth. However, our work

does not rule out that other mechanical feedbacks encoded in the CWI pathway could also play a role in the stabilization of projection growth. It also is likely that other stress sensors [59, 58], expressed during different cell wall remodeling events in budding yeast, coordinate cell wall expansion and assembly in other morphogenetic processes. While our experimental observations qualitatively agree with our theoretical predictions regarding the existence of an instability associated to the thinning of the cell wall and then need of a mechanical feedback to coordinate cell wall extension and assembly, further experiments will be needed to fully confirm this scenario.

Beyond budding yeast, many other organisms, including other fungi, plants and bacteria, have walled cells that are constantly remodeled [13, 89, 46, 90]. The molecular control of cell wall remodeling and morphogenesis differs across species, and it is therefore likely that different mechanisms encode mechanical feedback in other species. Indeed, previous observations have hinted at the existence of mechanical feedback [91], but the feedback mechanisms remain elusive. The mechanical feedback described herein, or different feedback mechanisms to be discovered, may also play an important role in the coordination of cell polarity and morphogenesis in both animal and walled cells [92, 91, 93, 94].

While essential to ensuring stability during cell wall expansion, our results show that the strength of mechanical feedback does not affect mating projection shape or size (Figs. 2.7 and 2.10). The observed decoupling in the control of cell geometry and growth stability reported here may allow cells to maintain a functional shape under different growth conditions. In addition, we find that projection size is controlled by

the spatial extent of exocytosis. This is in agreement with recent observations in fission yeast indicating that the size of the apical growth domain correlates best with the size of the apical exocytosis region [21], and also with theoretical models of fission yeast that predict the radius of the cell to be determined by the size of the apical cell wall assembly region [22].

More generally, the need to coordinate growth processes and mechanics during morphogenesis is important for individual cells, but also for tissues and organs. Identifying the molecular mechanisms enabling this coordination at different scales and in different organisms will substantially contribute to our understanding of morphogenetic processes.

2.6 Experimental methods

Experiments were done by Carloz Gomez and Dr. Tau-Mu Yi.

Yeast strains and culture conditions

All yeast strains were derivatives of W303-1A and contained the *bar1Δ* mutation that prevents α-factor degradation by deletion of the Bar1 protease. Genetic techniques were performed per standard methods [95]. Yeast strains used in this study are listed in Table A in Appendix A. All strains were cultured in YPD (yeast extract-peptone-dextrose) media supplemented with adenine. The *wsc1Δmid2Δ* strain was grown in YPD media with 1M sorbitol to increase viability. Gene deletions and GFP-tagging were constructed by genomic integration using vectors amplified and targeted by PCR primers [96].

Cell viability measurements

Cell lysis was determined by propidium iodide (Molecular Probes) staining. Propidium iodide (PI) was prepared in DMSO at a concentration of 20 mM and then diluted 1:1000 for use. Propidium iodide was added to cells after being exposed to α-factor (1 μM) for 2 hours. To observe the viability of cells after altering the osmotic pressure, we diluted the YPD media with distilled water upon addition of propidium iodide. The cells were imaged on slides after being exposed to propidium iodide for 10 minutes. Brightfield and fluorescent (RFP filter set) images were acquired using an inverted Nikon Eclipse TE300 microscope with a 60x objective (NA = 1.4). Image analysis was manually performed using ImageJ. Data from 3 samples for each condition was averaged and, for each sample, 150 cells or more were analyzed.

Cell lysis due to zymolyase

To decrease the viscosity of the cell wall, we utilized zymolyase, which contains β-1,3 glucanase, to hydrolyze the glucan linkages that strengthen the wall. Zymolyase (Zymo Research, 1 μl (2 units) per 100 μl of cells) was added to cells exposed to alpha-factor for 1.5 hours. Cells were treated additionally with concanavalin A to immobilize them during the imaging process. The cells were imaged on slides for 7 minutes after being exposed to zymolyase for 3 minutes. DIC images were acquired every 3 seconds. Data from 5 samples for each condition was averaged and, for each sample, 15 cells or more were analyzed. Image analysis was manually performed using ImageJ.

Imaging and analyzing exocytosis

The length-scale of exocytosis was measured in strains that contained Sec3 fused to GFP. Calcofluor White Stain (Sigma-Aldrich) was added to cells 10 minutes prior to imaging (final concentration 0.1mg/ml) to distinguish the cell wall during image analysis. To properly visualize the length-scale and reduce imaging noise, we averaged 30 consecutive confocal images, taken at 2 second time intervals, for each cell, after incubation in 1 μM α-factor for 1 hour and 30 minutes. For *spa2*Δ cells, the 30 images were taken at 13 second intervals to average over a longer time period to average out the stronger fluctuations in polarization in this mutant. Images were acquired with a laser-scanning confocal microscope (Zeiss LSM 710), using a 100x objective (NA = 1.4). The cells were immobilized to a glass-bottom dish coated with concanavalin A. To horizontally orient the mating projections, we layered a YPD (supplemented with 1 μM α-factor) agarose pad on top of the cells. Image analysis was manually performed using ImageJ.

Chapter 3

Maintaining polarization during yeast mating projection growth

3.1 Introduction

Cell polarization is essential to a large number of cellular processes. From cell migration in animal cells to the growth of walled cells from plants and fungi, cells need to spatially polarize to perform key functions. In many cases, an external cue, such as a molecular gradient, triggers the molecular polarization of the cell. Once polarity is established, cells need to maintain polarization at specific spatial locations where cell shape changes or cell movements occur, suggesting the existence of some coordination between these processes. In animal cells, it has been proposed that membrane tension could help such coordination [97, 98], but no specific coordination mechanisms are known. More generally,

it remains unclear what mechanisms provide the molecular polarization machinery with the necessary information about cell geometry and how such polarization machinery coordinates with cell shape changes. This work was done in close collaboration with Dr. Brian Drawert, Dr. Tau-Mu Yi, Professor Linda Petzold and Michael Trogdon who performed the stochastic simulations in Section 3.4. These simulations are discussed in Chapter 5 of Michael Trogdon's dissertation [99].

During polarized (tip) growth in walled cells, from plants to fungi, cells must maintain polarity at the apex as the cell grows. An example of this process is mating projection growth in budding yeast, *Saccharomyces cerevisiae*. During mating, a-cells and α cells secrete pheromones, a factor and α factor, respectively, to attract the opposite cell type. G protein coupled receptors, Ste2, on the cell surface bind pheromone, which triggers a cascade of reactions ultimately leading to the spatial localization of the polarity master regulator, Cdc42. In turn, Cdc42 recruits Bni1, a formin, which initiates the nucleation of actin cables from the polarization site. These actin cables focus transport to the polarization site, bringing enzymes to synthesize and remodel the cell wall as well as more Cdc42. This process induces the localized growth of the mating projection in the direction of maximal pheromone gradient. While cell polarization and subsequent mating projection growth do occur in the presence of pheromone gradients, a graded cue is not necessary. If the distribution of α factor is uniform (no gradient), the molecular polarization machinery has been shown to be able to spontaneously break the symmetry and polarize the cell, albeit in a random spatial direction. Upon polarization, a mating

projection emerges from the polarization cap and this polarization cap is maintained at the tip of the growing projection as it extends. In the absence of a pheromone gradient to externally coordinate spatial and temporal changes in cell polarization and cell shape, the observation of sustained mating projection growth suggests the existence of a cell autonomous coordination mechanism between cell polarity and cell shape. However, no coordination mechanisms are known.

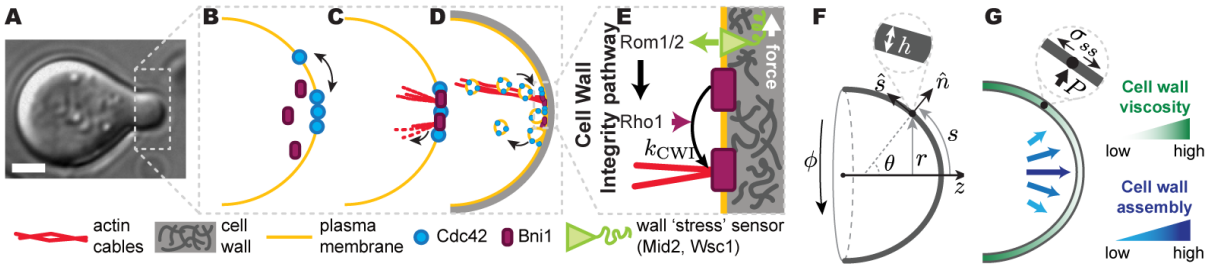

Figure 3.1: **Schematic diagram of relevant events during cell polarization.** A: Transmitted light image of a *S. cerevisiae* cell growing a mating projection in the presence of α-factor. Scale bar, 2μm. B-E: Sketch of molecular events leading to the polarization of the cell during the growth of the mating projection. The key players are indicated in the figure. F: Geometry of the system and definition of the relevant variables. G: Sketch depicting the increasing cell wall viscosity and decreasing cell wall assembly away from the apex. The inset depicts local normal force balance at the cell wall. All variables are defined in the main text.

Many existing models of cell polarization in budding yeast are able to reproduce the spontaneous symmetry breaking and establishment of a polarization cap in a static, spherical cell geometry [25]. However, using 3D simulations of the polarization machinery in non-spherical geometries, we have recently shown that these models cannot explain the maintenance of cell polarization at the tip of mating projections [26]. A polarization cap initially localized at the tip of the mating projection, quickly moves away from the tip and localizes out of the mating projection, thereby precluding mating projection growth.

These simulations contain a feedback between geometry and the polarization machinery: the molecular gradients established inside the cell depend on the cell geometry and these geometry-dependent gradients affect the reaction rates and spatial distribution of polarization molecules at the cell surface. However, this polarization-cell geometry coupling (or feedback) plays against the maintenance of the polarization at the mating projection tip. A different coordination mechanisms between cell shape and polarization must then exist to maintain polarization at the projection tip and sustain mating projection growth.

Cell shape and cell wall mechanics are directly related to each other and, therefore, the mechanics of the cell wall contains information about the cell shape. We have recently shown that the sustained growth of a mating projection requires a mechanical feedback between the cell wall synthesis and cell wall mechanics [48]. This mechanical feedback is genetically encoded through the Cell Wall Integrity (CWI) pathway and involves cell wall "stress" sensors (Wsc1, Wsc2 and Mid2) activating the rho GTPase Rho1, which in turn activates cell wall synthesis (Fks1/2), thereby creating a feedback loop between cell wall mechanics (cell shape) and cell wall assembly. However, Rho1 activation through the CWI pathway also promotes actin cable formation via the local activation of the formin Bni1. Since Cdc42 is transported on actin cables by vesicles, it is possible that the same mechanical feedback shown to stabilize mating projection growth is simultaneously used to maintain cell polarity at the mating projection tip, effectively providing the molecular polarization machinery with the necessary information about cell shape.

Unlike previous theoretical descriptions, which either considered the dynamics of po-

larization in fixed geometries or the mechanics of cell morphogenesis without accounting for polarization, here we couple the dynamics of cell polarization and cell wall mechanics during mating projection growth. Using both a coarse-grained theoretical description and 3D stochastic simulations of the coupled cell polarization dynamics and cell morphogenesis, we show that the mechanical feedback encoded in the CWI pathway coordinates the dynamics of the polarization cap and cell morphogenesis, maintaining the polarization cap at the tip of the mating projection and sustaining mating projection growth.

3.2 Theoretical Description

To study the relation between the dynamics of cell polarization and cell morphogenesis during budding yeast mating projection growth, we employ two different methodologies. First, we describe the mechanics and growth of the cell wall that govern cell shape changes and, in particular, the extension of a mating projection. We then describe for the dynamics of cell polarization using two methodologies: (1) a continuum minimal model for the coupling between polarization and mechanics and, (2) 3D stochastic simulations of the molecular polarization machinery in the growing cell. In both cases, we couple the dynamics of polarization to the mechanics of the cell wall through the CWI pathway and study whether cell polarization can be maintained at the tip of the extending mating projection as well as whether mating projection growth can be sustained by the coupled dynamics.

3.2.1 Geometry and mechanics of cell wall expansion during mating projection growth

As in any walled organism, the budding yeast cell is surrounded by a thin (~ 100 nm [72]) cell wall, much smaller than the characteristic cell size or diameter of the mating projection ($\sim 1\,\mu$m [73]). The shape of the cell is defined by the location of the cell wall and, during mating projection growth, the cell shape can be approximated to be axisymmetric (Fig. 3.1A). The extension of the mating projection can thus be described as the expansion of an axisymmetric thin shell caused by the large cell's internal turgor pressure, P (Fig. 3.1G). It is convenient to parametrize the geometry of the cell (cell wall) by the arclength s from the projection apex and azimuthal angle ϕ (Fig. 3.1F). The shape of the growing projection is characterized by its local radius of curvature, $r(s,t)$, and the two principal curvatures $\kappa_s = \partial\theta/\partial s$ and $\kappa_\phi = \sin\theta/r$, respectively, where $\theta(s,t)$ is the angle between the local outward normal and the axis of growth (Fig. 3.1F). The coordinates (r,ϕ,z) (Fig. 3.1F) are standard cylindrical coordinates, and the angle θ and arclength s provide measures of changes in the normal and tangential directions of the surface, $\hat{n}$ and $\hat{s}$ respectively [23, 74] (Fig. 3.1F).

The description below of the cell wall mechanics and growth is analogous to our prior work [48], which builds up on earlier work combining cell wall mechanics and growth in tip-growing cells [23], as well as on the expansion of thin viscous shells [74]. The dynamics of cell wall expansion during growth are governed by mass and momentum conservation. Since inertia is irrelevant in this system, momentum conservation reduces to local force

balance on the cell wall, which reads

$$\sigma_{\rm ss}\kappa_{\rm s} + \sigma_{\phi\phi}\kappa_{\phi} = P \quad \text{and} \quad \sigma_{\rm ss}\kappa_{\phi} = \frac{P}{2}\,, \tag{3.1}$$

where $\sigma_{\rm ss}(s,t)$ and $\sigma_{\phi\phi}(s,t)$ are the tensions along s and ϕ directions in the wall (Fig. 3.1F). The rheology (mechanical properties) of the cell wall control its expansion in response to the tensions in the wall. While the yeast cell wall in known to behave elastically at short time scales (seconds [72]), plastic behavior manifested by irreversible cell wall expansion occurs on timescales of mating projection growth (minutes [20]). Enzymes that locally degrade the cell wall (glucanases) are brought to the polarization cap by exocytic vesicles moving along the actin cables emanating from it [84]. Upon release to the adjacent cell wall, a higher concentration of glucanases degrade more the cell wall adjacent to the polarization cap, creating a gradient of cell wall degradation away from it. This is consistent with the observation of a higher concentration of cell wall degrading enzymes (glucanases) near the apex of the mating projection [77]. Therefore, at the timescales of growth, the cell wall can thus be approximated by a viscous fluid shell with inhomogeneous viscosity, $\mu(s,t)$, minimal at the polarization cap and increasing away from it (Fig. 3.1F). In this case, the local tangential velocity $u(s,t)$ of a cell wall with constant density $\rho_{\rm w}$, or equivalently, its strain (expansion) rates $\dot{\epsilon}_{\rm s} = \partial u/\partial s$ and $\dot{\epsilon}_{\phi} = (1/r)(dr/dt)$ are related to the tensions in the wall by [23, 74]

$$\sigma_{\rm ss} = 4\,\mu(s,t)\,h\,[\dot{\epsilon}_{\rm s} + \dot{\epsilon}_{\phi}/2] \quad \text{and} \quad \sigma_{\phi\phi} = 4\,\mu(s,t)\,h\,[\dot{\epsilon}_{\rm s}/2 + \dot{\epsilon}_{\phi}]\,. \tag{3.2}$$

Beyond the expansion of the cell wall in response of the tensions in it, new cell wall

needs to be assembled as the mating projection grows. The cell wall is assembled via Fks1/2 synthases at the plasma membrane that extrude $1,3-\beta$ glucans to the preexisting wall. Since Fks1/2 synthases are also brought to the plasma membrane along actin cables and inserted in it during the exocytosis process, their concentration is high at the polarization cap and decreases away from it, generating a graded distribution $G(s,t)$ of the cell wall assembly rate that decreases away from the polarization cap. In this case, mass conservation of the cell wall material during mating projection growth reads

$$\partial_t(rh) + \partial_s(rhu) = \frac{r\mathrm{G}(s,t)}{\rho_\mathrm{w}}\,, \tag{3.3}$$

where $h(s,t)$ is the cell wall thickness (Fig. 3.1E) and ρ_w is the cell wall density (assumed constant).

The functions $\mu(s,t)$ and $\mathrm{G}(s,t)$ depend directly on transport along actin cables and exocytosis, which are controlled by the polarization machinery. We will relate these functions to the dynamics of polarization below.

3.2.2 Dynamics of cell polarization: minimal coarse-grained model

In order to form a mating projection, the cell must first polarize to specify the site of cell wall growth and expansion. Many molecular players are involved in the cell polarization process in response to mating pheromones. In our 3D stochastic simulations (see below), we will consider the coupled dynamics of many of the key molecular players in the polarization process. However, since the aim of this coarse-grained model is to

study solely the coupling between the dynamics of polarization and the mechanics of cell wall expansion during mating projection growth, we neglect much of the complexity of the polarization molecular machinery. Since the formin Bni is directly activated through the CWI pathway, leading to the assembly of actin cables and further recruitment of the master polarity regulator Cdc42 via actin-mediated transport, we consider solely the effective coupled dynamics of Cdc42 and Bni on the curved geometry of the cell.

Inactive Cdc42 can reach the plasma membrane either through direct binding from a cytoplasmic pool [100, 101] or through actin cable-mediated transport, carried by secretory vesicles [101]. Once at the membrane, Cdc42 diffuses (diffusion constant D $\mu\text{m}^2/s$) and also unbinds from the membrane at a rate k_D. Once activated [100], the Cdc42 population at the plasma membrane acts as a central regular of many polarization factors. In particular, it recruits Bni1, a formin that drives the nucleation of actin cables [102] (Fig. 3.1)C. As mentioned above, these actin cable bring many different factors that are essential for cell wall remodeling and growth, as well ad Cdc42 itself, creating a positive feedback loop. Focusing on this feedback between Cdc42 and Bni1, we can write the dynamics of Cdc42 on the plasma membrane of the mating projection as

$$\partial_t(r\rho_{\text{C}}) - D\partial_s(r\partial_s\rho_{\text{C}}) = r\left[k_X\rho_{\text{A}} - k_D\rho_{\text{C}}\right] , \tag{3.4}$$

where ρ_C is the Cdc42 concentration on the plasma membrane, k_X is the rate at which Cdc42 is added to the plasma membrane through transport along actin filaments, which are characterized by a local surface density ρ_{A}. Since actin cables are nucleated by active Bni, we assume the local density of actin cables emanating from the membrane

to be proportional to the local active Bni1 concentration, $\rho_{\mathrm{B,a}}$, at the plasma membrane, namely $\rho_{\mathrm{A}} \sim \rho_{\mathrm{B,a}}$. For simplicity, we assume a uniform pool of inactive Bni1 on the plasma membrane with concentration $\rho_{\mathrm{B,i}} = \rho_0$ and write the dynamics of active Bni1 as

$$\partial_t(r\rho_{\mathrm{B,a}}) = r\left[k_{\mathrm{R}}\rho_{\mathrm{C}} + k_{\mathrm{CWI}}\rho_0 - k_{\mathrm{I}}\rho_{\mathrm{B,a}}\right] , \tag{3.5}$$

where k_R is the rate at with Cdc42 recruits (and activates) Bni1, k_{I} is the inactivation rate of Bni1 and k_{CWI} is rate of activation of Bni1 through the CWI pathway (independently of Cdc42) [103]. Activation of the CWI pathway depends on the local mechanical state of the cell wall, leading to a direct coupling between the dynamics of Bni1 and the mechanics of the cell wall. Since CWI activation correlates with locations of cell wall expansion, we write the local activation rate of Bni1 via the CWI as being proportional to the local cell wall expansion (strain) rates [48], namely

$$k_{\mathrm{CWI}} = A_{\mathrm{CWI}}[\dot{\epsilon}_s + \dot{\epsilon}_\phi] , \tag{3.6}$$

where A_{CWI} is a dimensionless constant that measures the strength of the mechanical feedback.

In order to fully connect the dynamics of Cdc42 and Bni1 to the mechanics of cell wall expansion during morphogenesis, it is necessary to relate the cell wall viscosity $\mu(s,t)$ and the rate of new cell wall assembly $G(s,t)$ to polarity. Since cell wall synthases Fks1/2 are carried to the plasma membrane through secretory vesicles along actin cables, we write the rate of new cell wall assembly $G(s,t)$ to be proportional to the local concentration of actin cables, namely $G(s,t) = k_s\,\rho_{\mathrm{A}}$, with k_s being the Fks1/2 rate of new wall assembly. Similarly, the spatial variations in the cell wall viscosity reflect spatial changes

in the concentration of glucanases, which are transported to the cell surface through actin cables. Consequently, we assume the length scale of viscosity variations in the cell wall to be determined by spatial variations in actin cable density, namely $\mu(s,t) = \mu_0 \exp(s^2/\lambda_{\mathrm{A}}^2)$, where λ_{A} is the length scale of the decay in actin cable density from the tip of the mating projection. This indicates that in regions with high concentration of actin cables, the cell wall viscosity is lower, enabling cell wall expansion in that region.

Dimensionless parameters				
$\frac{P(D/k_D)^{1/2}\rho_w}{12\mu_0 k_s \rho_0}$	A_{CWI}	k_{I}/k_D	k_{R}/k_D	k_X/k_D
Physical/Chemical parameters				
Parameter	Description	Parameter	Description	
P	Turgor pressure of budding yeast	k_{D}	Apical rate of endocytosis	
ρ_w	Cell wall density	k_{X}	Apical rate of exocytosis	
μ_0	Apical viscosity of cell wall	k_{R}	Recruitment rate of Bni1 by Cdc42	
k_{s}	Rate of new wall synthesis	k_{I}	Inactivation rate of Bni1	
ρ_0	Membrane concentration of Bni1	D	Membrane diffusion constant of Cdc42	

Table 3.1: System physical parameters and relevant dimensionless parameters

Combining equations 3.1-3.5 and viscosity profile described above, we solved the coupled dynamics of polarity and cell wall expansion during cell morphogenesis. Scaling length and time with $(D/k_D)^{1/2}$ and k_D, respectively, the stresses with P and the surface densities of Cdc42 and active Bni1 with ρ_0, we obtain the relevant dimensionless parameters in the system, as described in Table 3.2.2. The parameters k_{I}/k_D,k_{R}/k_D, k_X/k_D have either been measured or estimated and we use their known values (Table 3.2.2). In contrast, the feedback strength A_{CWI} has not been directly measured. To explore the

role of a potential mechanical feedback between cell wall mechanics and polarization, we study the dynamics of the system upon changes in the feedback strength A_{CWI}.

3.3 Mechanical feedback can maintain cell polarization at mating projection tip

This minimal coarse-grained model focuses only on a possible feedback loop between cell wall mechanics and cell polarization that could maintain cell polarization at certain regions of the cell surface upon cell growth. Because of the minimal nature of this description, we do not account for several molecular interactions that are responsible for the initial spontaneous symmetry breaking in the spherical cell. We therefore start from the geometry of a mating projection and study the dynamics of polarization in the elongated shape of the growing projection.

In the absence of mechanical feedback ($A_{\mathrm{CWI}} = 0$), an initially polarized cell loses its polarization within the typical timescales of the dynamics of the cell polarization machinery, as can be seen from the loss in polarization in Cdc42 (Fig. 3.1a). Since the typical timescales of the molecular processes associated with polarization are shorter than the timescales of physical mating projection growth, cell polarization is lost before any cell shape changes occur. In contrast, if the strength of the mechanical feedback is large enough, cells maintain cell polarization at the tip of the growing mating projection. Even starting from a uniform distribution of Cdc42 in the mating projection (not polarized),

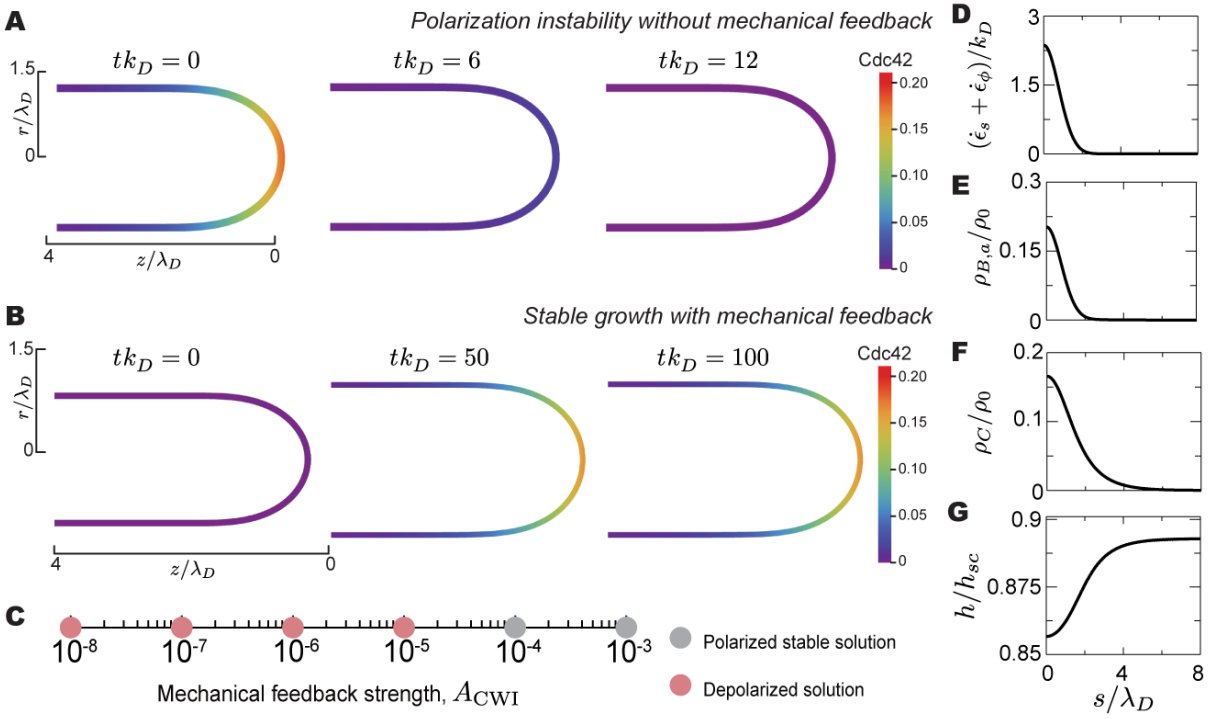

Figure 3.2: **Maintenance of cell polarization at the mating projection tip via mechanical feedback** A: Simulation of an initially polarized cell depolarizing without mechanical feedback even at the short timescales of the molecular dynamics B: Cell becomes polarized and grows stably with mechanical feedback over timescales of growth. C: Phase diagram showing the state of the cell (polarized or not) as a function of the mechanical feedback strength Steady state spatial profiles for D: cell wall expansion rate $\dot{\epsilon}_s + \dot{\epsilon}_\phi$ E: Bni1 density F: Cdc42 density G: cell wall thickness h.

the mere presence of the mechanical feedback polarizes the cell at the tip of the mating projection, enabling the sustained growth of the projection and the maintenance of polarization at the tip during growth (Fig. 3.1b). In between these two limiting regimes, there is a critical value of the mechanical feedback strength below which the cell is unable to maintain cell polarization (Fig. 3.1c), eventually leading to a uniform and very low (vanishing) concentration of Cdc42 at the plasma membrane. Above the critical value, stable solutions for the polarized state exist and the cell can maintain cell polarization at the tip of the mating projection during growth (Fig. 3.1b).

As expected for the tip growth of the mating projection, the stable solutions show that the rate of cell surface (cell wall) expansion, namely $\dot{\epsilon}_s + \dot{\epsilon}_\phi$, is maximal at the tip and decays away from it over a characteristic lengthscale of the polarity machinery, λ_D, to eventually vanish in the region where the cell wall becomes solid-like (Fig. 3.1d). The presence of mechanical feedback (with cell wall expansion activating Bni1 through the CWI pathway), leads to the localized activation of Bni1 at the tip (Fig. 3.1e) that, in turn, generates a localized (polarized) density of actin cables emanating from the tip of the growing mating projection. This higher density of actin cables at the tip generates higher concentrations of Cdc42 in this region (Fig. 3.1f), maintaining cell polarization during cell growth. Finally, the cell wall thickness is largely uniform along the mating projection, albeit with a slight thinning at the tip.

This minimal description, which couples the mechanics and growth of the cell wall with the polarization dynamics, shows that the mechanical feedback between cell wall expansion and Bni1 dynamics encoded in the CWI pathway can maintain cell polarization at regions of the cell surface where cell wall expansion occurs. Since cell wall expansion and cell geometry are related to each other through mass and momentum conservation, this mechanical feedback effectively provides the cell polarization machinery with information on the cell shape.

3.4 Combined mechanical description with stochastic simulations of cell polarization

The mechanics description inputs profiles of the concentration of actin and Cdc42, so here we obtain them from stochastic simulations. Because the timescales of cell wall expansion and growth (cell shape changes) are much longer than the timescales of the molecular reactions involved in cell polarization, we perform stochastic simulations of molecular polarization models while updating the shape of the cell using our mechanical model. The stochastic simulations were performed by Michael Trogdon.

To perform 3D stochastic simulations of the polarization dynamics in this geometry, we employ the PyURDME software [104], which can simulate spatial stochastic dynamics on complex, 3D and time-dependent geometries. In this stochastic model, we consider both the inactive (Cdc42-GDP) and active (Cdc42-GTP) states of Cdc42, the local density of actin cables on the membrane and actin monomers in the cytoplasm (Fig. 3.2A). Inactive Cdc42 in the cytoplasm can directly bind to the membrane at a rate $0.28\mu m s^{-1}$ [105] and has a membrane diffusion constant of $0.0053\mu m^2 s^{-1}$ [106]. It can also dissociate from the plasma membrane at a rate $1s^{-1}$[105]. At the plasma membrane, inactive Cdc42 can be activated and inactivated at rates $0.266\mu m^3 s^{-1}$ [105] and $1s^{-1}$[105], respectively. Local assembly of actin cables on the membrane is due to Bni1 activation, which can be caused either by active Cdc42 at a rate $0.197\mu m^3 s^{-1}$ [106] or by Rho1 through the CWI pathway at a rate that depends on the local cell wall expansion, namely $A_{\mathrm{CWI}}[\dot{\epsilon}_s + \dot{\epsilon}_\phi]$.

Actin filaments disassemble at a rate $1.57s^{-1}$ [106]. For a complete set of equations describing this model, please see section 3.6.

We coupled the 3D stochastic simulations of cell polarization to the mechanics of the expanding cell wall. This involves performing the 3D stochastic simulations of the polarization machinery in a changing cell shape, governed by the mechanics of cell wall expansion described above (Eqs. 3.1-3.3). To do so, we used an operator splitting methodology similar to that described in our previous work [107], where the simulation can evolve over time in a predetermined manner. Here we use the equations describing the mechanics of the cell wall expansion during mating projection growth (Eqs. 3.1-3.3) to dictate how the simulation domain (cell shape) evolves over time. The operator splitting methodology takes advantage of the large separation of timescales between the fast molecular processes that polarize the cell and slow physical cell wall expansion during cell growth.

Staring with a spherical geometry (sphere of radius $r = 2\mu m$) and random initial distribution for each species (Fig. 3.3A), we simulate the polarization dynamics for timescales smaller than any relevant change in cell shape. The cell polarization machinery establishes a polarization cap within the spherical geometry, as observed experimentally and recapitulated by many polarization models. This spontaneous symmetry breaking reduces the symmetry of the problem from a sphere to a axisymmetric geometry. Taking advantage of the axisymmetric geometry, we time and rotationally averaged the concentration of active Cdc42 and actin cables to obtain their distributions along the arclength s from the tip of the mating projection. Once these averaged distributions are known,

they can be used as input fields for the equations describing the mechanics of cell wall expansion. As described above for the coarse-grained model, we write the rate of new cell wall assembly $G(s,t)$ to be proportional to the local concentration of actin cables, namely $G(s,t) = k_s\,\rho_{\rm A}$, and the cell wall viscosity $\mu(s,t) = \mu_0 \exp(s^2/\lambda_{\rm A}^2)$, with $\lambda_{\rm A}$ being the length scale of the decay in actin cable density from the tip of the mating projection. In this specific simulations, the spatial profile of actin cable density $\rho_{\rm A}(s)$ and $\lambda_{\rm A}$ correspond to the averaged distributions described above. Knowing $G(s)$ and $\mu(s)$ from the averaged actin cable density profile, we integrate the Eqs. 3.1-3.3 describing cell wall expansion from the initial spherical geometry and for the same time period. Cell wall expansion during the integration time leads to a small change in cell shape. We then continue the 3D stochastic simulations of polarization in this new cell geometry, leading to small changes in the spatial profile of Cdc42 and actin cables. The new averaged spatial profile of actin cable density is then used to obtain the new $G(s)$ and $\mu(s)$ and we solve again the mechanics of cell wall expansion. Iteration of this process allows us to simulate the couple (stochastic) dynamics of polarization in the evolving cell shape.

To understand whether the mechanical feedback encoded in the CWI pathway could also stabilize the polarization cap during mating projection growth, we simulated their coupled dynamics as described above. We found the polarization cap is maintained stable at the tip of the mating projection during growth (Fig. 3.3A,B). Both the Cdc42 and actin cables profiles are polarized at the tip, displaying a higher concentration in this region and decaying away from it. In the absence of mechanical feedback, no mating

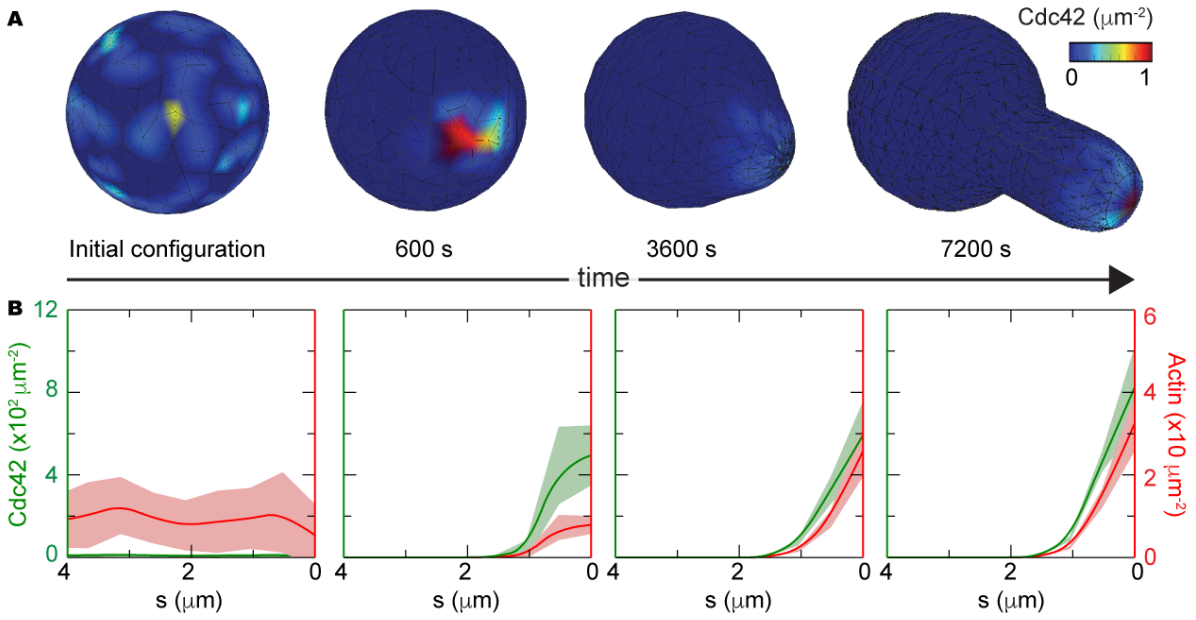

Figure 3.3: **Coupled dynamics of cell polarization and cell wall expansion during mating projection growth in the presence of mechanical feedback.** Starting from a uniform density of Cdc42 in a spherical geometry, the cell polarizes and grows a mating projection. A: A 3D realization showing a uniform density of cdc42 at t=0s transiting to a polarized state with the cdc42 cap co-localized to the tip of the mating projection B: 2D profiles of Cdc42 and actin becoming polarized over time.

projection grows from the initial spherical cell because it is not possible to maintain the polarization cap stably located at the point where the mating projection starts to form.

3.5 Discussion

Here we theoretically explored how a mechanical feedback between the mechanics of cell wall expansion and the dynamics of the polarization machinery can stabilize and maintain cell polarization at the tip of a growing mating projection. Using both a coarse-grained description and full 3D stochastic simulations of polarization, our results show that a mechanical feedback encoded in the CWI pathway, which activates the formin

Bni1 formation through mechanical input from the cell wall, is sufficient to maintain the polarization cap at the tip of a growing mating projection.

We first derived a minimal coarse grained theoretical description of the dynamics of the key polarity molecules Cdc42 and Bni1 and coupled it to the mechanical state of the wall via the CWI pathway. We showed that mechanical feedback was able to maintain the localization of the polarization cap to the tip of the mating projection. We then coupled the equations describing the mechanics of the cell wall to a 3D stochastic model of polarization. Despite the increased complexity of the stochastic simulations, the 3D system also required mechanical feedback to maintain the polar cap at the tip of the mating projection. The reaction diffusion equations were solved in 3D space, which resulted in additional complexities. The output of the stochastic models of course depend on the initial concentration and locations of the molecules.

Previous models of polarization [24, 108, 109, 110, 111] did not account for non-spherical geometries. As the cell grows a mating projection, the shape of the cell changes and thus the cell must coordinate the location of the polar cap to the site of growth. Modeling the system with just Cdc42 does lead to the development of polar caps but with no specific preference for location as seen in Fig 3.4A [108]. Further modeling has shown that actin may be necessary to ensure that the cap does not wander [111]. However these results have been obtained in a spherical geometry. Experimentally, it has been shown that the formation of constitutionally active Cdc42 clusters in a cell with a mating projection does not occur at the tip [108]. It was further shown that the

disruption of actin and components of the exocyst complex was necessary for the temporal maintenance of the polar cap. However the question of the spatial maintenance of the polar cap during mating projection growth has still not been experimentally tested. In the cell with a mating projection, there must be a mechanism which provides a preference for the polarization site. The cell wall integrity pathway sensing the location of expansion and providing a feedback to recruit more actin cables and polarity machinery to the site of growth seems to be a plausible mechanism for also ensuring the spatial maintenance of the polar cap.

Beyond budding yeast, many other organisms, including other fungi, plants and bacteria, undergo polarized cell wall growth [13, 112, 113, 114]. The molecular control of cell wall remodeling and morphogenesis differs across species, and it is therefore possible and even likely that different mechanisms encode mechanical feedback in other species. Fission yeast exhibits polarized growth and it has been recently shown that stable polar caps are destabilized by the arrest of growth [115]. This effect is akin to the removal of the mechanical feedback. Previous work [116] by the same group showed that a there exists a cell wall integrity pathway in fission yeast, similar to our results in Chapter 2, that coordinates wall growth. Likely similar to our findings, the same feedback mechanism ensures the maintenance or lack thereof seen in their experimental results [115]. The mechanical feedback described herein, or different feedback mechanisms yet to be discovered, may also play an important role in the coordination of cell polarity and morphogenesis in both animal and walled cells [117, 118, 119, 98].

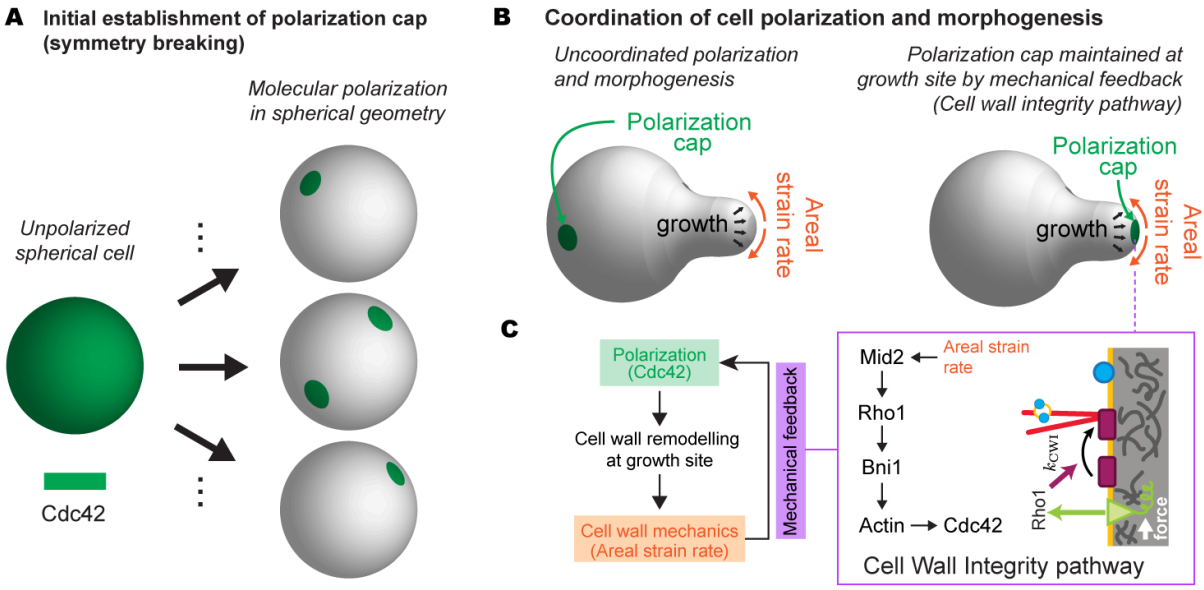

Figure 3.4: **Schematic summary of the process of polarization.** A: Unpolarized budding yeast cells can spontaneously break the symmetry and establish a polarization cap that is randomly located on the cell's surface (all locations on the cell surface are equally probable) or even create multiple polarization caps. B: The polarization cap need not be maintained at the tip of the mating projection and this has been seen experimentally [108]. However the site of polarization must be localized to the site of growth C: The polarization cap can gain information about the geometry and site of growth through the cell wall integrity pathway which provides a feedback between the cell wall mechanics and polarization machinery of Bni1.

Polarization is a critical component for cell migration, growth, division, and signal propagation. The mechanisms by which cells remain polarized while changing shape due to migration and growth are not well understood. Results from this work and our previous work [48] show that the same mechanical feedback mechanism is used in seemingly different contexts to inform the molecular machinery of the physical state of the cell here for sustaining polarization and ensuring cell wall stability. More generally, the need to coordinate molecular processes with cell shape changes and growth is a general problem beyond polarization. Identifying the molecular mechanisms enabling this

coordination at different scales and in different organisms will substantially contribute to our understanding of morphogenetic processes.

3.6 Computational methods

Numerical integration of coarse grained equations

The system of equations was scaled and written in a manner such that r, h, ρ_{cdc42}, and ρ_{actin} were described by equations evolving in time, and u, θ, κ_{s} by differential equations in s. The latter equations were solved by the method of lines; s was discretized and the s-derivatives were written as a differential matrix using fourth order central difference and one sided finite differences at the boundary. The resulting system becomes a differential algebraic system (DAE), which was solved using Sundials [120], a suite of nonlinear and DAE solvers. Steady state solutions were obtained by ensuring that all time derivatives of scaled variables were below 10^{-3}.

Numerical integration of coupled reaction diffusion simulations

The stochastic simulations were solved by Michael Trogdon. The mechanics equations were coupled to the reaction diffusion equations. This was done assuming a separation of timescales of the physical growth governed by the mechanics equations and the biochemical reactions governed by the stochastic reaction diffusion equations. The mechanics equations were solved using the same method presented above for the integration

of the coarse grained equations. The stochastic reaction diffusion equations were built and solved using PyURDME and MOLNs. Computational meshes for each geometry consisted of a discretization of both the cytoplasm and the membrane (the surface of the shape), allowing for diffusion both in the cytoplasm and on the membrane as required by the models used in this study. All reactions took place in voxels on the membrane for each geometry. These meshes were generated using Gmsh.

Model 1: Reactions for the coarse grained model of Cdc42 and actin polarization presented in Figure 3.3.

$$Cdc42GDP_c \xrightarrow{\beta_2} Cdc42GDP_m$$

$$Cdc42GDP_m \xrightarrow{\beta_3} Cdc42GDP_c$$

$$Cdc42GDP_c + Actin_m \xrightarrow{\beta_1} Cdc42GTP_m + Actin_m$$

$$Cdc42GDP_m + Actin_m \xrightarrow{\beta_1} Cdc42GTP_m + Actin_m$$

$$Cdc42GTP_m \xrightarrow{\alpha_3} Cdc42GDP_m$$

$$Actin_c + Cdc42GTP_m \xrightarrow{A_{on}} Actin_m + Cdc42GTP_m$$

$$Actin_c \xrightarrow{S\dot{\epsilon}} Actin_m$$

$$Actin_m \xrightarrow{A_{off}} Actin_c$$

Chapter 4

Zebrafish body axis elongation

4.1 Introduction

During embryonic development, tissues undergo major physical transformations to build functional structures. As for inert materials, shaping embryonic tissues necessarily involves the spatiotemporal control of several key physical quantities [3], namely its growth (e.g., cell proliferation), material properties and/or active stresses. Unlike inert systems, however, living tissues are active materials and can locally regulate the value of these fields through local changes in cell behavior. However, it is unclear what physical fields are spatiotemporally controlled to sculpt tissues and organs and their specific roles in morphogenesis, mainly because measurements of spatiotemporal variations in these physical quantities within developing embryos are still sparse. Since spatiotemporal variations in multiple physical fields can contribute to the morphogenetic processes [3], it is important to have information of all these fields in the same system to establish how the tissues are

physically shaped. This work was done in close collaboration with Dr. Payam Rowghanian, Emmet Carn, Dr. Georgina Stooke-Vaughan, who performed the experiments in Section 4.5, and Dr. Sangwoo Kim who performed the data analysis.

Recently, quantitative measurements of the spatial variations in both mechanical stresses and tissue material properties showed that a fluid-to-solid transition in the state of the tissue guides the posterior extension of the body axis in zebrafish embryos [28] (Fig. 4.1a). During zebrafish posterior body elongation, cells in dorsal-medial (DM) posterior tissues continuously move ventrally to the mesodermal progenitor zone (MPZ), providing the necessary material to build the body axis since, at the developmental stages studied in those experiments, cell proliferation is negligible and does not substantially contribute to the elongation of the body axis [121, 122].

The mesodermal progenitor cells in the MPZ progressively incorporate into the presomitic mesoderm (PSM), a process that involves their maturation into mesodermal cells and their gradual arrest [28, 123, 124, 39]. The observed fluid-to-solid transition was found to be associated with cellular jamming along the anteroposterior (AP) axis following an anterior decrease in extracellular spaces and in cell-cell contact active fluctuations [28]. Regardless of the specific physical mechanism of this transition, the tissue was found to transit from a fluid-like state in the posterior end of the body, namely the MPZ, to a solid-like state in the PSM (Fig. 4.1a-b). Continuum mechanics simulations showed that the existence of a fluid-to-solid transition in the tissue was sufficient to reproduce body axis elongation [28], but it remains unclear what tissue shapes (morphological

phenotypes) can be achieved with the observed transition, how different physical parameters control the temporal evolution of tissue shape, and how different physical quantities (stress, tissue pressure, velocity, etc.) vary spatially during body axis elongation.

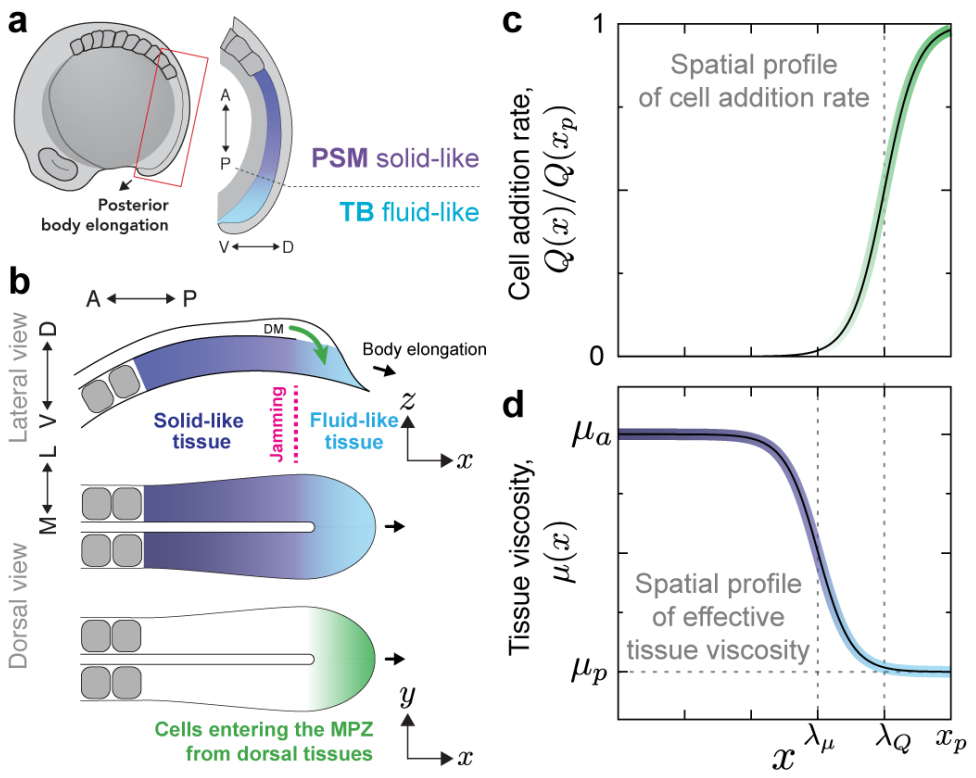

Figure 4.1: a) Schematic view of the zebrafish embryo at 10-somite stage. Cells moving along the anterior-posterior axis in the DM tissue enter the ventral tissue at the posterior end, drive growth, and move anteriorly as they enter a more solid-like tissue. b) Spatial profile of cell addition rate to the posterior end as a function of the distance from the posterior end of the tissue. c) Spatial profile of tissue viscosity as a function of the distance from the posterior end of the tissue.

Several methods exist to simulate tissue morphogenesis. Cell-based models are well suited when cellular resolution is necessary, but typically lead to a large number of parameters because the mechanical state for each cell needs to be accounted for [29, 30, 31, 32, 33, 34]. The tissue material properties and stresses in cell-based models emerge

from the collective behavior of cells, and the connection between mechanical parameters at the cell scale and material properties at the tissue scale can be quite complex. While cell-based approaches are necessary for small cell numbers or in theoretical descriptions requiring cellular resolution, when studying tissue morphogenesis at length and time scales characteristic of tissue dynamics (typically larger than those of cell dynamics), tissue morphogenesis can be properly described by coarse-grained continuum approaches that only require information of physical fields at supracellular scales [35]. Previous continuum descriptions of tissue morphogenesis generally assumed spatially uniform mechanical properties (i.e., constant tissue viscosity or constant stiffness depending on the tissue) and considered only spatial variations in either cell proliferation or forces because experimental studies have been mostly focused on spatial variations of these quantities [125, 126, 127]. The role of spatial variations in tissue mechanical properties and, especially, the role of regional changes in fluid and solid tissue states has been largely unexplored.

In the specific case of body axis elongation, self-propelled particle descriptions have been to understand cellular movements in the tissue. These simulations assumed set tissue shape (fixed tissue boundaries), allowing the prediction of cell movements but not tissue morphogenesis since the boundaries are, by construction, fixed. Importantly, most cases of tissue morphogenesis are examples of so-called free boundary problems, in which tissue flows change the shape of the tissue and these boundary changes affect the movements inside the tissue. Therefore, in tissues that change shape during morphogenesis,

it is important to consider the coupled dynamics of the tissue shape and morphogenetic flows.

Building on previous work [28], we theoretically explore the role of the tissue fluid-to-solid transition on the elongation of the zebrafish body axis. We treat the system as a free-boundary problem and perform 2D finite element numerical simulations of tissue morphogenesis based solely on first principles (mass and momentum conservation) to study how the characteristics of a spatially-restricted fluid-to-solid transition between tissue states affect morphogenetic flows, tissue stresses and their morphological outcome. Our results show that the mere presence of a fluid-to-solid transition along the AP axis enables unidirectional tissue elongation. In the absence of the fluid-to-solid transition, the tissue either expands isotropically when the tissue surface tension is not negligible. In the presence of a fluid-to-solid transition, our results show that morphogenetic flows can either smoothly transit from posterior-directed movements in the MPZ to anterior-directed tissue flow in the PSM or alternatively display counter-rotating vortices as the tissue transits from fluid-like to solid-like states. The predicted AP axial stresses indicate that the MPZ tissues are pushed posteriorly, contributing to axis elongation, whereas PSM tissues are pushed anteriorly, indicating that the PSM mechanically sustains the extension of the body. In between, both posteriorly-directed and anteriorly-directed AP stresses are found at the same distance from the extending body end, depending on the distance from the embryo midline. Finally, for large enough tissue pressures preventing cells from DM tissue to enter the MPZ, our simulations predict the arrest of

body elongation.

4.2 Theoretical description

Since we are interested in tissue morphogenesis at supracellular length scales and developmental time scales, we describe the tissue as a coarse-grained continuum. Indeed, all observed mechanical gradients in the tissue during body axis elongation occur at length scales much larger than the cell size and are persistent over timescales longer that characteristic timescales of cellular processes [28], indicating that a coarse-grained description is apt, as previously emphasized in other systems [128, 129]. Moreover, since the ventral tissue (including MPZ and PSM) is thin along the dorsal-ventral axis (DV, z axis) compared to its medial-lateral (ML, y axis) and anterior-posterior (AP, x axis) extensions [28, 124] (Fig. 4.1a-b), we approximate the tissue as a 2D system, neglecting the DV tissue thickness, and simulate a 2D DV projection of the ventral tissues (Fig. 4.1b). Finally, since the notochord has little ML extension and the extension of the body axis has been shown to proceed in the absence of notochord [130], we neglect it here.

In order to sustain the continuous posterior extension of the body axis, it is necessary to constantly add new material at the posterior end of the ventral tissues. Cell proliferation could potentially contribute to the addition of new tissue material, but it has been previously shown that proliferation is minimal in the tissue and that its inhibition does not preclude the formation of the body axis [122, 131], indicating that cell proliferation is not driving tissue elongation in zebrafish at these developmental stages [121]. From the

perspective of ventral tissues, the dorsal to ventral movement (ingression) of cells at the posterior end of the tissue represents an addition of material to the MPZ region as body elongation proceeds (Fig. 4.1b). However, cell ingression into the MPZ can only occur if enough space can be made available for the ingressing cells, which depends directly on the local tissue pressure (local volume changes are directly related to the local value of the pressure): large tissue pressure in the MPZ will prevent ingression of cells from DM tissues because these cannot generate enough force to push their way into the MPZ. Since the ingression of cells to the MPZ from DM tissues has been shown to be restricted to a region of limited size at the extending posterior leading edge of the tissue [39], we define the rate of cell ingression from DM tissues into the MPZ, $Q(x,p)$, with both explicit spatial and pressure dependencies, namely

$$Q(x,P) = \frac{Q_0\left(1-\frac{P}{P_{\rm C}}\right)\Theta\left(1-\frac{P}{P_{\rm C}}\right)}{1+\exp\left(\dfrac{x_{\rm P}-\lambda_Q-x}{a}\right)}\,, \tag{4.1}$$

where P is the tissue pressure, P_C is the critical pressure over which cells cannot ingress into the MPZ and Q_0 is the maximal cell addition rate at the posterior-most end of the body axis when tissue pressure is negligible. The function $\Theta(\bullet)$ represents the Heaviside step function and $x_{\rm p}$ is the time-dependent position of the end of the body axis. In the case that tissue pressure is small compared to p_c, the cell addition rate $Q(x,P)$ decays along the AP axis from a maximal value Q_0 at the posterior-most end to vanishing values at length scales larger than λ_Q, which sets the size of the ingression region (Fig. 4.1b,c). In this case, Q transits from Q_0 to zero over a spatial range of size a (with $a \ll \lambda_Q$). If

the tissue pressure is not negligible compared to p_c, cell ingression will be limited further following to the spatial profile of the tissue pressure, and eventually halted for tissue pressures above p_c. From the reference frame of the extending posterior end, the profile Q does not change over time at steady-state, but in the absolute reference frame it does so through its dependence on the position $x_{\mathrm{p}}(t)$ of the extending body end.

In order to simulate the physical growth of the tissue, it is necessary to know its material properties and the way they change in space and time. As explained above, direct measurements of tissue mechanics have revealed that ventral tissues undergo a fluid-to-solid transition along the AP axis, with the fluid-like MPZ tissues rigidifying into to a solid-like PSM [28]. The transition was found to be caused by cellular jamming as cells mature and transit from the MPZ to the PSM. Within the broad classification of jamming transitions [132], the observed transition corresponds more closely to a glass transition, as the active cell-scale forces were shown to generate cell-cell contact fluctuations that can be qualitatively thought of as an effective temperature. The observed larger effective temperature (higher cell-cell contact fluctuations) of the MPZ was found to be the main cause of fluidization of this posterior tissue region, with the PSM tissues rigidifying mainly due to the anterior decrease in effective temperature (lower cell-cell contact fluctuations). In glass transitions, the relaxation timescale of the system becomes arbitrarily large as the system in cooled below the glass transition temperature, leading to arbitrarily large viscosities as the temperature is progressively lowered [32]. The fluid-like state of the extending posterior MPZ tissue can be thought of as the tissue

having an effective temperature higher than the glass transition temperature, enabling cellular rearrangements and tissue fluidization. In contrast, the solid-like PSM can be thought of as a tissue with an effective temperature lower than the glass transition temperature, leading to very large viscosities that barely allow any tissue reorganization at the observation timescales, effectively rigidifying the PSM. To account for a fluid-to-solid transition of this nature along the AP axis, we describe the tissue as a viscous fluid with inhomogeneous viscosity $\mu(x)$, minimal at the posterior end of the body and sharply transiting to a very high viscosity value at a defined distance λ_μ from the posterior end of the body (Fig. 4.1b,d), namely

$$\mu(x) = \mu_p + \frac{\mu_a - \mu_p}{1 + \exp\left(\dfrac{x - (x_\mathrm{P} - \lambda_\mu)}{a}\right)}\,, \tag{4.2}$$

where μ_p and μ_a are the values of the tissue viscosity in the MPZ and PSM, respectively. The transition between low and high tissue viscosities occurs over a region of size a (with $a \ll \lambda_\mu$). Large values of μ_a/μ_p ($\mu_a/\mu_p \to \infty$) simulate the observed fluid-to-solid tissue transition, but it is also possible to simulate a tissue with uniform viscosity ($\mu_p = \mu_a$) and intermediate behaviors.

Knowing the spatial distribution cell ingression rate and tissue viscosity along the AP axis, which we consider here as input fields, it is possible to simulate the dynamics of tissue morphogenesis. Two fundamental equations govern the dynamics of the system, namely mass conservation (or mass balance) and momentum conservation. In the presence of spatially-dependent cell ingression, $\mathrm{Q}(x, P)$, mass conservation reads

$$\frac{\partial \rho}{\partial t} + \nabla \cdot (\rho \mathbf{u}) = \mathrm{Q}(x, P)\,, \tag{4.3}$$

where $\mathbf{u}$ and ρ are the velocity and density fields, respectively. Since the cell density has been experimentally shown to be uniform along the AP axis [28], we assume ρ to be constant in what follows, which reduces Eq. 4.3 to

$$\nabla \cdot \mathbf{u} = \frac{\mathrm{Q}(x, P)}{\rho} \,. \tag{4.4}$$

At the length scales involved ($\sim 100\,\mu$m) and for the measured values of tissue viscosity ($\sim 10^5$ Pa s [28, 133]), the dynamics can be safely assumed to be over-damped. In these conditions, momentum conservation reduces to local force balance, which reads

$$\nabla \cdot \sigma = 0 \,, \tag{4.5}$$

where σ is the stress tensor. For a viscous fluid with inhomogeneous viscosity $\mu(x)$ in 2D, the stress tensor reads

$$\sigma = -P\mathbf{I} + \mu(x) \left(\left(\nabla \mathbf{u} + \nabla \mathbf{u}^{\mathrm{T}} \right) - (\nabla \cdot \mathbf{u})\, \mathbf{I} \right) \,, \tag{4.6}$$

where $\mathbf{I}$ and P are the identity tensor and pressure field in the tissue, respectively. This pressure is not any hydrostatic pressure in the tissue but rather, the crowding pressure between cells in the tissue, mirroring the osmotic pressure in an aqueous foam [134]. While the density in the tissue is constant, the divergence of the velocity field does not generally vanish in Eq. 4.6 because of the addition of new material (see Eq. 4.4). The tissue is assumed to be immersed in a fluid environment similar to water (Newtonian fluid) with uniform viscosity several orders of magnitude smaller than that of the tissue. The equations governing the dynamics of the surrounding fluid are also mass and momentum conservation, but in this case, there are no sources of material.

Finally, to solve the equations above, it is necessary to specify the boundary condi-

tions. The shape of the tissue is not imposed in any way and depends on the physical fields inside the tissue. In the same way, these physical fields depend on the location of the boundary, i.e., the shape of the tissue. As for free-boundary problems related to the dynamics of fluid-fluid interfaces [135], the boundary conditions are velocity continuity and local normal force balance at the tissue boundary (or surface). Continuity of the velocity field simply reads

$$\mathbf{u}_{\text{in}} = \mathbf{u}_{\text{out}} \,, \tag{4.7}$$

where $\mathbf{u}_{\text{in}}$ and $\mathbf{u}_{\text{out}}$ are the velocities of the tissue and outer fluid surrounding it, respectively, evaluated at the boundary (tissue surface). Local normal force balance (Laplace's Law) reads

$$\Delta P = \gamma\kappa \,, \tag{4.8}$$

where ΔP is the tissue pressure jump at the boundary, γ is the tissue surface tension and κ is the curvature of the tissue surface. The interface between the tissue and surrounding fluid is described with a single curvature κ along its arc-length because the simulations are in 2D. Since the tissue pressure is not associated with any hydrostatic pressure, but rather it is a pressure associated with cellular crowding, its value outside the tissue vanishes. In this sense, the tissue pressure jump ΔP at the tissue surface is simply $\Delta P = P_S$, where P_S is the tissue pressure at the tissue boundary and, in general, varies on the tissue surface. The tissue surface tension γ considered here accounts for the tissue surface tension known to exist in multicellular systems with adhering cells, such as in tissues [136]. For simplicity, we assume here that at the relevant developmental time

scales and supracellular scales the tissue surface tension is constant in time and does not vary along the AP axis.

Since addition of material in the MPZ is essential to sustain body elongation, we scale all lengths with the characteristic length scale λ_Q, time with the characteristic timescale of cell ingression, $\tau \equiv \rho/Q_0$, and stresses with the critical pressure P_C over which cell ingression to the MPZ ceases. Scaling all variables and equations with the mentioned scales, we obtain the relevant dimensionless parameters that govern the dynamics of the system, which read

$$\frac{\lambda_\mu}{\lambda_Q}, \quad \frac{\sigma_\mathrm{C}}{P_\mathrm{C}}, \quad \frac{\sigma_\mathrm{A}}{P_\mathrm{C}}, \quad \frac{\sigma_\mathrm{P}}{P_\mathrm{C}} \tag{4.9}$$

where λ_μ/λ_Q is the ratio of the length scale over which tissue viscosity varies to the size of the region where cell ingression occurs (or tissue material is added, equivalently). Beyond this ratio, the other dimensionless parameters are ratios of the four relevant stress scales in the problem, namely the shear stress scale in the MPZ, σ_P, the shear stress scale in the PSM, σ_A, the capillary stress associated to the tissue surface, $\sigma_\mathrm{C} \equiv \gamma/\lambda_Q$, and the critical tissue pressure P_C over which cell ingression ceases. In analogy to fluid interfaces, the capillary stress measures how much stress is needed to deform the tissue surface. The ratio of shear stress scales directly relates to the ratio of tissue viscosities in each region, such that $\sigma_\mathrm{P}/\sigma_\mathrm{A} = \mu_\mathrm{P}/\mu_\mathrm{A}$, with $\mu_\mathrm{P}/\mu_\mathrm{A} = 1$ for uniform viscosity and $\mu_\mathrm{P}/\mu_\mathrm{A} \to 0$ for a jamming transition at vanishing tissue effective temperature [29, 137].

In order to narrow the parameter space, we use known experimental values for some parameters. Measurements of the size of the MPZ, λ_μ, and the size of the ingression

region λ_Q indicate that the relevant parameter range for λ_μ/λ_Q is $0.5 < \lambda_\mu/\lambda_Q < 2$. The range of $\sigma_{\rm P}/\sigma_{\rm A}$ explored is $10^{-3} - 1$, because we are interested in the limit of uniform tissue viscosity and the limit of $\mu_{\rm A} \gg \mu_{\rm P}$ representing the fluid-to-solid transition. We considered the ratio of capillary to critical pressure controlling $P_{\rm C}$, $\sigma_{\rm C}/P_{\rm C}$, to vary over a range $0.01 - 10$. We checked that the results show negligible dependence on the transition zone size a as long as a is sufficiently small. Consequently, we fix $a = \lambda_Q/4$ in our simulations.

4.3 Elongation regime

To understand the possible tissue shapes and the spatiotemporal variations in the different physical fields, we numerically integrated Eqs. 4.4-4.5 and obtained the time evolution of the system for different parameter values. Starting from an initial semicircular tissue shape, we let the tissue shape evolve over time and identify the different dynamical regimes of the system for different parameter values. For values of the capillary stress larger than a threshold value in the critical pressure, namely $\sigma_{\rm C}/P_C \simeq 4$, the tissue cannot extend in any way and remains arrested (Fig. 4.2). This is because tissue material (cells) cannot enter the MPZ due to the high crowding pressure in the MPZ (Fig. 4.2C), thus halting growth. This high pressure in the tissue is a direct consequence of the large capillary stress (as compared to P_C) that resists deformation and extension of the tissue surface.

Below the threshold value causing growth arrest (i.e., $\sigma_{\rm C}/P_C < 4$), the tissue can

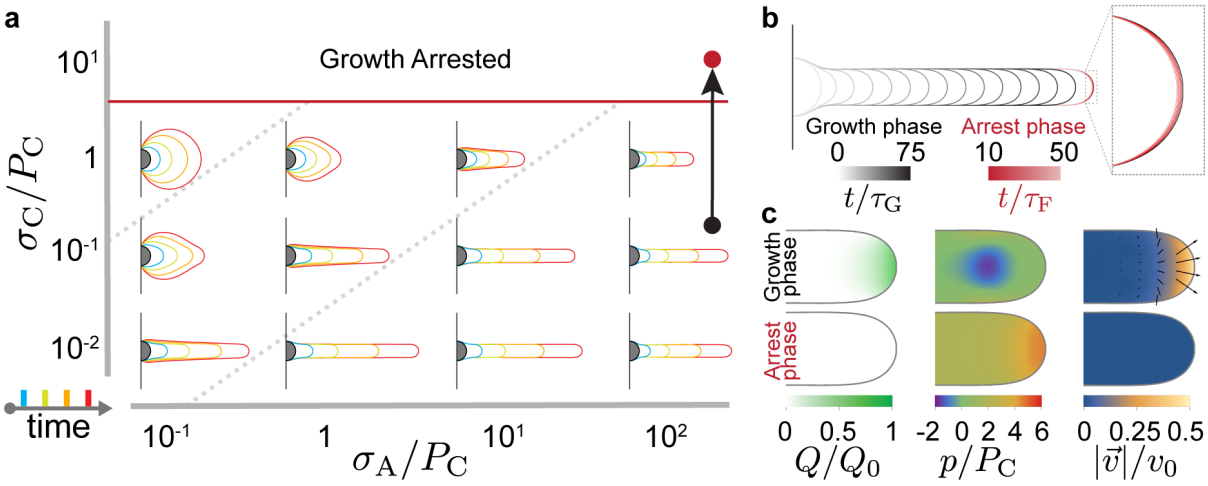

Figure 4.2: Time evolution of tissue shapes for various values of the parameters, starting from an initial semi-circular shape (gray). Four time snapshots are shown for each parameter combination, namely, $t/\tau = 10, 25, 50, 75$, all measured in material addition units of $\tau = \rho/Q_0$. The dotted lines indicate a separation between two regimes of arrested growth, due to the pressure of a cell's surrounding being higher that the critical pressure, and the growth phase which can be categorized into two regimes of unidirectional extension for capillary stress small compared to the critical pressure ($\sigma_C \ll P_C$), and isotropic extension with flow along the ML axis for large relative capillary stress ($\sigma_C \gg \sigma_P$). a) Increasing the ratio of anterior stress scale σ_A to the critical pressure P_C results in a larger capillary stress threshold for transitioning between unidirectional and isotropic growth b) The shape of the tissue is dependent upon the capillary stress σ_C c) The growth is arrested during unidirectional growth when the critical pressure over which cells no longer ingress is decreased. The rate at which cells ingress into the MPZ becomes zero.

extend, albeit differently for varying values of parameters. When the capillary stresses are much larger than the shear stresses both in the MPZ and the PSM ($\sigma_C \gg \sigma_P$ and $\sigma_C \gg \sigma_A$), it is much more costly to deform the tissue surface than to induce material flows within it. Consequently, in this regime, the tissue expands keeping a round shape, as would a liquid drop with high interfacial tension with liquid being injected in it (Fig. 4.2a,b). In contrast, when the capillary stresses are large compared to the shear stresses in the MPZ ($\sigma_P \ll \sigma_C$), but small compared to the shear stresses in the PSM

($\sigma_A \gg \sigma_C$; i.e., if the viscosity μ_A is large enough), the MPZ tissue can easily flow upon addition of new cells from dorsal tissues, but the PSM can barely flow within the timescales of tissue growth. Since anterior PSM tissues do not flow due to their large viscosity in this limit, they effectively behave as a solid at the timescales relevant to tissue morphogenesis. In this case, it is much less costly to deform the tissue at the posterior end that inducing any flow in the PSM and, as a result, the tissue extends unidirectionally and progressively builds a tubular structure (Fig. 4.2a,b) that resembles, both in shape and extension, body axis elongation in zebrafish [131, 122, 28]. Indeed, this situation, in which the PSM effectively behaves like a solid and the MPZ behaves like a fluid, corresponds to experimentally observed fluid-to-solid tissue transition from MPZ to PSM [28]. Since unidirectional axis elongation can only be achieved when the capillary stresses associated with the tissue surface tension are smaller than the shear stresses in the PSM, our results suggest that tissue surface tension in zebrafish posterior tissues is small compared to the other stress scales in the system.

In between these two limiting regimes (purely isotropic growth and unidirectional elongation), there is an intermediate regime that displays some characteristics of both. If the capillary stress scale becomes comparable to the shear stress scales ($\sigma_C \sim \sigma_A$ and $\sigma_C \sim \sigma_P$), then the tissue expands mostly isotropically but also displays a posterior bump in the tissue shape due to the localized addition of cells in that region (Fig. 4.2a, intermediate region (INT)). In this case, the viscosity in the PSM is not large enough to support the posterior unidirectional extension of the tissue and prevent mediolateral

tissue spreading over the timescales of tissue morphogenesis, but it is neither small enough to fully prevent it. As a consequence, the tissue spreads mediolaterally at the anterior end, leading to a blob-like anterior tissue expansion in this region, while displaying a posteriorly extending bump at the posterior end.

Increasing the capillary stress above the critical value ($\sigma_{\mathrm{C}}/P_C \simeq 4$) as the tissue is elongating causes the tissue to arrest growth (Fig. 4.2b). The timescale of fluidization ($\tau_{\mathrm{F}} = \sigma_{\mathrm{C}}/\mu_{\mathrm{P}}$) is much shorter than the timescale of growth and only over a large t/τ_{F} do we see the tissue slightly retract due to the capillary stress being larger than the shear stress as seen in the inset of Fig. 4.2b. As the cell is growing, cells ingress normally at the posterior end. However, after the capillary stress is increased, cell ingression stops (Fig. 4.2c). The crowding pressure in the MPZ is higher than the pressure during growth due to the increase of capillary stress (Fig. 4.2c). During the growth phase, we see a high velocity leading to elongation of the tissue. Interestingly, after the increase of capillary stress, the velocity becomes negligible (Fig. 4.2c).

The different dynamical regimes of tissue expansion (Fig. 4.2a) will, in general, be characterized by different morphogenetic flows. In the case of isotropic tissue expansion with uniform tissue viscosity ($\sigma_{\mathrm{C}} > \sigma_{\mathrm{A}} = \sigma_{\mathrm{P}}$), strong mediolateral flow is observed to redistribute the tissue material added at the posterior end of the tissue (Fig. 4.3a). Indeed, in this case the capillary stresses are larger than all shear stresses in the tissue, forcing the material added at the posterior-most tissue end to redistribute mediolaterally while preserving a nearly spherical tissue shape during expansion. Since the shear stresses

are much smaller than the capillary stress, the tissue can easily flow and quickly reduce pressure differences, leading to an almost uniform tissue pressure inside the isotropically expanding tissue.

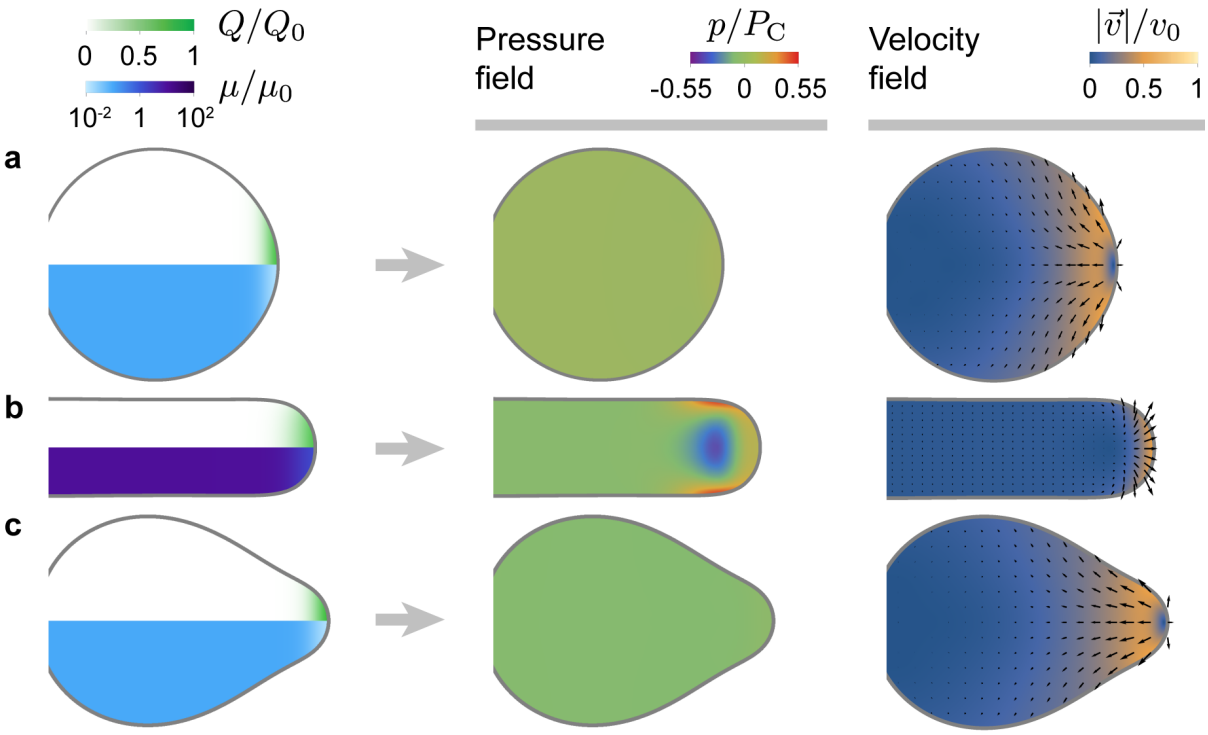

Figure 4.3: Tissue pressure and velocity of morphogenetic flows for three limiting regimes. The left column shows the tissue viscosity normalized to posterior viscosity and normalized growth rate. Pressure is normalized with the critical pressure, P_C, and velocity with $v_0 = \lambda_Q/\tau$. a) No fluid-to-solid transition between the posterior and anterior tissues, with large capillary stress ($\sigma_C \gtrsim \sigma_A = \sigma_P$). b) Large capillary stress in the presence of fluid-to-solid transition between the posterior and anterior tissues ($\sigma_A \gg \sigma_C = \sigma_P$). $\lambda_\mu = 2\lambda_Q$ c) Large capillary stress in the presence of fluid-to-solid transition between the posterior and anterior tissues ($\sigma_A \gg \sigma_C < \sigma_P$). $\lambda_\mu = 2\lambda_Q$.

In the regime where the tissue extends unidirectionally and posteriorly (Fig. 4.2a, regime U and Fig. 4.3b,c), most of the newly added tissue material flows posteriorly, contributing to the posterior tissue elongation, with the tissue just anterior of this region reversing direction and flowing anteriorly to virtually arrest just further where the tissue

viscosity sharply increases (solid-like PSM). As explained above, this is because it is less costly to create new tissue surface and extend posteriorly than moving the PSM material to accommodate the new material, as $\sigma_{\mathrm{A}} \gg \sigma_{\mathrm{C}} \sim \sigma_{\mathrm{P}}$. Far away from the extending end of the tissue, in the PSM, the flow is arrested and the tissue is uniformly slightly compressed (positive low pressure). In between these limiting posterior and anterior velocity behaviors, the tissue morphogenetic flows can display different patterns that we discuss below. For the specific cases shown in Fig. 4.3, the tissue displays posterior-directed velocities at the posterior end that progressively turn to anterior directed velocities with decaying magnitude towards the anterior end. Since in this limit the PSM is effectively solid, no mediolateral flow is possible in the PSM. Essentially, the material added at the posterior end flows posteriorly, elongating the tissue unidirectionally in the posterior direction, with a small backflow away from the extending tip (due to momentum conservation). The pressure profile displays a negative pressure zone in the medial region, just anterior of the region where new material is added, flanked mediolaterally by two regions of high pressure. A negative pressure indicates that the tissue is being pulled in all directions. The reason for this region of negative pressure in 2D is that the tissue at the posterior-most end expands quickly posteriorly, whereas the solid-like anterior tissues cannot flow fast. Since the tissue is considered to be a continuum incompressible material, the tissue in between the solid-like PSM and the posteriorly expanding MPZ needs to follow the posterior expansion at one end while keeping connection with the PSM at the other, leading to an effective pull on the tissue and a negative pressure. It

is important to note that this negative pressure region may be due to the 2D nature of these simulations, as in the full 3D geometry the capillary stresses from the other spatial direction would create higher pressures in the tissue, likely preventing the formation of negative pressure regions. Yet, the reported spatial distribution of pressures would most likely remain qualitatively the same, with a medial region of small pressure localized anteriorly from where material is added. The high pressure regions flanking the low pressure medial region are due to the fact that the flow in this region is anterior directed and encounters a very large anterior resistance due to the increasing viscosity towards the PSM, effectively compressing the tissue.

Finally, in the intermediate regime, the morphogenetic flows show characteristics of both the isotropic growth with strong mediolateral and anterior directed flows and a small bump with small posterior directed velocities in a small posterior region.

4.4 Topological transitions in the structure of morphogenetic flows

In order to understand the types of morphogenetic flows that are involved in extending the posterior body axis, we explore the parameter space in the regime where there is a fluid-to-solid tissue transition ($\mu_{\mathrm{A}} \gg \mu_{\mathrm{P}}$) and the capillary stresses are less than or equal to the shear stress in the PSM, leading to unidirectional body elongation.

Varying the ratio of capillary stress to shear stress in the PSM ($\sigma_{\mathrm{C}}/\sigma_{\mathrm{A}}$) shows that

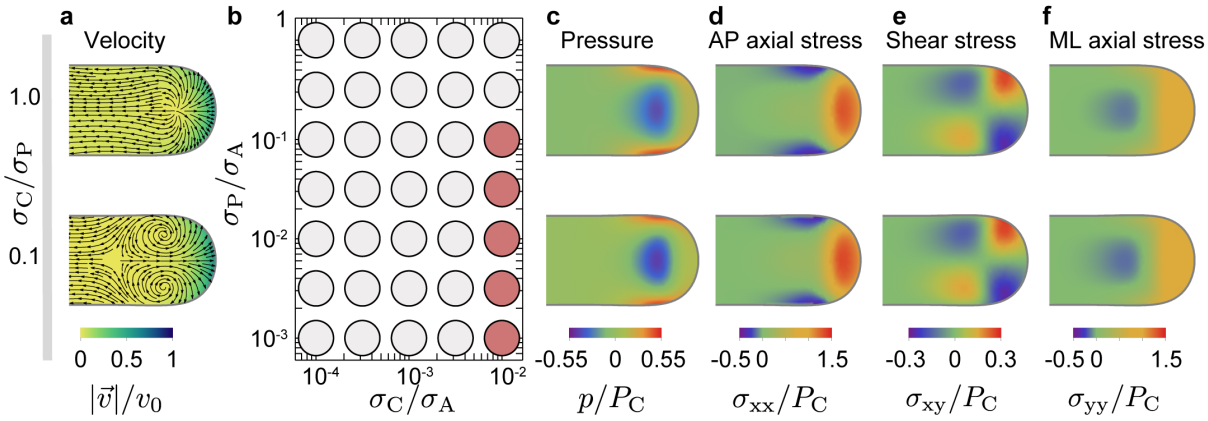

Figure 4.4: Morphogenetic flows near or anterior to the material addition zone for increasing capillary stress. Counter-rotating vortices are present when capillary stress σ_c is small compared to the MPZ shear stress σ_p, and when the fluid-to-solid and material addition transition zones are sufficiently close.a) AP axial stress,σ_{xx}, showing streamlines highlighting the morphogenetic flows b) ML axial stress, σ_{yy}, c) shear stress, σ_{xy}, and d) a phase diagram showing that the disappearance of vortices occur as the capillary stress increases.

morphogenetic flows transit from a source-type flow to displaying two counter-rotating vortices as σ_C/σ_A decreases (Fig. 4.4a,b). This is a topological transition in the structure of the flow field. The source-type flow has a topological charge of +1, whereas in the presence of the two counter-rotating vortices (with topological charges +1) a stagnation point with topological charge -1 appears in the PSM, thereby conserving the topological charge through the transition (Fig. 4.4a). The counter-rotating vortices appear just anterior from the location where the tissue viscosity sharply increases (location of the fluid-to-solid tissue transition). This is because when capillary stresses are small compared to even the smaller MPZ shear stress σ_P (limit of vanishing capillary stress), the added material forced to move anteriorly eventually encounters the solid-like PSM and, since extending the tissue posteriorly has little cost for vanishing tissue surface tension, it progressively reverses its direction to medial, posterior-directed flows, generating the

vortices. For larger capillary stress, this flow reversal cannot occur because it is too costly to deform the tissue surface and extend the body axis.

Even if the tissue morphogenetic flows undergo a topological transition that considerably affects their structure, the stress fields and tissue shape are remarkably similar for the two flow structures (with or without counter-rotating vortices). For unidirectionally extending tissues, and regardless of the flow structure: (1) the axial stress σ_{xx} (Fig. 4.4d) shows strong uniaxial extension in the MPZ and weak compression in the PSM as well as flanking lateral regions with increased uniaxial compression as the tissue transits from fluid-like to solid-like behavior; (2) the mediolateral stresses σ_{yy} (Fig. 4.4f) display uniaxial extension in the MPZ and weak compression in the PSM, with a medial compressive region located anterior of the fluid-to-solid transition; (3) the shear stress (Fig. 4.4e) is large in the MPZ with two localized regions of high magnitude and it vanishes in the PSM; (4) the tissue pressure shows the characteristics described above for unilateral posterior tissue extension.

4.5 Comparing experiment and theory

Qualitatively, the theoretical results match some of the fields exhibited during zebrafish axis elongation. The experiments were carried out by Dr. Georgina Stooke-Vaughan and the experimental data analysis was performed by Dr. Sangwoo Kim.

Labeled nuclei, as seen in Fig 4.5a, were tracked and their positions and velocities were obtained using Imaris as explained in section 4.7. From the experimental data,

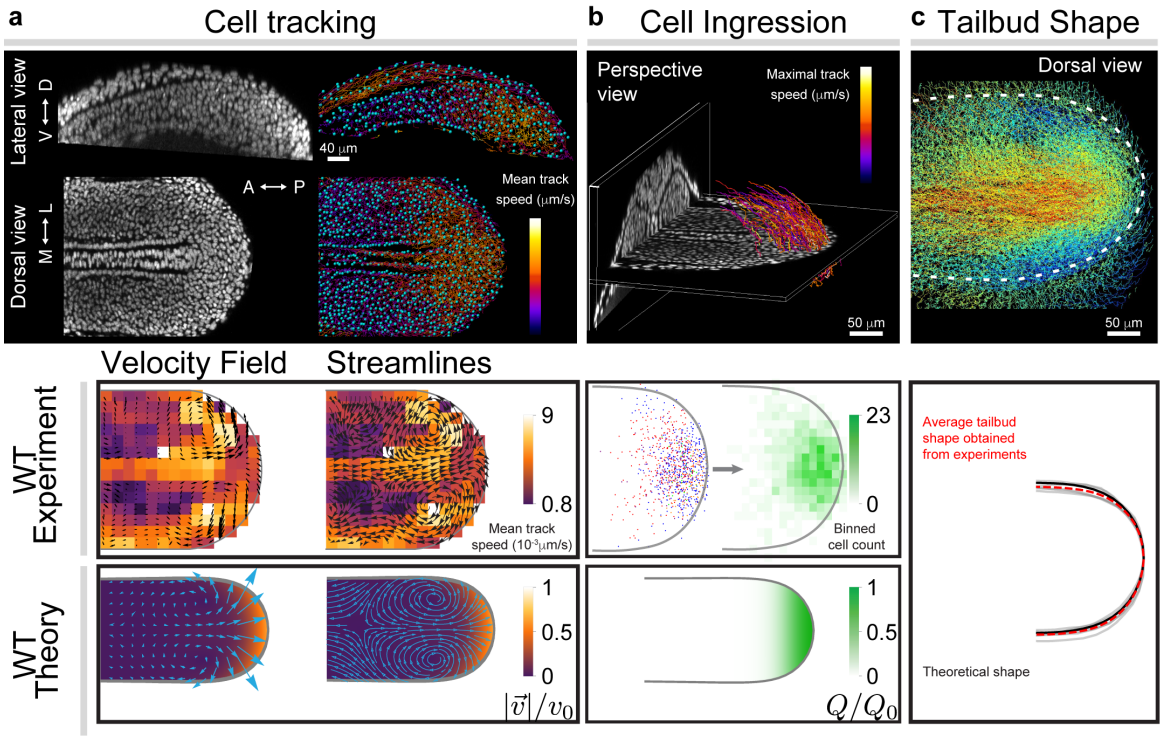

Figure 4.5: a) Experimental data showing lateral and dorsal views of the zebrafish embryo at the 10 somite stage. On the right nuclei are shown in blue and tracks of the nuclei are shaded with the mean track speed. Below, the velocity vectors and streamlines are shown with the speed shaded and at the bottom the theoretical velocity vectors and streamlines are shown with the speed shaded. b) Tracks of $30\mu m$ are shown with the maximal track speed shaded, below are the points at which cells cross the interface between the dorsal and ventral plane with the number of cells in a given bin of width $10\mu m$ on the left, at the bottom is the cell ingression field obtained from theoretical simulations c) The track are shown shading the anterior posterior velocity showing how cells move in opposite directions for the different tissue regions highlighting the shape of the MPZ and PSM, below in a red dashed line is the averaged shape over 5 samples and the black line represents the shape of the tissue from theoretical simulations.

the velocities were averaged and binned (see section 4.7 for further details) to find the speed and the vectoral components of the velocity at a given point. Counter rotating vortices are seen, in front of which the cell moves posteriorly and behind the vortices the tissue is seen to flow anteriorly. The streamlines show the morphogenetic flows 4.5a. The presence of the notochord makes it difficult to visualize the stagnation point in the

flow seen in theoretical predictions. Nuclei moving distances greater than or equal to $30\mu m$ from the dorsal tissue into the MPZ are seen in 4.5b. The number of cells crossing the dorsal ventral interface at a given location is counted and binned (bin width $10\mu m$). The cell ingression region seems to be more spherical than the cell ingression region used in theory. Finally, the tailbud shape is obtained by looking at images obtained from Imaris color coding the velocity along the anterior-posterior axis (Fig. 4.5c), the red hues indicate a velocity in the posterior direction while the blue hues represent a velocity in the anterior direction. This helps us trace the shape using ImageJ. The shapes from 5 embryos are averaged as given by the red dashed line in Fig. 4.5c. The black line shows the shape obtained from the theory. The theoretical shape is influenced by the cell ingression region which is different from experiments as we saw in Fig. 4.5b and would perhaps more closely capture the shape if a similar rounded cell ingression region was used in simulations. Qualitatively the morphogenetic flows which are crucial to shaping the embryo is similar and it would be interesting to further explore the morphogenetic flows of mutant zebrafish embryos.

4.6 Discussion

We have studied the role of spatially-localized fluid-to-solid tissue transitions in the control of tissue morphogenesis and specifically, in the elongation of the vertebrate body axis. By using finite element simulations to physically describe tissue morphogenesis at supracellular scales, we showed that unidirectional body elongation, with minimal lat-

eral tissue spreading, occurs naturally in the presence of a fluid-to-solid tissue transition in the AP axis. In the absence of this spatially-localized fluid-to-solid tissue transition, posterior tissues expand isotropically or display considerable lateral spreading, but fail to form body axis that extends unidirectionally at its posterior end. Moreover, in the case of unidirectional body elongation, we predict the tissue morphogenetic flows and find a topological transition.

Previous theoretical models have described the cell movements during axis elongation, albeit for DM tissues. In those cases, the simulations were cell-based and assumed a fixed geometry of the tissue (boundary) that did not evolve in time. Since the geometry was fixed, those simulations could not describe morphogenesis and instead focused on studying movements of cells in DM and PZ tissues. In contrast, our description focuses on ventral tissues (PSM and MPZ), for which detailed mechanical information is available. The tissue is characterized as a continuum that can undergo large shape changes (a free-boundary problem). This continuum approach has been used to theoretically study several instances of morphogenesis both for tissues and cells. In most cases though, the spatiotemporal variations of key input physical fields in the simulations, such as the tissue material properties, are unknown, limiting the predictive power of those theoretical analyses. Instead, here we made use of recent experimental data for key physical fields at play during posterior body axis elongation.

The sustained posterior elongation of the body axis requires a constant addition of cells. The required tissue material to elongate the body axis posteriorly comes from

the dorsal tissues, where cells display strong coherent posterior directed movements and eventually move ventrally upon reaching the body end. Cell ingression into the MPZ can only occur if enough space can be made available for the ingressing cells, which depends directly on the local tissue pressure (local volume changes are directly related to the local value of the pressure): large tissue pressure in the MPZ will prevent ingression of cells from DM tissues because these cannot generate enough force to push their way into the MPZ. This causes growth to arrest.

The predicted morphogenetic flows (velocity field) for simulated unidirectional body elongation, indicates that two potential patterns exist depending on the relevance of tissue tension. At low tissue tensions, two counter-rotating vortices are observed in the tissue, just as it is transiting to a solid-like state. This predicted flow pattern is not obvious and arises naturally from the dynamics of the system. Importantly, counter-rotating vortices are observed in the extending body axis as seen in Fig. 4.5a.

It has been shown that zebrafish mutants lacking the notochord can properly extend the posterior body axis. For this reason, and also for simplicity, we did not consider the presence of the notochord in these simulations. While we believe that the presence of the notochord does not change the obtained results qualitatively, it may impose slightly different boundary conditions close to the midline that may slightly modify the tissue flows in that region. However, the predicted tissue flows strongly resemble the observed morphogenetic flows even in the absence of the notochord.

Overall, our results indicate that the presence of a fluid-to-solid transition as cells

transit from the MPZ to the PSM is essential to mechanically sustain unidirectional posterior elongation. In the absence of the transition, the tissue surface tension prevents unidirectional extension and an isotropic tissue expansion is observed. It would be interesting to explore whether a fluid-to-solid transition occurs in other developing embryos as well.

4.7 Experimental and computational methods

Experiments were done by Dr. Georgina Stooke-Vaughan and data analysis was done by Dr. Sangwoo Kim.

Zebrafish husbandry, lines and experimental manipulations.

Zebrafish (Danio rerio) were maintained under standard conditions [138]. Animal husbandry and experiments were done according to protocols approved by the Institutional Animal Care and Use Committee (IACUC) at the University of California Santa Barbara. Nuclei were labeled to track cell movements by either using the Tg(h2afva:GFP)kca6 transgenic line [139] or by injection with 80-100pg H2B-RFP mRNA at 1-2 cell stage.

Microscopy

8-10 somite stage zebrafish embryos were mounted in 1% low-melting point agarose in a glass bottom petri dish (MatTek Corporation) for a dorsal view of the tailbud and imaged at 25C using an inverted Zeiss Laser Scanning Confocal (LSM 710, Carl Zeiss

Inc.). Confocal stacks through the tailbud were acquired with a step size of 2 μm and time interval of 2 minutes for 2 hours, using a 25x water immersion objective (LD LCI Plan-Apochromat 25x/0.8 Imm Corr DIC M27, Carl Zeiss Inc.). Imaris (Bitplane) was used to prepare figure panels showing embryonic data, detected nuclei and tracks.

Cell movement tracking

Data was processed using Imaris (Bitplane). First, data was smoothed using a 1-pixel Gaussian filter, next to correct for photo-bleaching over time the normalize timepoints function was used, then attenuation correction was applied to correct for z-attenuation. If required, the free-rotate tool was used to align the data such that all samples had the same alignment with respect to Cartesian coordinates. The Measurement Points tool was used to identify scaling points for the data and define the plane of cell ingression. After processing, nuclei were detected using the spots function, and tracked using the Brownian motion algorithm. Nuclei positions and velocities were output for further analyses.

Velocity field analysis

Nucleus position data from Imaris is used to compute velocity field. For each cell trajectory, B-spline curve is first computed to eliminate high frequency movements. Velocity values are computed from the B-spline curve using central different formula. Velocity values are further averaged spatially and temporally to obtain smooth velocity field. All velocity values are projected on xy plane and binned in terms of x and y positions with

a bin width $10\mu m$.

Cell ingression analysis

To identify cell ingression rate, cells that exhibit displacement in dorsal-ventral axis larger than $30\mu m$ are selected. For each cell trajectory, all time points that cell is located in the dorsal-ventral boundary region ($10\mu m$ thickness) are identified and x and y positions are averaged over the identified time points. Cell ingression positions are measured over 5 distinct samples. To take binning cell ingress rate from different samples, body axes are rescaled by a distance between tail end and posterior end of notochord and origin is moved to tail end. Cell ingression rate is binned in terms of x and y positions.

Computational Methods

We solve Eqs. 4.3- 4.5 with the boundary conditions described above using Comsol Multiphysics 5.3, which employs Finite Element Methods. Laminar flow and moving mesh models were used to simulate large deformations of the tissue material under growth.

The Comsol model consists of a box, with sides of length 50 times larger than the tissue size, filled with a fluid of negligible viscosity, and the tissue initially contained in a semicircular region with both ends fixed to one side of the box. The tissue satisfies the source and viscosity profiles (Eqs. 4.1, 4.2). Fluid addition at the tip and the isotropic term ($\nabla \cdot \mathbf{u}$) in Eq. 4.6 are directly inputted into the weak solution integration formulation of Comsol. No tissue flow can go through the box and pressure is set to zero at far away

walls. The system is meshed with the smallest element being 130 times smaller than the radius of the initial semicircular area close to the tissue-fluid and tissue-box interfaces, with the mesh updating as needed to accommodate large deformations resulting from tissue growth.

Chapter 5

Conclusions

Nature has made forms in a variety of shapes and sizes. More than 20 centuries ago, Aristotle and other philosophers realized that that the egg of an animal contained the information required for determining its final form, while *not* being a miniature version, which simply expanded into an adult. In developmental biology, morphogenesis deals with the organization of shape and is the result of spatial patterning (the setting up of locations in space for future events) combined with temporal regulation (the control of the relative timing of events). These processes are triggered by biochemical signaling yielding changes in protein activity and gene expression. Mutations in the DNA can result in morphological changes and determine the fitness of a species under selection pressure. Morphogenesis is fundamentally important because it is ultimately responsible for the physiology and even the behavior of an organism.

Understanding the physical aspects leads to more complete picture than the common

approach of looking at gene expression and biological signatures. Even more important, the laws of physics can impose important constraints on the shape of the growing biological form. Interestingly, our work has shown that this top down approach yields novel insights on the key biochemical processes and genes underlying morphogenesis, in the case of the yeast mating projection. Our theoretical description of yeast mating projection growth, in chapter 2, was based on the first principles of physics and showed the need for coordination of the biological and physical processes underlying growth in order for stable growth to occur. A genetically encoded mechanical feedback through the cell wall integrity pathway is shown to be essential to ensure that the physical expansion of the cell wall is coupled to the synthesis of new cell wall material. The mechanical feedback not only stabilizes the growth but is also involved in another key process of the growth, polarization, as we show in Chapter 3. In order for the cell to grow unidirectionally, the cell must maintain its polarization cap at the site of growth. We showed that this can be achieved by the cell obtaining information about its geometry also through the cell wall integrity pathway. This was a new approach compared to previous studies, which ignored the spatial context of polarization and focused merely on obtaining and maintaining a single polar cap in a spherical geometry. Polarization is a critical component for cell migration, growth, division, and signal propagation. Directed cell migration occurs when cells polarize to have a front. This creates a leading edge of the cell, which extends in the direction of motion and the back of the cell trails behind. Dictyostelium and leukocytes exhibit this rapid process and have migration speeds of 10-25 $\mu m/s$ [140]. These cells

must rapidly. on the time scale of minutes, change their shape due to their polarized state and it would be interesting to understand if they use a similar mechanical feedback mechanism. Note that the mechanical feedback mechanism we found for growth is operational on the time scale of hours. Looking at the physical aspects of growth led us to a better understanding of the key biological processes such as the tuning of material properties, which we show is not only relevant to the elongation of cells but also to the elongation of tissues.

An important and surprising finding is that nature exploits the same physical mechanism, localized fluid to solid transitions, in two entirely different contexts – the morphogenesis of individual cells and of multicellular structures. The recurrent use of the same theme in seemingly dissimilar situations is a remarkable example of convergent evolution. In Chapter 4, we show that the presence of a fluid-to-solid transition in the zebrafish tissue is essential to explain the extension of the zebrafish body axis and the morphogenetic flows in the tissue. It was relatively unknown that a fluid to solid transition could facilitate elongation in the tissue and most studies focused on elongation by convergent extension [141]. These include notochord formation in the Xenopus laevis embryo [142] and neural tube formation in the mouse embryo [143] and even zebrafish axis elongation [144]. However convergent extension flow patterns are not what is seen in experiments. Instead flows with counter rotating vortices, which is a distinct prediction of the flow pattern in our theoretical description, are observed. Remarkably, in the absence of the fluid to solid transition along the body axis, the tissue does not elongate. It would be

interesting to assess whether any zebrafish mutants exhibit the source-type flow and its relationship to an increase in surface tension. Further work is needed to understand the interplay between the biological and physical processes underlying tissue morphogenesis.

Nature amazingly exploits the distinct physical phases of biological structures to control morphogenesis just as D'Arcy Thompson predicted a century ago. Our studies teach us that emergence [145] (the whole being greater than the sum of the interacting parts) provides the link between the molecular and genetic mechanisms and the system-wide development of morphology. It is even more intriguing that nature uses the same tricks (in our case, the mechanical feedback) to accomplish seemingly distinct tasks (stabilize cell growth and maintain cell polarization). The robustness of morphogenesis underscores the importance of the emergent orchestration in space and in time of the key players within the cell.

Appendix A

Experimental Details

Table A:

Strain	Genotype	Source
RJD863	*MAT**a** can1-100 leu2-3-112 his3-11-15 trp1-1 ura3-1 ade2-1 bar1::hisG*	Ray Deshaies
CGY003	RJD863 *wsc1Δ::KAN^R*	This study
CGY004	RJD863 *mid2Δ::KAN^R*	This study
CGY005	RJD863 *wsc1Δ::HIS5 mid2Δ::KAN^R*	This study
CGY011	RJD863 *sec3Δ::SEC3-GFP-HIS5*	This study
CGY012	RJD863 *sec3Δ::SEC3-GFP-HIS5 mid2Δ::KAN^R*	This study
CGY013	RJD863 *sec3Δ::SEC3-GFP-HIS5 wsc1Δ::LEU2^{Kl}*	This study
CGY015	RJD863 *sec3Δ::SEC3-GFP-HIS5 spa2Δ::LEU2^{Kl}*	This study
CGY016	RJD863 *sec3Δ::SEC3-GFP-HIS5 spa2Δ::LEU2^{Kl} mid2Δ::KAN^R*	This study
CGY017	RJD863 *sec3Δ::SEC3-GFP-HIS5 spa2Δ::LEU2^{Kl} wsc1Δ::URA3^{Kl}*	This study

Table B:

Parameter	Description	Value
P	Turgor pressure of budding yeast	0.6 ± 0.2 MPa [146]
ρ_w	Density of 1,3-β glucans in cell wall	–
μ_0	Apical viscosity of cell wall	–
m_w	Mass of 1,3-β glucan monomer	–
ρ_0	Density of Fks1/2 enzymes in vesicle	–
k_p	Extrusion rate of 1,3-β glucan monomers	–
λ_X	Exocytosis length-scale	$0.6 \pm 0.1\mu$m [48]
		$0.45 \pm 0.10\mu$m [82]
λ_D	Endocytosis length-scale	$1.05 \pm 0.18\mu$m [82]
k_X^0	Apical rate of exocytosis	$0.045s^{-1}$ [85]
k_D^0	Apical rate of endocytosis	$0.02 \pm 0.02s^{-1}$ [82]
		$0.027s^{-1}$ [85]
k_{off}	Inactivation rate of Fks1/2	–

Bibliography

[1] D.W.T Thompson. *On Growth and Form*. Cambridge University Press, 1917.

[2] G.T. Reeves, C.B. Muratov, T. Schüpbach, and S.Y. Shvartsman. Quantitative Models of Developmental Pattern Formation. *Developmental Cell*, 11(3):289–300, September 2006.

[3] G.A. Stooke-Vaughan and O. Campàs. Physical control of tissue morphogenesis across scales. *Current Opinion in Genetics & Development*, 51:111–119, 2018.

[4] C. Charlier and D. Dunia. *Neurons, confocal fluorescence microscopy*. www.zeiss.com/confocal, https://www.flickr.com/photos/75834543@N06/8695004301, CC BY-NC-ND 2.0, 2013.

[5] Chiba H., Sakai N., Murata M., Osanai M., Ninomiya T., Kojima T., and Sawada N. *Microvilli*. https://www.flickr.com/photos/43875334@N07/4077864405, 2006.

[6] Ronnydv10. *Spores and hyphae of M. roreri*. 2013.

[7] D. Menshykau, O. Michos, C. Lang, and et al. *The image-based modeling approach*. Nature Communications, 2019.

[8] Bonert M. *Small intestine neuroendocrine tumour low mag*. 2011.

[9] D. Sweetman, L. Wagstaff, O. Cooper, and et al. *Chicken primitive streak cell fate*. BMC Developmental Biology, 2008.

[10] Lodish H., Berk A., Zipursky S.L., Matsudaira P., Baltimore D., and J. Darnell. *Molecular Cell Biology*. W. H. Freeman, New York, 2000.

[11] F.M. Harold. *The Way of the Cell*. Oxford University Press, New York, 2001.

[12] J. Kroeger and A. Geitmann. The pollen tube paradigm revisited. *Current opinion in plant biology*, 15(6):618–624, 2012.

[13] R.R. Lew. How does a hypha grow? The biophysics of pressurized growth in fungi. *Nature Publishing Group*, 9(7):509–518, 2011.

[14] R. Bernal, E. Rojas, and J. Dumais. The mechanics of tip growth morphogenesis: what we have learned from rubber balloons. *JOMMS*, 2(6):1157–1168, 2007.

[15] B.B. Goodwin and L.E.H. Trainor. Tip and Whorl Morphogenesis in Acetabularia by Calcium-Regulated Strain Fields. *Journal of Theoretical Biology*, 117:79–106, 1985.

[16] S. Bartnicki-Garcia, F. Hergert, and G. Gierz. Computer simulation of fungal morphogenesis and the mathematical basis for hyphal (tip) growth. *Protoplasma*, 153, 1989.

[17] S.H. Tindemans, N. Kern, and B.M. Mulder. The diffusive vesicle supply center model for tip growth in fungal hyphae. *Journal of Theoretical Biology*, 238(4):937–948, 2006.

[18] A. Goriely and M. Tabor. Self-Similar Tip Growth in Filamentary Organisms. *Phys. Rev. Lett.*, 90(10):108101–4, 2003.

[19] J.A. Lockhart. An Analysis of Irreversible Plant Cell Elongation. *Journal of Theoretical Biology*, 8:264–275, 1965.

[20] B. Goldenbogen, W. Giese, M. Hemmen, J. Uhlendorf, A. Herrmann, and E. Klipp. Dynamics of cell wall elasticity pattern shapes the cell during yeast mating morphogenesis. *Open Biology*, 6(9):160136–14, 2016.

[21] J.F. Abenza, E. Couturier, J. Dodgson, J. Dickmann, A. Chessel, J. Dumais, and R.E.C. Salas. Wall mechanics and exocytosis define the shape of growth domains in fission yeast. *Nature Communications*, 6:1–13, 2015.

[22] T. Drake and D. Vavylonis. Model of Fission Yeast Cell Shape Driven by Membrane-Bound Growth Factors and the Cytoskeleton. *PLoS computational biology*, 9(10):e1003287, 2013.

[23] O. Campàs and L. Mahadevan. Shape and Dynamics of Tip-Growing Cells. *Current Biology*, 19(24):2102–2107, 2009.

[24] A. Mogilner, J. Allard, and R. Wollman. Cell Polarity: Quantitative Modeling as a Tool in Cell Biology. *Science*, 336(6078):175–179, 2012.

[25] S.J. Altschuler, S.B. Angenent, Y. Wang, and L.F. Wu. On the spontaneous emergence of cell polarity. *Nature*, 454(7206):886–889, 2008.

[26] M. Trogdon, B. Drawert, C. Gomez, S.P. Banavar, T.M. Yi, O. Campàs, and L.R. Petzold. The effect of cell geometry on polarization in budding yeast. *PLoS Computational Biology*, 14(6):e1006241–22, 2018.

[27] B. Bénazéraf and O. Pourquié. Formation and Segmentation of the Vertebrate Body Axis. *Annual Review of Cell and Developmental Biology*, 29(1):1–26, 2013.

[28] A. Mongera, P. Rowghanian, H.J. Gustafson, E. Shelton, D.A. Kealhofer, E.K. Carn, F. Serwane, Ad.A. Lucio, J. Giammona, and O. Campàs. A fluid-to-solid jamming transition underlies vertebrate body axis elongation. *Nature*, 45:1–21, 2018.

[29] D. Bi, J.H. Lopez, J.M. Schwarz, and M. L. Manning. A density-independent rigidity transition in biological tissues. *Nature Physics*, 11(12):1074–1079, 2015.

[30] E. Hannezo, J. Prost, and J-F. Joanny. Theory of epithelial sheet morphology in three dimensions. *PNAS*, 111:27–32, 2014.

[31] D. Bi, J.H. Lopez, J.M. Schwarz, and M.L. Manning. Energy barriers and cell migration in densely packed tissues. *Soft Matter*, 10(12):1885–6, 2014.

[32] E. Schötz, M. Lanio, J.A. Talbot, and M.L. Manning. Glassy dynamics in three-dimensional embryonic tissues. *Journal of the Royal Society Interface*, 10(89):20130726–11, 2013.

[33] T.E. Angelini, E. Hannezo, X. Trepat, M. Marquez, J.J. Fredberg, and D.A. Weitz. Glass-like dynamics of collective cell migration. *PNAS*, 108:4714–4719, 2011.

[34] D.B. Staple, R. Farhadifar, J.C. Röper, B. Aigouy, S. Eaton, and F. Julicher. Mechanics and remodelling of cell packings in epithelia. *The European Physical Journal E*, 33(2):117–127, 2010.

[35] N. Murisic, V. Hakim, I.G. Kevrekidis, S.Y. Shvartsman, and B. Audoly. From Discrete to Continuum Models of Three-Dimensional Deformations in Epithelial Sheets. *Biophysj*, 109(1):154–163, 2015.

[36] B. Boehm, H. Westerberg, G. Lesnicar-Pucko, S. Raja, M. Rautschka, J. Cotterell, J. Swoger, and J. Sharpe. The Role of Spatially Controlled Cell Proliferation in Limb Bud Morphogenesis. *PLoS Biology*, 8(7):e1000420–21, July 2010.

[37] R. Dillon and Othmer H.G. A Mathematical Model for Outgrowth and Spatial Patterning of the Vertebrate Limb Bud. *Journal of Theoretical Biology*, 197:295–330, March 1999.

[38] B. Szabó, G.J. Szöllösi, B. Gönci, Zs. Jurányi, D. Selmeczi, and T. Vicsek. Phase transition in the collective migration of tissue cells: Experiment and model. *Physical Review E*, 74(6):061908–5, December 2006.

[39] A.K. Lawton, A. Nandi, M.J. Stulberg, N. Dray, M.W. Sneddon, W. Pontius, T. Emonet, and S.A. Holley. Regulated tissue fluidity steers zebrafish body elongation. *Development*, 140(3):573–582, 2013.

[40] D. Das, V. Chatti, T. Emonet, and S.A. Holley. Patterned Disordered Cell Motion Ensures Vertebral Column Symmetry. *Developmental Cell*, 42(2):170–180.e5, 2017.

[41] D. Das, D. Jülich, J. Schwendinger-Schreck, E. Guillon, A.K. Lawton, N. Dray, T. Emonet, C.S. O'Hern, M.D. Shattuck, and S.A. Holley. Organization of Embryonic Morphogenesis via Mechanical Information. *Developmental Cell*, pages 1–17, May 2019.

[42] A.J. Engler, P.O. Humbert, B. Wehrle-Haller, and V.M. Weaver. Multiscale modeling of form and function. *Science*, 324(5924):208–212, 2009.

[43] K.D. Young. The selective value of bacterial shape. *Microbiology and molecular biology reviews : MMBR*, 70(3):660–703, 2006.

[44] W.J. Nelson. Adaptation of core mechanisms to generate cell polarity. *Nature*, 422(6933):766–774, 2003.

[45] E. Cabib and J. Arroyo. How carbohydrates sculpt cells: chemical control of morphogenesis in the yeast cell wall. *Nature Reviews Microbiology*, 11(9):648–655, 2013.

[46] A. Geitmann and J.K.E. Ortega. Mechanics and modeling of plant cell growth. *Trends in plant science*, 14(9):467–478, 2009.

[47] F.M. Harold. Force and compliance: rethinking morphogenesis in walled cells. *Fungal genetics and biology : FG & B*, 37(3):271–282, 2002.

[48] S.P. Banavar, C. Gomez, M. Trogdon, L.R. Petzold, T.M. Yi, and O. Campàs. Mechanical feedback coordinates cell wall expansion and assembly in yeast mating morphogenesis. *PLoS Computational Biology*, 14(1):e1005940–19, 2018.

[49] F.M. Harold. Molecules into cells: specifying spatial architecture. *Microbiology and molecular biology reviews : MMBR*, 69(4):544–564, 2005.

[50] L. Merlini. Mate and fuse: how yeast cells do it. *Open Biology*, 3(3):130008–130008, 2013.

[51] E. Bi and H.O. Park. Cell Polarization and Cytokinesis in Budding Yeast. *Genetics*, 191(2):347–387, 2012.

[52] D. Pruyne and A. Bretscher. Polarization of cell growth in yeast: I. establishment and maintenance of polarity states. *J. Cell Sci.*, 113:365–375, 2000.

[53] M. Evangelista, K. Blundell, M.S. Longtine, C.J. Chow, N. Adames, J.R. Pringle, M. Peter, and C. Boone. Bni1p, a yeast formin linking Cdc42p and the actin cytoskeleton during polarized morphogenesis. *Science*, 276(5309):118–122, 1997.

[54] M. Snyder. The Spa2 Protein of Yeast Localizes to Sites of Cell-Growth. *The Journal of Cell Biology*, 108(4):1419–1429, 1989.

[55] S. Bidlingmaier and M. Snyder. Regulation of polarized growth initiation and termination cycles by the polarisome and Cdc42 regulators. *The Journal of Cell Biology*, 164(2):207–218, 2004.

[56] D.R. TerBush, T. Maurice, D. Roth, and P. Novick. The Exocyst is A Multiprotein Complex Required For Exocytosis In *Saccharomyces Cerevisiae* . *Embo Journal*, 15(23):64883–66494, 1996.

[57] D.E. Levin. Cell wall integrity signaling in Saccharomyces cerevisiae. *Microbiology and Molecular Biology Reviews*, 69(2):262–291, 2005.

[58] R. Rodicio and J.J. Heinisch. Together we are strong—cell wall integrity sensors in yeasts. *Yeast*, 27(8):531–540, 2010.

[59] D.E. Levin. Regulation of Cell Wall Biogenesis in Saccharomyces cerevisiae: The Cell Wall Integrity Signaling Pathway. *Genetics*, 189(4):1145–1175, 2011.

[60] C. Kock, Y.F. Dufrêne, and J.J. Heinisch. Up against the Wall: Is Yeast Cell Wall Integrity Ensured by Mechanosensing in Plasma Membrane Microdomains? *Appl. Environ. Microbiol.*, 81(3):806–811, 2015.

[61] J. Verna, A. Lodder, K. Lee, A. Vagts, and R. Ballester. A family of genes required for maintenance of cell wall integrity and for the stress response in Saccharomyces cerevisiae. *Proceedings of the National Academy of Sciences*, 94(25):13804–13809, 1997.

[62] B.D. Manning, R. Padmanabha, and M. Snyder. The Rho-GEF Rom2p Localizes to Sites of Polarized Cell Growth and Participates in Cytoskeletal Functions in Saccharomyces cerevisiae. *Molecular Biology of the Cell*, 8(10):1829–1844, 1997.

[63] B. Philip and D.E. Levin. Wsc1 and Mid2 Are Cell Surface Sensors for Cell Wall Integrity Signaling That Act through Rom2, a Guanine Nucleotide Exchange Factor for Rho1. *Mol. Cell. Biol.*, 21(1):271–280, 2001.

[64] P. Perez and S.A. Rincón. Rho GTPases: regulation of cell polarity and growth in yeasts. *Biochem. J.*, 426(3):243–253, 2010.

[65] V. Dupres, D. Alsteens, S. Wilk, B. Hansen, J.J. Heinisch, and Y.F. Dufrêne. The yeast Wsc1 cell surface sensor behaves like a nanospring in vivo. *Nat Chem Biol*, 5(11):857–862, 2009.

[66] A. Straede and J. Heinisch. Functional analyses of the extra- and intracellular domains of the yeast cell wall integrity sensors Mid2 and Wsc1. *FEBS Letters*, 581(23):4495–4500, 2007.

[67] F. Hutzler, R. Gerstl, M. Lommel, and S. Strahl. Protein N-glycosylation determines functionality of the Saccharomyces cerevisiaecell wall integrity sensor Mid2p. *Mol Microbiol*, 68(6):1438–1449, 2008.

[68] T. Ono, T. Suzuki, Y. Anraku, and H. Iida. The *MID2* gene encodes a putative integral membrane protein with a Ca2 +-binding domain and shows mating pheromone-stimulated expression in *Saccharomyces cerivisiae*. *Gene*, 151:203–208, 1994.

[69] T. Ketela, R. Green, and H. Bussey. *Saccharomyces cerevisiae* Mid2p Is a Potential Cell Wall Stress Sensor and Upstream Activator of the *PKC1-MPK1* Cell Integrity Pathway . *Journal of Bacteriology*, 181(11):3330–3340, 1999.

[70] M. Rajavel, B. Philip, B.M. Buehrer, B. Errede, and D.E. Levin. Mid2 Is a Putative Sensor for Cell Integrity Signaling in Saccharomyces cerevisiae. *Mol. Cell. Biol.*, 19(6):3969–3976, 1999.

[71] B. Chapa-y Lazo, E.G. Allwood, I.I. Smaczynska-de Rooij, M.L. Snape, and K.R. Ayscough. Yeast Endocytic Adaptor AP-2 Binds the Stress Sensor Mid2 and Functions in Polarized Cell Responses. *Traffic*, 15(5):546–557, 2014.

[72] F.M. Klis, C.G. de Koster, and S. Brul. Cell Wall-Related Bionumbers and Bioestimates of Saccharomyces cerevisiae and Candida albicans. *Eukaryotic Cell*, 13(1):2–9, 2014.

[73] C. Chou, T.I. Moore, S.D. Chang, Q. Nie, and T.M. Yi. Signaling regulated endocytosis and exocytosis lead to mating pheromone concentration dependent morphologies in yeast. *FEBS Letters*, 586(23):4208–4214, 2012.

[74] B.W. Van De Fliert, P.D. Howell, and J.R. Ockenden. Pressure-driven flow of a thin viscous sheet. *J. Fluid Mech.*, 292(-1):359–376, 1995.

[75] M. Bosch and P.K. Hepler. Pectin methylesterases and pectin dynamics in pollen tubes. *The Plant cell*, 17(12):3219–3226, 2005.

[76] P. Fayant, O. Girlanda, Y. Chebli, C.E. Aubin, I. Villemure, and A. Geitmann. Finite Element Model of Polar Growth in Pollen Tubes. *Plant Cell*, 22(8):2579–2593, 2010.

[77] D.J. Adams. Fungal cell wall chitinases and glucanases. *Microbiology*, 150(7):2029–2035, 2004.

[78] C.M. Douglas, F. Foor, J.A. Marrinan, N. Morin, J.B. Nielsen, A.M. Dahl, P. Mazur, W. Baginsky, W.L. Li, M. Elsherbeini, J.A. Clemas, S.M. Mandala, B.R. Frommer, and M.B. Kurtz. The Saccharomyces-Cerevisiae Fks1 (Etg1) Gene Encodes an Integral Membrane-Protein Which Is a Subunit of 1,3-Beta-D-Glucan Synthase. *Proceedings of the National Academy of Sciences*, 91(26):12907–12911, 1994.

[79] T. Utsugi, M. Minemura, A. Hirata, M. Abe, D. Watanabe, and Y. Ohya. Movement of yeast 1,3-beta-glucan synthase is essential for uniform cell wall synthesis. *Genes to Cells*, 7(1):1–9, 2002.

[80] P. Delley and M.N. Hall. Cell Wall Stress Depolarizes Cell Growth Via Hyperactivation of RHO1. *The Journal of Cell Biology*, 147(1):163–174, 1999.

[81] M. Abe, H. Qadota, A. Hirata, and Y. Ohya. Lack of GTP-bound Rho1p in secretory vesicles of Saccharomyces cerevisiae. *The Journal of Cell Biology*, 162(1):85–97, 2003.

[82] M. Jose, S. Tollis, D. Nair, J. Sibarita, and D. McCusker. Robust polarity establishment occurs via an endocytosis-based cortical corralling mechanism. *The Journal of Cell Biology*, 200(4):407–418, 2013.

[83] J. Valdez-Taubas and H.R.B. Pelham. Slow Diffusion of Proteins in the Yeast Plasma Membrane Allows Polarity to Be Maintained by Endocytic Cycling. *Current Biology*, 13(18):1636–1640, 2003.

[84] L.B. Huberman and A.W. Murray. A Model for Cell Wall Dissolution in Mating Yeast Cells: Polarized Secretion and Restricted Diffusion of Cell Wall Remodeling Enzymes Induces Local Dissolution. *PLoS ONE*, 9(10), 2014.

[85] L. Carrillo, B. Cucu, V. Bandmann, U. Homann, B. Hertel, S. Hillmer, G. Thiel, and A. Bertl. High-Resolution Membrane Capacitance Measurements for Studying Endocytosis and Exocytosis in Yeast. *Traffic*, 16(7):760–772, 2015.

[86] F.P. Finger and P. Hughes, T.E.and Novick. Sec3p Is a Spatial Landmark for Polarized Secretion in Budding Yeast. *Cell*, 92(4):559–571, 1998.

[87] R. Teparić and V. Mrša. Proteins involved in building, maintaining and remodeling of yeast cell walls. *Current Genetics*, 59(4):171–185, 2013.

[88] N. Röckel, S. Wolf, B. Kost, T. Rausch, and S. Greiner. Elaborate spatial patterning of cell-wall PME and PMEI at the pollen tube tip involves PMEI endocytosis, and reflects the distribution of esterified and de-esterified pectins. *The Plant journal : for cell and molecular biology*, 53(1):133–143, 2008.

[89] K.C. Huang, R. Mukhopadhyay, B. Wen, Z. Gitai, and N.S. Wingreen. Cell shape and cell-wall organization in Gram-negative bacteria. *Proceedings of the National Academy of Sciences of the United States of America*, 105(49):19282–19287, 2008.

[90] M.T. Cabeen and C. Jacobs-Wagner. Bacterial cell shape. *Nature reviews Microbiology*, 3(8):601–610, 2005.

[91] D. Bonazzi, J.D. Julien, M. Romao, R. Seddiki, M. Piel, A. Boudaoud, and N. Minc. Symmetry Breaking in Spore GerminationRelies on an Interplay between Polar Cap Stability and Spore Wall Mechanics. *Developmental cell*, 28(5):534–546, 2014.

[92] V. Davì and N. Minc. Mechanics and morphogenesis of fission yeast cells. *Current opinion in microbiology*, 28(C):36–45, 2015.

[93] N.W. Goehring and S.W. Grill. Cell polarity: mechanochemical patterning. *Trends in Cell Biology*, 23(2):72–80, 2013.

[94] A. Diz-Muñoz, D.A. Fletcher, and O.D. Weiner. Use the force: membrane tension as an organizer of cell shape and motility. *Trends in Cell Biology*, 23(2):47–53, 2013.

[95] C. Guthrie and G. Fink. Guide to yeast genetics and molecular biology. *Methods in Enzymology*, 194:1–863, 1991.

[96] U. Gueldener, J. Heinisch, G.J. Koehler, D. Voss, and J.H. Hegemann. A second set of loxp marker cassettes for cre-mediated multiple gene knockouts in budding yeast. *Nucleic Acids Res.*, 30:e23, 2002.

[97] A. Diz-Muñoz, O.D. Weiner, and D.A. Fletcher. In pursuit of the mechanics that shape cell surfaces. *Nature Physics*, 14(7):1–5, 2018.

[98] A. Diz-Muñoz, D.A. Fletcher, and O.D. Weiner. Use the force: membrane tension as an organizer of cell shape and motility. *Trends in Cell Biology*, 23(2):47–53, 2013.

[99] M. Trogdon. *Combining Biochemical Signaling and Mechanics to Understand Yeast Mating Morphogenesis*. PhD thesis, University of California, Santa Barbara, 2018.

[100] M. Ziman, D. Preuss, J. Mulholland, OBrien J.M., B. David, and D.I. Johnson. Subcellular localization of cdc42p, a Saccharomyces cerevisiae GTP-binding protein involved in the control of cell polarity. *Molecular Biology of the Cell*, 4:1307–1316, 1993.

[101] R. Wedlich-Soldner. Robust cell polarity is a dynamic state established by coupling transport and GTPase signaling. *Journal of Cell Biology*, 166(6):889–900, 2004.

[102] M. Evangelista, K. Blundell, M.S. Longtine, C.J. Chow, N. Adames, J.R. Pringle, M. Peter, and C. Boone. Bni1p, a Yeast Formin Linking Cdc42p and the Actin Cytoskeleton During Polarized Morphogenesis. *Science*, 276(5309):118–122, 1997.

[103] Y. Dong, D. Pruyne, and A. Bretscher. Formin-dependent actin assembly is regulated by distinct modes of Rho signaling in yeast. *Journal of Cell Biology*, 161(6):1081–1092, 2003.

[104] B. Drawert, M. Trogdon, S. Toor, L.R. Petzold, and A. Hellander. MOLNs: A Cloud Platform for Interactive, Reproducible, and Scalable Spatial Stochastic Computational Experiments in Systems Biology Using PyURDME. *SIAM Journal on Scientific Computing*, 38(3):C179–C202, 2016.

[105] B. Klünder, T. Freisinger, Roland Wedlich-Söldner, and E. Frey. GDI-Mediated Cell Polarization in Yeast Provides Precise Spatial and Temporal Control of Cdc42 Signaling. *PLoS Computational Biology*, 9(12):e1003396–12, 2013.

[106] M.J. Lawson, B. Drawert, M. Khammash, L.R. Petzold, and T.M. Yi. Spatial Stochastic Dynamics Enable Robust Cell Polarization. *PLoS Computational Biology*, 9(7), 2013.

[107] B. Drawert, S. Hellander, M. Trogdon, T.M. Yi, and L. Petzold. A framework for discrete stochastic simulation on 3D moving boundary domains. *The Journal of Chemical Physics*, 145(18):184113–12, 2016.

[108] R. Wedlich-Soldner. Spontaneous Cell Polarization Through Actomyosin-Based Delivery of the Cdc42 GTPase. *Science*, 299(5610):1231–1235, 2003.

[109] E.M. Ozbudak, A. Becskei, and A. van Oudenaarden. A System of Counteracting Feedback Loops Regulates Cdc42p Activity during Spontaneous Cell Polarization. *Developmental Cell*, 9(4):565–571, 2005.

[110] E. Marco, R. Wedlich-Söldner, R. Li, S.J. Altschuler, and L.F. Wu. Endocytosis Optimizes the Dynamic Localization of Membrane Proteins that Regulate Cortical Polarity. *Cell*, 129(2):411–422, 2007.

[111] B.D Slaughter, A. Das, J.W. Schwartz, B. Rubinstein, and R. Li. Dual Modes of Cdc42 Recycling Fine-Tune Polarized Morphogenesis. *Developmental Cell*, 17(6):823–835, 2009.

[112] K.C. Huang, R. Mukhopadhay, B. Wen, Z. Gitai, and N.S. Wingreen. Cell shape and cell-wall organization in Gram-negative bacteria. *PNAS*, 105:19282–19287, 2008.

[113] A. Geitmann and Joseph K.E. Ortega. Mechanics and modeling of plant cell growth. *Trends in Plant Science*, 14(9):467–478, 2009.

[114] Ma.T. Cabeen and C. Jacobs-Wagner. Bacterial cell shape. *Nature Reviews Microbiology*, 3(8):601–610, 2005.

[115] A. Haupt, D. Ershov, and N. Minc. A Positive Feedback between Growth and Polarity Provides Directional Persistency and Flexibility to the Process of Tip Growth. *Current Biology*, 28(20):1–14, 2018.

[116] V. Davì, H. Tanimoto, D Ershov, A. Haupt, H. De Belly, R. Le Borgne, E. Couturier, A. Boudaoud, and N. Minc. Mechanosensation Dynamically Coordinates Polar Growth and Cell Wall Assembly to Promote Cell Survival. *Developmental Cell*, 45(2):170–182.e7, 2018.

[117] V. Davì and N. Minc. ScienceDirect Mechanics and morphogenesis of fission yeast cells. *Current Opinion in Microbiology*, 28(C):36–45, 2015.

[118] D. Bonazzi, J. Julien, M. Romao, R. Seddiki, M. Piel, A. Boudaoud, and N. Minc. Symmetry Breaking in Spore Germination Relies on an Interplay between Polar Cap Stability and Spore Wall Mechanics. *Developmental Cell*, 28(5):534–546, 2014.

[119] N.W. Goehring and S.W. Grill. Cell polarity: mechanochemical patterning. *Trends in Cell Biology*, 23(2):72–80, 2013.

[120] A.C. Hindmarsh, P.N. Brown, K.E. Grant, S.L. Lee, R. Serban, D.E. Shumaker, and C.S. Woodward. SUNDIALS: Suite of Nonlinear and Differential/Algebraic Equation Solvers. *ACM Transactions on Mathematical Software*, 31:363–396, 2005.

[121] B. Steventon, F. Duarte, R. Lagadec, S. Mazan, J. Nicolas, and E. Hirsinger. Species-specific contribution of volumetric growth and tissue convergence to posterior body elongation in vertebrates. *Development*, 143(10):1732–1741, 2016.

[122] L. Zhang, C. Kendrick, D. Julich, and S.A. Holley. Cell cycle progression is required for zebrafish somite morphogenesis but not segmentation clock function. *Development*, 135(12):2065–2070, 2008.

[123] D. Kimelman. *Tales of Tails (and Trunks): Forming the Posterior Body in Vertebrate Embryos*, volume 116 of *Current Topics in Developmental Biology*. Elsevier Inc., 1 edition, 2016.

[124] P. McMillen and S.A. Holley. The tissue mechanics of vertebrate body elongation and segmentation. *Current Opinion in Genetics & Development*, 32:106–111, 2015.

[125] S.J. Streichan, C.R. Hoerner, T. Schneidt, D. Holzer, and L. Hufnagel. Spatial constraints control cell proliferation in tissues. *Proceedings of the National Academy of Sciences*, 111(15):5586–5591, 2014.

[126] T. Mochizuki, S. Suzuki, and I. Masai. Spatial pattern of cell geometry and cell-division orientation in zebrafish lens epithelium. *Biology Open*, 3(10):982–994, 2014.

[127] C.P. Heisenberg and Y. Bellaïche. Forces in Tissue Morphogenesis and Patterning. *Cell*, 153(5):948–962, 2013.

[128] B. Boehm, H. Westerberg, G. Lesnicar-Pucko, S. Raja, M. Rautschka, J. Cotterell, J. Swoger, and J. Sharpe. The Role of Spatially Controlled Cell Proliferation in Limb Bud Morphogenesis. *PLoS Biology*, 8(7):e1000420–21, 2010.

[129] O. Campàs. A toolbox to explore the mechanics of living embryonic tissues. *Seminars in Cell and Developmental Biology*, 55:119–130, 2016.

[130] W.S. Talbot, B. Trevarrow, M.E. Halpern, A.E. Melby, G. Farr, J.H. Postlethwait, T. Jowett, C.B. Kimmel, and D. Kimelman. A homeobox gene essential for zebrafish notochord development. *Nature*, 378(6553):150–157, 1995.

[131] J.P. Kanki and R.K. Ho. The development of the posterior body in zebrafish. *Development*, pages 881–893, 1997.

[132] A.J. Liu and S.R. Nagel. Jamming is not just cool any more. *Nature*, 396:1–2, 1998.

[133] F. Serwane, A. Mongera, P. Rowghanian, D.A. Kealhofer, A.A. Lucio, Z.M. Hockenbery, and O. Campàs. In vivo quantification of spatially varying mechanical properties in developing tissues. *Nature Methods*, 14(2):181–186, 2016.

[134] S. Cohen-Addad, R. Hhler, and O. Pitois. Flow in foams and flowing foams. *Annual Review of Fluid Mechanics*, 45(1):241–267, 2013.

[135] J.H. Ferziger and M. Peric. *Computational Methods for Fluid Dynamics*. Springer-Verlag Berlin Heidelberg, 2002.

[136] M.L Manning, R.A. Foty, M.S. Steinberg, and E. Schoetz. Coaction of intercellular adhesion and cortical tension specifies tissue surface tension. *PNAS*, 107:1–6, 2010.

[137] P. Marmottant, A. Mgharbel, J. Kafer, B. Audren, J.P. Rieu, J.C. Vial, B. van der Sanden, A.F.M. Maree, F. Graner, and H. Delanoe-Ayari. The role of fluctuations and stress on the effective viscosity of cell aggregates. *Proceedings of the National Academy of Sciences*, 106(41):17271–17275, 2009.

[138] C. Nusslein-Volhard and R. Dahm. *Zebrafish: a practical approach*. Oxford Univ. Press, 2002.

[139] S. Pauls, B. Geldmacher-Voss, and J.A. Campos-Ortega. A zebrafish histone variant H2A.F/Z and a transgenic H2A.F/Z:GFP fusion protein for in vivo studies of embryonic development. *Development Genes and Evolution*, 211(12):603–610, 2001.

[140] Y. Artemenko, T.J. Lampert, and P.N. Devreotes. Moving towards a paradigm: common mechanisms of chemotactic signaling in Dictyostelium and mammalian leukocytes. *Cellular and Molecular Life Sciences*, 71(19):3711–3747, 2014.

[141] A. Shindo. Models of convergent extension during morphogenesis. *Wiley Interdisciplinary Reviews: Developmental Biology*, 7(1):e293–17, 2017.

[142] R.E. Keller, M. Danilchik, R. Gimlich, and J. Shih. The function and mechanism of convergent extension during gastrulation of *Xenopus laevis*. *Development*, 89:1–26, 1985.

[143] P. Ybot-Gonzalez, D. Savery, D. Gerrelli, M. Signore, C.E. Mitchell, C.H. Faux, N.D.E. Greene, and A.J. Copp. Convergent extension, planar-cell-polarity signalling and initiation of mouse neural tube closure. *Development*, 134(4):789–799, 2007.

[144] M. Tada and C.P. Heisenberg. Convergent extension: using collective cell migration and cell intercalation to shape embryos. *Development*, 139(21):3897–3904, 2012.

[145] P.W. Anderson. More is Different Science. *Science*, 177(4047):393–396, 1972.

[146] J. Schaber, M. Angel Adrover, E. Eriksson, S. Pelet, E. Petelenz-Kurdziel, D. Klein, F. Posas, M. Goksor, M. Peter, S. Hohmann, and E. Klipp. Biophysical properties of Saccharomyces cerevisiae and their relationship with HOG pathway activation. *European Biophysics Journal with Biophysics Letters*, 39(11):1547–1556, 2010.